2015

Development and Optimization of Non-Hydrostatic Models for Water Waves and Fluid-Vegetation Interaction

Ling Zhu
Louisiana State University and Agricultural and Mechanical College, lzhu5@lsu.edu

DEVELOPMENT AND OPTIMIZATION OF NON-HYDROSTATIC MODELS FOR WATER WAVES AND FLUID-VEGETATION INTERACTION

A Dissertation

Submitted to the Graduate Faculty of the
Louisiana State University and
Agricultural and Mechanical College
in partial fulfillment of the
requirements for the degree of
Doctor of Philosophy
in

The Department of Civil and Environmental Engineering

by
Ling Zhu
B.S., East China Normal University, 2006
M.S., East China Normal University, 2009
August 2015

ACKNOWLEDGMENTS

I would like to express the deepest appreciation to my major professor, Dr. Qin J. Chen for his aspiring guidance, encouragement and support throughout my Ph.D. study. I thank Dr. Xiaoliang Wan, Dr. Haosheng Huang, and Dr. Frank Tsai for serving on my dissertation committee and providing valuable advice. I thank Dr. Krishnaswamy Nandakumar for serving as Dean's representative for my general and final exams. My dissertation research benefits greatly from discussions with Dr. Xiaoliang Wan on numerical methods.

I am grateful to my friends and colleagues Dr. Kelin Hu, Agnimitro Chakrabarti, Getnet Agegnehu and Ke Liu, who have shared with me their knowledge and experience in numerical modeling and been very supportive. I thank Dr. Jian Tao, Dr. Peter Diener, and Dr. Steve Brandt from the Center for Computation and Technology, LSU, who also provided valuable suggestions in numerical modeling that benefit my dissertation research. I also thank my friends and colleagues Dr. Arash Karimpour, Dr. Ranjit Jadhav, Cody Johnson and Kyle Parker for sharing with me their field experience. Special thanks are dedicated to Dr. Haihong Zhao, who shared with me not only her knowledge in coastal engineering that benefits my dissertation research but also her life experiences that carry me through tough moments.

I would like to acknowledge Dr. Don Liu from Louisiana Tech University, Dr. Gangfeng Ma from Old Dominion University, and Dr. Xing Yulong from University of Tennessee. They shared with me their experience and knowledge in numerical modeling that benefit my dissertation research. Also I would like to express my gratitude to Dr. Yavuz Ozeren who provided us with his laboratory data for model verification. The studies were supported by the US National Science Foundation (NSF) (CBET-0652859 and DMS-1115527).

Last but not least, I would like to express many thanks to my great parents for their unconditional and continual support throughout my graduate study.

TABLE OF CONTENTS

ABSTRACT

The primary objective of this study is twofold: 1) to develop an efficient and accurate non-hydrostatic wave model for fully dispersive highly nonlinear waves, and 2) to investigate the interaction between waves and submerged flexible vegetation using a fully coupled wave-vegetation model. This research consists of three parts. Firstly, an analytical dispersion relationship is derived for waves simulated by utilizing the Keller-box scheme and central differencing for vertical discretization. The phase speed can be expressed as a rational polynomial function of the dimensionless water depth, kh, and the layer distribution in the water column becomes an optimizable parameter in this function. For a given tolerance dispersion error, the range of kh is extended and the layer thicknesses are optimally selected. The derived theoretical dispersion relationship is tested with linear and nonlinear standing waves generated by an Euler model. The optimization method is applicable to other non-hydrostatic models for water waves.

Secondly, an efficient and accurate approach is developed to solve Euler equations for fully dispersive and highly nonlinear water waves. Discontinuous Galerkin, finite difference, and spectral element formulations are used for horizontal discretization, vertical discretization, and the Poisson equation, respectively. The Keller-box scheme is adopted for its capability of resolving frequency dispersion accurately with low vertical resolution (two or three layers). A three-stage optimal Strong Stability-Preserving Runge-Kutta (SSP-RK) scheme is employed for time integration. Thirdly, a fully coupled wave-vegetation model for simulating the interaction between water waves and submerged flexible plants is presented. The complete governing equation for vegetation motion is solved with a high-order finite element method and an implicit time differencing scheme. The vegetation model is fully coupled with a wave model to explore the relationship between displacement of water particle and plant stem, as well as the effect of vegetation flexibility on wave attenuation. This vegetation deformation model can be coupled with other wave models to simulate wave-vegetation interactions.

CHAPTER 1 INTRODUCTION

Waves, the most familiar features existing from ocean to rivers, exhibit the power of nature and influence the life of all residence in this planet. Water wave motions include wind-generated surface waves, tidal waves and long-period oscillations in estuaries, tsunami waves generated by earthquakes, waves generated by a moving ship, landslides, or explosions near or under the water, etc.. In physical oceanography, and coastal and ocean engineering, an accurate and efficient prediction of surface waves is of paramount importance. With the rapid development in computational technology, substantial efforts have been devoted to developing numerical models for simulating the propagation and evolution of water waves from deep water to the shoreline, as well as wave-structure interactions in the coastal area.

1.1 Numerical Modeling of Water Waves

Existing numerical wave models can be categorized as (i) phase-averaged models and (ii) phase-resolving models. The former type of model, based on the wave energy balance principle, simulates the spectral evolution of dispersive waves. Over the last three decades, various phase-averaged models have been developed. For instance, Simulating Waves Nearshore (SWAN) model (Booij et al. 1999; Ris et al. 1999) has been widely used in the coastal engineering and science community to predict or simulate wind-generated waves in oceans, coastal regions and inland waters.

Phase-resolving wave models are based on the conservation laws of mass and momentum for fluid motions. Examples of this type of models include mild-slope equations (e.g. Refraction-Diffraction Wave (REFDIF1) model (Kirby and Dalrymple 1994)), Boussinesq-type equations (e.g. Fully Nonlinear Boussinesq Wave (FUNWAVE) model (Kirby et al. 1998)), and incompressible Navier-Stokes (N-S) equations or Euler equations for fluid motions (e.g. Simulating WAves till SHore (SWASH) model (Zijlema and Stelling 2005; Zijlema et al. 2011), Non-Hydrostatic Wave (NHWAVES) model (Ma et al. 2012)).

To model nearshore waves with strong nonlinearity, Boussinesq or N-S/Euler models are more desirable. The classic Boussinesq models (e.g. Peregrine 1967) have the drawback of weak dispersion and weak nonlinearity, or a limited range of applicability. By introducing a reference velocity at an arbitrary vertical location as the velocity variable and choosing the location to match the Padé [2, 2] expansion of the exact linear dispersion relationship, Nwogu (1993) extended the applicability of the model to $kh \approx 3$, here k is the wave number, and h is the water depth. The dimensionless wave number kh serve as a measure of dispersion.

Many efforts have been devoted to enhancing the deep-water accuracy of the depth-integrated approach by developing high-order Boussinesq-type models. By utilizing a quartic polynomial approximation for the vertical profile of velocity field, Gobbi and Kirby (1999) developed a model with excellent linear dispersion properties up to $kh \approx 6$. The models of Madsen and Schäffer (1998), and Chen et al. (1998) also showed good linear dispersive wave properties up to $kh \approx 6$. Madsen et al. (2002) further improved the Boussinesq-type model and made it applicable to extremely deep-water waves with $kh \approx 40$. Agnon et al. (1999) presented a new procedure to achieve good nonlinear dispersion properties up to $kh \approx 6$.

Lynett and Liu (2004a and 2004b) introduced another approach to improve the dispersion accuracy of Boussinesq-type models. Instead of using a high-order approximation for the vertical profile of the flow field, they used N independent quadratic polynomial approximations for the velocity profiles. These polynomial approximations match at the interfaces that divide the water column into N layers. Good dispersion accuracy up to $kh \approx 8$ was achieved with an optimized two-layer model. Chazel et al. (2009) combined the approach in Madsen et al. (2002) and the approach in Lynett and Liu (2004a), and developed an efficient model with less complexity. This model exhibits good linear and nonlinear dispersion properties up to $kh \approx 10$.

Navier-Stokes or Euler models are derived from the mass and momentum conservation laws without assuming a vertical distribution of the velocity field, which describe the general

fluid flow including water waves. Navier-Stokes or Euler models are capable of simulating complex problems, such as wave breaking, wave-current interaction, wave-structure interaction, etc. The momentum equations are solved at every layer for this type of models, thus the computational cost is higher compared with Boussinesq-type models. Therefore, the practical applications of such models are restricted to small-scale problems.

The challenges in developing a N-S/Euler model lie in (i) solving a Poisson equation for non-hydrostatic pressure; (ii) tracking the free-surface; (iii) devising a stable and efficient scheme; (iv) handling nonlinearity and capturing shocks for applications related to wave breaking; and (v) achieving high accuracy without sacrificing efficiency.

Navier-Stokes or Euler models do not assume that the pressure in a flow is hydrostatic; therefore, are able to accurately simulate short wave propagation. The non-hydrostatic pressure is a passive variable that depends on the velocity field. The non-hydrostatic pressure can be determined by solving a Poisson equation, obtained by taking the divergence of the momentum equations and employing the continuity equation.

One of the techniques to couple velocity field and pressure is the projection method proposed by Chorin (1968, 1969). This method fully splits the advection and pressure gradient terms into two steps. An intermediate velocity field is calculated with the absence of pressure at first, and then the non-hydrostatic pressure is solved from a Poisson equation. The velocity filed is updated with the resulting pressure. This method is easy to implement but introduces splitting error because of the lack of information passing between the advection and pressure terms.

Casulli and Zanolli (2002) proposed to add a correction for the water level in the second step. Zijlema and Stelling (2005) introduced a prediction-correction procedure with the use of semi-implicit time stepping. This algorithm is divided into hydrostatic and non-hydrostatic parts. In the hydrostatic part, the free surface is computed, whereas in the non-hydrostatic part,

the non-hydrostatic pressure is computed. Firstly, in the hydrostatic part, an estimate of the velocity field is achieved by solving the momentum equations including the non-hydrostatic pressure at the current time level. Secondly, in the non-hydrostatic part, the pressure correction, i.e. the difference of non-hydrostatic pressure between the current and next time levels, is computed by solving a Poisson equation. Lastly, through the pressure correction, the intermediate velocity field is corrected, resulting in a divergence-free velocity field.

The non-hydrostatic pressure on the top layer can be enforced by means of: (1) employing edge-based grid systems (e.g. Lin and Li 2002; Zijlema and Stelling 2005, 2008; Zijlema et al. 2011; Chen et al. 2011; Ma et al. 2012), (2) using the integration method (e.g. Yuan and Wu 2004), (3) implementing interpolation approaches (e.g. Walters 2005; Choi and Wu 2006; Young et al. 2007; Badiei et al. 2008), and (4) embedding Boussinesq-type equations into the Navier-Stokes models (e.g. Wu et al. 2010). Among these approaches, the edge-based grid systems allow precise assignment of pressure on the top layer, thereby more favored.

Numerical techniques to resolve a free surface in the flow simulation include marker and cell (MAC) (e.g. Harlow and Welch 1965), arbitrary Lagrangian-Eulerian (ALE) (e.g. Donea et al. 1982) volume of fluid (VOF) (e.g. Hirt and Nichols 1981), and level set methods (e.g. Osher and Sethian 1988). Curvilinear boundary-fitted coordinates are often used in wave models for mapping the irregular physical domain vertically with wavy surface and uneven bottom (e.g. σ-coordinate), and horizontally (e.g. Shi et al. 2001) into a regular domain. The surface elevation can be computed by solving the kinematic free surface boundary conditions or integrated mass equation (e.g. Zhu et al. 2014).

1.2 Wave-Vegetation Interaction

Coastal wetlands have been recognized as a buffer zone protecting the inner land and a natural erosion barrier stabilizing the shoreline. By attenuating incoming waves and trapping sediment in vegetated areas, the coastal vegetation can provide substantial protection from erosion.

Considerable efforts have been devoted to field studies (e.g. Bradley and Houser 2009; Jadhav et al. 2013; Jadhav and Chen 2013), laboratory experiments (e.g. Stratigaki et al. 2011; Koftis et al. 2013; Ozeren et al. 2013; Anderson and Smith 2014) and numerical simulations (e.g. Li and Yan 2007; Dijkstra and Uittenbogaard 2010; Suzuki et al. 2011; Wu et al. 2012; Tang et al. 2013; Blackmar et al. 2014; Zhan et al. 2014) aimed at quantifying vegetation-induced wave attenuation, and understanding wave-vegetation interactions.

With regard to field studies, a recent work by Jadhav et al. (2013) analyzed spectral energy dissipation of random waves due to salt marsh vegetation using data collected during a tropical storm. A frequency-dependent velocity attenuation parameter inside the canopy was utilized to parameterize the spectral variation and predict energy dissipation.

With regard to laboratory experiments, a recent study by Anderson and Smith (2014) investigated the relationship between wave attenuation and stem density, submergence, incident wave height, and peak period based on laboratory data. The transformation of wave energy spectra was analyzed and estimation for a bulk drag coefficient C_D was proposed. A summary of field and laboratory studies can be found in Anderson et al. (2011). Most of the studies, however, assumed vegetation is rigid and neglected the plant motion.

Field works and laboratory experiments can provide valuable data, but they are either difficult to control, impossible to replicate, or expensive to conduct. Numerical simulations, on the other hand, can provide useful results in an inexpensive manner. In the past several decades, various numerical models have been developed to study wave attenuation caused by vegetation. These models are either phase-resolving models based on Navier-Stokes equations (e.g. Li and Yan 2007; Wu et al. 2012; Ma et al. 2013; Zhan et al. 2014), Boussinesq equations (e.g. Augustin et al. 2009; Iimura and Tanaka 2012; Blackmar et al. 2014), and shallow water equations (e.g. Tang et al. 2013), or phase-averaged models based on the wave-action or wave energy balance equations (e.g. Suzuki et al. 2011; Chen and Zhao 2012). To consider the vegetation

effect, these models either treat the vegetation as a rough bottom with high friction (e.g. Möller et al. 1999; Fathi-Moghadam et al. 2011), or add the drag (and inertial) force to the momentum equations (e.g. Dalrymple et al. 1984; Ikeda et al. 2001; Maza et al. 2013).

Most natural vegetation is deformable, which reduces the flow resistance. In contrast to the large number of models neglecting vegetation motions, only a small number of models consider the vegetation swaying effect. A simple but less robust way is to reduce the drag coefficient to achieve the equivalent wave attenuation (Kobayashi et al. 1993). The drag coefficient due to swaying is not only a function of the plant rigidity but also influenced by the degree of submergence and hydrodynamic conditions. The calibrated drag coefficients are on the order of 0.1 in Kobayashi et al. (1993). However, application of this method is limited because of the uncertainty of the drag coefficient.

Zhao and Chen (2013) extended and unified resistance formulations for rigid and deformable plants under both emergent and submergent conditions. A resistance formulation and an empirical relationship between the deflected vegetation height and the flow drag exerted on vegetation elements were utilized to iteratively determine the changing drag force and vegetation deformation. Li and Xie (2011) investigated the hydrodynamics of submerged flexible vegetation with and without foliage using a 3D non-hydrostatic model with the σ-coordinate for the treatment of the free surface. The effective stem height was determined by an empirical formulation obtained by solving a bending equation in a sufficient large number of cases with different conditions. Only the effective height of the deformed vegetation was included to account for the reduction of drag due to plant deformation under combined wave and current conditions.

A different methodology is to solve the vegetation motion from a force balance equation and incorporate relative velocities into the vegetation-induced resistance (Asano et al. 1992; Dubi and Torum 1996; Mendez et al. 1999; Ikeda et al. 2001; Maza et al. 2013). The balance

of forces for the vegetation motion includes buoyancy, damping, stiffness of the vegetation, and gravity as restoring forces, and drag and inertia as driving forces (Asano et al. 1992; Ikeda et al. 2001). Mullarney et al. (2010) presented a theoretical relationship between the movements of single-stem vegetation and water particle based on the cantilever beam theory, balancing stiffness with drag on stem elements. The model assumed negligible inertia and buoyancy, small deformations, and thin near-vertical stems. A dimensionless parameter S was proposed to measure vegetation stiffness. This parameter incorporates material and geometric properties of the vegetation, as well as wave period and velocity. When S approaches 0, stems move with the surrounding fluid particles except in a thin near-bed elastic boundary layer, whereas when S approaches infinity, stem deflections approach zero but lead the displacements of surrounding fluid particles by 90°. Mullarney et al. (2010) also concluded that the simulated dissipation by the flexible stems was about 30% of the dissipation caused by equivalent rigid stems.

1.3 Numerical methods

The traditional mesh-based numerical methods include finite difference (FD), finite volume (FV) and finite element (FE) methods. When deciding which numerical method to use, we need to take into account the following factors: (1) simplicity to implement, (2) flexibility to accommodate complex geometries, (3) efficiency, and (4) accuracy.

Finite difference methods are the easiest to implement and the discretization is intuitive. Extensive theories have been developed for FD methods (e.g. Gustafsson et al. 2001). However, they have difficulties in resolving geometries with complex boundaries. Finite volume methods, enabling element-based discretization, are close to FD methods but with better geometric flexibility. For a complex domain, FV methods allow unstructured meshes (e.g. triangle meshes) that can be conformal to irregular domain boundaries. Riemann problems appear in FV methods for the need of evaluating the fluxes at the element boundaries. Exact Riemann solvers are considered costly, thus approximate Riemann solvers have been developed to reduce the com-

putational cost. The commonly used methods to compute numerical fluxes include Roe flux, Lax-Friedrichs flux, Harten-Lax-Val Leer (HLL) flux, Osher flux, etc. A general discussion of these fluxes can be found in Toro (1999) and LeVeque (2002).

The main limitation of FV methods is the inability to extend to higher-order accuracy on general unstructured grids. Finite element methods, constructing local approximated solutions using piecewise polynomial test functions, enable high-order accuracy and remain the geometric flexibility. However, since the test functions are globally defined, for time-dependent problems with implicit scheme, it is disadvantagous to invert the globally defined mass matrix.

A special type of FE methods, discontinuous Galerkin (DG) methods, is introduced to wave problems in the past decades. DG methods, firstly proposed by Reed and Hill (1973) and then generalized for systems of hyperbolic conservation laws by the pioneering work of Cockburn et al. (e.g. Cockburn and Shu 1989, 1990, 1991, 1998; Cockburn et al. 1989), are in essence a combination of FV and FE methods, thus combine the merit of both. DG methods are capable of handling complex physical domains, capturing shocks, steep gradient and sharp fronts, and providing high-order approximations within elements with the use of high-order interpolating functions. Moreover, the elementwise formulation of DG methods enables local conservation of mass and momentum, makes the model highly parallelizable, and renders hp-adaptivity (here h is the mesh size and p is the polynomial degree) which allows locally refining the mesh and high-order approximations within elements. The high-order approximations make possible more accurate solutions on unstructured grids. One main drawback of DG methods, however, is that the employment of high-order polynomial brings in large degrees of freedom, which increases the computational cost. An extensive review of DG methods can be found in Cockburn et al. (2000).

DG methods are known well-suited for hyperbolic problems but with one potential disadvantage over continuous Galerking (CG) methods, that is the degrees of freedom in DG methods

are associated with the number of elements, while in CG methods they are associated with the number of nodes. By coupling a CG method with a DG method, the overall degrees of freedom can be reduced (Dawson and Proft 2002a) while still retaining a local conservative, flux continuous solution.

In this study, all of the aforementioned numerical methods are implemented into an Euler solver for water waves, and are utilized to investigate the wave-vegetation interaction. Particularly, a FD method is used to develop a non-hydrostatic wave model for studying the dispersion property of numerically simulated waves in Chapter 2. A hybrid DG-CG-FD scheme is developed to solve the Euler equations for fully dispersive highly nonlinear waves in Chapter 3. In Chapter 4, a fourth order FE method is utilized to solve the governing equation for vegetation motion with a fourth order derivative term, and the vegetation model is incorporated into a hybrid FV-FD Euler model to study the wave-vegetation interaction.

1.4 Objective and Outline

Although a number of open-source wave models exist, there is still a need to improve the accuracy and efficiency of wave models for practical applications. The distribution of variables in the water column controls the dispersion properties of non-hydrostatic models. Navier-Stokes or Euler models requires fine vertical resolutions to simulate highly dispersive waves in deep water. It is highly desirable to reduce the number of unknowns in the water column by placing them at optimal locations.

Finer vertical resolution is utilized near the free surface for capturing the rapid velocity and pressure variation while coarse resolution is used at the bottom due to the mild change of velocity and pressure in this region. Yuan and Wu (2006) presented a so-called top-down resolving (TDR) technique to determine a set of suitable layer thicknesses. Young and Wu (2009) provided the top-layer thickness for their two-layer non-hydrostatic model. For $kh =$

3.14, the top layer takes 50% of the water depth; for $kh = 6$, the top layer takes 39.3% of the water depth, and for $kh = 15$, the top layer takes 15.7% of the water depth.

However, there was no theoretical guidance for non-hydrostatic wave models to determine the layer distribution. One of the objectives of this study is to derive a theoretical dispersion relationship of waves simulated by non-hydrostatic models, and obtain the optimal layer distribution for a given tolerance dispersion error.

It is desirable to develop an efficient and accurate approach to solve Euler equations for fully dispersive and highly nonlinear water waves. DG methods, combining the merits of FV and FE methods, are capable of handling complex physical domains, capturing shocks, steep gradient and sharp fronts, and providing high-order approximations within elements with the use of high-order interpolating functions. Discontinuous Galerkin methods have been developed for nonlinear shallow water (NSW) equations, Boussinesq equations, and incompressible N-S equations; however, there are shortcomings: 1) NSW models are unable to accurately predict the propagation of short waves due to the hydrostatic assumption; 2) Boussinesq models lack varying velocities in the water column; and 3) N-S models are limited to flow problems in a small domain because of the expensive computational cost. There is no application of DG methods to solve Euler equations for water waves in a large area.

With respect to wave-vegetation interaction, although models with the capability of simulating wave interaction with vegetation have been developed already, they assume that either the vegetation stem is rigid or swaying in a linear or exponential pattern. In reality, vegetation stems may move like a cantilever or a whip driven by waves (Paul et al. 2012). The deflection of flexible vegetation, such as sedge Schoenoplectus americanus and seagrasses, exhibits a nonlinear whip-like motion, which cannot be approximated using linear or exponential functions. In such cases, solving the complete force balance equation for beam deformation is necessary.

However, there is no pre-existing model that solves the complete force balance equation for the vegetation motion coupled with a nonlinear, dispersive wave model.

The following scientific questions are addressed in this study. (1) What is the analytical dispersion relationship of waves simulated by an Euler model? (2) What is the optimal layer distributions for a given tolerance dispersion error? (3) Can this layer distribution be extended to non-linear waves case? (4) How can we devise a numerical scheme that combines the merits of DG, CG, and FD methods to achieve the optimal efficiency and accuracy of Euler wave model? (5) What is the relationship between the movements of single-stem vegetation and water particle? (6) How does the vegetation flexibility affect wave attenuation? In order to answer these questions, three research objectives are formulated as follows.

1) Derive a theoretical dispersion relationship of waves simulated by an Euler model, and obtain the optimal layer distribution for a given tolerance dispersion error;

2) Develop a hybrid discontinuous Galerkin, spectral element (SE), and finite difference (DG-SE-FD) scheme to solve the Euler equations for fully dispersive highly nonlinear waves with higher accuracy, hp-adaptivity and good dispersion property;

3) Develop a deformable vegetation model to investigate wave and vegetation interaction, and provide insights on the relationship between displacement of water particle and plant stem, as well as on vegetation flexibility on wave attenuation.

In Chapter 2, an analytical dispersion relationship of waves simulated by a non-hydrostatic Euler model is derived. The horizontal discretization and vertical discretization are separated. With infinitely small dx (horizontal element size) and dt (time step), a theoretical dispersion relationship of numerically simulated waves by non-hydrostatic wave models is derived from the semi-discretized governing equations. The phase speed of linear waves simulated by the semi-discretized Euler model is expressed as a rational polynomial function of the dimensionless water depth, kh, and the layer thicknesses encompassing the water column become optimiz-

able parameters in this function. The dispersion error is obtained by comparing this phase speed against the exact solution based on the linear wave theory. It is shown that for a given dispersion error (e.g. 1%), the range of kh can be extended if the layer thicknesses are optimally selected. The optimal two- and three-layer distributions for such Euler models are provided. Although the optimization method is applicable to all non-hydrostatic models, for demonstration purpose, an Euler model using FD method in a σ-coordinate is developed and utilized. The algorithm and numerical scheme presented in Zijlema and Stelling (2005) are applied. The derived phase speed is tested against both numerical and exact solutions of standing waves for various cases. The model is also tested using the fifth-order Stokes theory for nonlinear standing waves.

In Chapter 3, a hybrid nodal DG-SE-FD scheme is developed to solve the Euler equations for fully dispersive highly nonlinear waves. σ-coordinate is employed to allow high resolution near the bottom and capture the changing free surface. An Euler solver can generally be divided into hydrostatic and non-hydrostatic parts corresponding to procedures for solving hydrostatic and non-hydrostatic pressure. In the non-hydrostatic part, a Poisson equation needs to be solved. Horizontal and vertical derivatives can be treated with different numerical methods to combine the merit of each method. In this study, to take advantage of the high-order accuracy, hp-adaptivity, and geometry flexibility, the DG method is utilized for horizontal discretization in the hydrostatic part. The CG method is applied to solve the Poisson equation in the non-hydrostatic part for the sake of reducing the overall degrees of freedom, and the FD method is used for the vertical discretization. The third order strong stability-preserving Runge-Kutta method (SSP-RK) provides high-order temporal accuracy and minimize unphysical disturbances introduced by the time integration. The variables at the element interface are evaluated using the Lax-Friedrichs and HLL Riemann solvers. The model is tested for linear and nonlinear standing waves using analytical solutions. And the numerical dispersion relationship is verified using the theoretical dispersion relationship presented in Chapter 2.

In Chapter 4, a fully coupled wave-vegetation model for simulating the interaction between water waves and submerged flexible plants is presented. The governing equation for vegetation motion is solved by a high-order finite element method and an implicit time differencing scheme. A vegetation deformation model is developed, and the algorithm and numerical scheme by Ma et al. (2012) are implemented into the Euler solver. This fully coupled vegetation-wave model is rigorously verified by comparing numerical results with theoretical solutions for single swaying vegetation cases and with experimental data for large-scale swaying vegetation cases. A scaling analysis is performed on the governing equation for vegetation motion to understand the importance of each force involved in the vegetation vibration. For cases that damping becomes significant compared with other restoring forces, a theoretical relationship between movements of vegetation stem and water particle is derived, and a dimensionless parameter, incorporating characteristics of waves and material as well as geometric properties of vegetation is obtained. Finally, all the findings are summarized and conclusions are provided in Chapter 5.

CHAPTER 2 OPTIMIZATION OF NON-HYDROSTATIC EULER MODEL FOR WATER WAVES [1]

2.1 Introduction

In physical oceanography, and coastal and ocean engineering, an accurate and efficient prediction of surface waves is of paramount importance. In the past several decades with the rapid advances in computational technology, substantial efforts have been devoted to developing numerical models for simulating the propagation and evolution of water waves from deep water to the shoreline.

A widely used type of models is based on depth-averaged equations, such as Boussinesq-type models. The conventional Boussinesq models (e.g. Peregrine 1967) have the drawback of weak dispersion and weak nonlinearity, or a limited range of applicability. By introducing a reference velocity at an arbitrary vertical location as the velocity variable and choosing the location to match the Padé [2, 2] expansion of the exact linear dispersion relationship, Nwogu (1993) extended the applicability of the model to $kh \approx 3$, here k is the wave number, and h is the water depth. The dimensionless wave number kh serve as a dispersion criterion.

Many efforts have been put in to enhance the deep-water accuracy of the depth-integrated approach by developing high-order Boussinesq-type models. By utilizing a quartic polynomial approximation for the vertical profile of velocity field, Gobbi and Kirby (1999) developed a model with excellent linear dispersion properties up to $kh \approx 6$. The models of Madsen and Schäffer (1998), and Chen et al. (1998) also showed good linear dispersive wave properties up to $kh \approx 6$. Madsen et al. (2002) further improved the Boussinesq-type model and made it applicable to extremely deep-water waves with $kh \approx 40$. Agnon et al. (1999) presented a new procedure to achieve good nonlinear dispersion properties up to $kh \approx 6$.

[1] This chapter has appeared in "Coastal Engineering". Zhu, L., Chen, Q., and Wan, X., 2014. Optimization of non-hydrostatic Euler model for water waves. *Coast. Eng.* 91, 191-199. doi:10.1016/j.coastaleng.2014.06.003. It is reprinted by permission of Elsevier.

Lynett and Liu (2004a and 2004b) introduced another approach to improving the dispersion accuracy of Boussinesq-type models. Instead of using a high-order approximation for the vertical profile of the flow field, they used N independent quadratic polynomial approximations for the velocity profiles. These polynomial approximations match at the interfaces that divide the water column into N layers. Good dispersion accuracy up to $kh \approx 8$ was achieved with an optimized two-layer model. Chazel et al. (2009) combined the approach in Madsen et al. (2002) and the approach in Lynett and Liu (2004a), and developed an efficient model with less complexity. This model exhibits good linear and nonlinear dispersion properties to $kh \approx 10$.

Another widely used type of models is based on the Navier-Stokes equations (NSE) or the Euler equations of fluid motion. The momentum equations are solved at every layer for this type of models, thus the computational cost is higher compared with the Boussinesq type models. To capture the rapid changing free surface and to apply the pressure boundary condition precisely on the free surface of the waves, Navier-Stokes models involve the non-hydrostatic pressure on the top layer, and solve this problem by methods of: (1) employing edged-based grid systems (e.g. Lin and Li, 2002; Zijlema and Stelling, 2005, 2008; Zijlema et al., 2011; Chen et al., 2011; Ma et al., 2012), (2) using the integration method (e.g. Yuan and Wu, 2004), (3) implementing interpolation approaches (e.g. Walters, 2005; Choi and Wu, 2006; Young et al., 2007; Badiei et al., 2008), and (4) embedding Boussinesq-type like equation into the Navier-Stokes model (e.g. Wu et al., 2010).

To improve the model dispersion properties, non-uniform layer distribution has been used. Finer vertical resolution is utilized near the free surface for capturing the rapid velocity and pressure variation while coarse resolution is used at the bottom due to the mild change of velocity and pressure in this region. Yuan and Wu (2006) presented a so-called top-down resolving (TDR) technique to determine a set of suitable layer thicknesses. The basic concept of this technique is to keep a fine resolution from the top layers down to the one just above the bottom

layer, and use a coarse resolution for the bottom layer. With this TDR method, their model can achieve the same dispersion accuracy using 5 non-uniform layers rather than using 10 uniform layers for waves with $kh = 4$.

Young and Wu (2009) provided the top-layer thickness for their two-layer non-hydrostatic model. For $kh = 3.14$, the top layer takes 50% of the water depth; for $kh = 6$, top layer takes 39.3% of the water depth, and for $kh = 15$, top layer takes 15.7% of the water depth. However, the dependence of top layer thickness on kh values hinders the model application in resolving highly dispersive random waves. Young and Wu (2010) proposed an adapted top-layer control (ATLC) method that eliminates the model layer thickness dependence on kh. The basic concept is that the finer resolution of the top layer is given by $\Delta\sigma_N = 0.5/(N-1)$, where $\Delta\sigma_N$ is the top layer size, and N is the number of layers. The size of the rest layers exponentially stretches to the bottom layer. The top layer size is set as 50%, 25% and 12.5% for two-, three-, and five-layer models, respectively. For a given tolerance phase error of 1%, the two-, three-, and five-layer models are capable of resolving linear wave dispersion up to $kh = 3.14$, 6.28 and 15.7, respectively.

Zijlema and Stelling (2005, 2008) and Zijlema et al. (2011) proposed a non-hydrostatic, free-surface flow model, SWASH (an acronym of Simulating WAves till SHore) for simulating wave propagation from deep water to the surf zone, using a semi-implicit, staggered finite volume method. The adoption of the Keller-box scheme in this model enabled the pressure to be assigned at the free surface without any approximation, and also enabled good dispersion properties at very low vertical resolution (two or three layers). Using two uniform layers, for a 1% tolerance phase error, SWASH achieves good linear dispersion properties up to $kh \approx 7$ and 3 for standing waves and progressive waves, respectively. Using three uniform layers, for a 1% tolerance phase error, SWASH achieves good linear dispersion properties up to $kh \approx 7$ for progressive waves. Zijlema et al. (2011) suggested that adjusting layer thicknesses could signif-

icantly improve wave dispersion accuracy. With layer thicknesses tuned as 10%, 20%, 70% of the total water depth, their three-layer model is able to simulate waves with $kh \approx 15.7$ with a relatively small phase error.

Bai and Cheung (2013) provides theoretical dispersion relationships for an N-layer Boussinesq-type system. The derived dispersion relationships follow a $[2N-2, 2N]$ Padé expansion. The accumulative dispersion error is computed over $0.01 \leq kh \leq 6$ for covering a wide spectrum of ocean waves from deep water to shoreline. The layer arrangement appears as free parameter and can be adjusted for minimizing the accumulative dispersion error, and optimizing the proposed model. The two-layer model with the optimal layer arrangement of 50% - 50% of the water depth gives a minimum error of 3.445%. The three-layer model with the optimal layer arrangement of 29% - 32% - 39% of the water depth gives a minimum error of 3.09%.

Similar to Boussinesq-type models in which the location of the horizontal velocity in the water column controls the dispersion properties, the vertical distribution of the variables in non-hydrostatic free surface flow models dictates the model dispersion accuracy. Because solving the Poisson equation is the most time consuming part of a non-hydrostatic model, it is highly desirable to reduce the number of variables in the water column by placing them at optimal locations. The objective of our study is to derive an analytical dispersion relationship of a non-hydrostatic free surface flow model and optimize it for extremely dispersive and highly nonlinear waves with only two or three layers. Although the optimization method is applicable to all non-hydrostatic models, for the demonstration purpose, the present work chose an Euler model that uses the algorithm and numerical scheme presented in Zijlema and Stelling (2005), except using the finite difference method in a sigma-coordinate. In this chapter, we will present: (1) the derivation of the phase speed of linear waves simulated by the semi-discretized non-hydrostatic Euler model, and (2) the optimal two- and three-layer distributions. For a 1% tolerance dispersion error, the optimal two-layer distribution from bottom to top is 67% and 33% of the total

water depth and the Euler model is capable of simulating linear waves up to $kh = 9$. For a 1% tolerance dispersion error, the optimal three-layer distribution from bottom to top is 68%, 26.5% and 5.5% of the total water depth and the Euler model is capable of simulating extremely dispersive waves up to $kh = 49.5$.

Furthermore, nonlinear standing wave tests have been performed to examine the effect of nonlinearity. Kirby and Dalrymple (1986) proposed a nonlinear dispersion relation, which effectively approximated the dispersion characteristics of waves propagating from deep to shallow waters. The nonlinear effect was scaled by wave steepness ka_0, and the phase speed became a function of kh and ka_0. In this chapter, numerical experiments with different ka_0 are conducted. A fifth-order Stokes-type exact solution for standing waves (Sobey 2009) is utilized to test our model. We have found that the phase speed of nonlinear waves follows the analytically derived linear phase speed, although the discrepancy rises as ka_0 increases. Therefore the optimal layer distribution can also be applied to the nonlinear wave simulation.

2.2 The Euler model

2.2.1 Governing equations

The propagation of fully dispersive, nonlinear water waves is governed by the continuity equation and the incompressible Euler equations, which are written as

$$\frac{\partial u}{\partial x^*} + \frac{\partial w}{\partial z^*} = 0 \tag{2.1}$$

$$\frac{\partial u}{\partial t^*} + u\frac{\partial u}{\partial x^*} + w\frac{\partial u}{\partial z^*} + \frac{\partial p}{\partial x^*} = 0 \tag{2.2}$$

$$\frac{\partial w}{\partial t^*} + u\frac{\partial w}{\partial x^*} + w\frac{\partial w}{\partial z^*} + \frac{\partial p}{\partial z^*} = 0 \tag{2.3}$$

where, (x^*, z^*) is the Cartesian coordinates, u and w are the velocity components in the x^*-, z^*-direction respectively, p is the total pressure. p is normalized by the water density ρ, and divided into hydrostatic part $g(\eta - z^*)$ and non-hydrostatic part q. Here, g is the gravitational acceleration, and η is the free surface elevation.

The physical computational domain is vertically bounded by the bottom $z^* = -h(x^*)$ and the free surface $z^* = \eta(x^*, t^*)$. To accurately represent the uneven bottom and the time dependent free surface, a σ-coordinate (Phillips 1957) is adopted.

$$t = t^*, \quad x = x^*, \quad \sigma = \frac{z^* + h}{D} \tag{2.4}$$

where $D(x,t) = \eta(x,t) + h(x)$ is the total water depth. The mapped computational domain is a stationary rectangular area, with σ ranging from 0 to 1 corresponding to the bottom and the free surface, respectively. Based on the chain rule, the governing equations in the σ-coordinate (x, σ, t) take the forms

$$\frac{\partial u}{\partial x} + \frac{\partial u}{\partial \sigma}\frac{\partial \sigma}{\partial x^*} + \frac{\partial w}{\partial \sigma}\frac{\partial \sigma}{\partial z^*} = 0 \tag{2.5}$$

$$\frac{\partial u}{\partial t} + u\frac{\partial u}{\partial x} + w_\sigma\frac{\partial u}{\partial \sigma} + g\frac{\partial \eta}{\partial x} + \frac{\partial q}{\partial x} + \frac{\partial q}{\partial \sigma}\frac{\partial \sigma}{\partial x^*} = 0 \tag{2.6}$$

$$\frac{\partial w}{\partial t} + u\frac{\partial w}{\partial x} + w_\sigma\frac{\partial w}{\partial \sigma} + \frac{\partial q}{\partial \sigma}\frac{\partial \sigma}{\partial z^*} = 0 \tag{2.7}$$

where, u and w are components of velocity in the x- and σ- direction, respectively, and

$$w_\sigma = \frac{D\sigma}{Dt^*} = \frac{\partial \sigma}{\partial t^*} + u\frac{\partial \sigma}{\partial x^*} + w\frac{\partial \sigma}{\partial z^*} \tag{2.8}$$

$$\frac{\partial \sigma}{\partial x^*} = \frac{1}{D}\frac{\partial h}{\partial x} - \frac{\sigma}{D}\frac{\partial D}{\partial x}, \quad \frac{\partial \sigma}{\partial z^*} = \frac{1}{D}, \quad \frac{\partial \sigma}{\partial t^*} = -\frac{\sigma}{D}\frac{\partial D}{\partial t} \tag{2.9}$$

The kinematic boundary conditions at the free surface $(\sigma = 1)$ and the impermeable bottom $(\sigma = 0)$ are:

$$w|_{\sigma=1} = \frac{\partial \eta}{\partial t} + u\frac{\partial \eta}{\partial x} \tag{2.10}$$

$$w|_{\sigma=0} = -u\frac{\partial h}{\partial x} \tag{2.11}$$

The dynamic boundary condition at the free surface $(\sigma = 1)$ is zero atmospheric pressure

$$q|_{\sigma=1} = 0 \tag{2.12}$$

The depth-integrated continuity equation can be obtained by integrating Equation (2.1) through the water column. After applying the kinematic boundary conditions, the resulting equation in σ-coordinate reads

$$\frac{\partial \eta}{\partial t} + \frac{\partial}{\partial x}\left[D \int_0^1 u d\sigma \right] = 0 \tag{2.13}$$

Waves are generated at the inflow boundary by prescribing the velocities and the surface elevation from the linear wave theory. At the outflow boundary, a sponge zone with a width of two wave lengths is enforced to eliminate the wave reflection from the boundary. Inside the sponge zone, the primitive variables are attenuated in the following manner:

$$\eta_j = \eta_j / C_s, \quad u_j = u_j / C_s, \quad w_j = w_j / C_s \tag{2.14}$$

in which C_s is the damping coefficient defined by

$$C_s = (\alpha_s)^{{\gamma_s}^i}, \quad i = 0, \ \ldots, \ n \tag{2.15}$$

where α_s and γ_s are free parameters, and n is the number of grids in the sponge zone. Numerical tests showed that best elimination of reflected waves from the boundary is attained with $\alpha_s = 2$ and $\gamma_s = 0.88$ for short waves; whereas the so-called Sommerfeld radiation boundary condition needs to be utilized for long waves. Treatments of these two types of outflow boundary conditions can be found in Chen et al. (1999).

2.2.2 Numerical scheme and algorithm

The numerical method of this model follows the framework of SWASH (Zijlema and Stelling 2005). The discretization of the governing equations is based on the Crank-Nicholson method, which gives second order accuracy in space and time. The adoption of the Keller-box scheme in this model enabled the pressure at the free surface to be assigned with the dynamic boundary condition without any approximation, and also enabled good dispersion properties at very low vertical resolution (two or three layers). The computational domain in σ-coordinate is

divided into $NX \times NZ$ rectangular cells with width Δx and height $\Delta\sigma_k = \sigma_k - \sigma_{k-1},\ k = 1,\ \ldots,\ NZ$. The grid points in x- and σ-direction are denoted as

$$\{X \mid x_{i+1/2} = i\Delta x,\ \ i = 0,\ \ldots,\ NX\} \quad \text{and} \quad \{Z \mid \sigma_k = \sigma_{k-1} + \Delta\sigma_k,\ \ k = 1,\ \ldots,\ NZ\} \tag{2.16}$$

The velocity components are distributed in a staggered manner, (i.e. u and w are located at $(i + 1/2, k + 1/2)$ and (i, k), respectively). The non-hydrostatic pressure q is located at the same place as w in the Keller-box scheme. The free surface elevation, η, is defined at the center of the surface cell. Figure 2.1 illustrates the layout of the all variables in the Keller-box scheme.

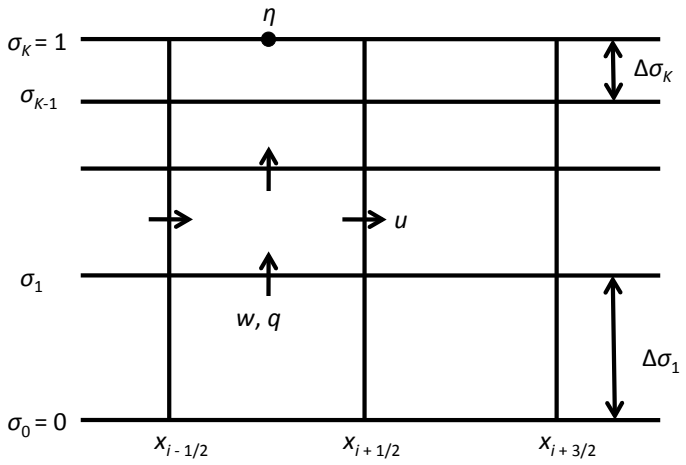

FIGURE 2.1. The layout of the variables in the Keller-box scheme

Owing to the implementation of the Keller-box scheme, instead of solving the vertical momentum equation (2.7) at the layer interface, where the vertical velocity w is located, we discretize it at the center of each layer

$$\frac{1}{2}\left(\frac{dw_j}{dt} + \frac{dw_{j-1}}{dt}\right) + u_{j+1/2}\frac{\partial w_{j+1/2}}{\partial x} + w_{\sigma j+1/2}\frac{\partial w_{j+1/2}}{\partial \sigma} + \frac{\partial q_{j+1/2}}{\partial \sigma}\frac{\partial \sigma_{j+1/2}}{\partial z^*} = 0 \tag{2.17}$$

with w_0 imposed by the bottom kinematic boundary condition. Central difference scheme is used to discretize the vertical derivative terms in the governing equations.

The algorithm can be decomposed into two phases to handle the hydrostatic and non-hydrostatic pressure separately. The employment of the pressure correction technique enables global mass conservation and local mass conservation. In the first phase (i.e. the hydrostatic phase), the hydrostatic part of the pressure, or the surface elevation (η), is computed. The horizontal moment equation (Equation (2.6)) and the depth-integrated continuity equation (Equation (2.13)) are discretized and coupled into a linear system of equations in $\Delta\eta$, which is the temporal change in the surface elevation. In the second phase (i.e. the non-hydrostatic phase), the non-hydrostatic part of the pressure, q, is computed. The boundary conditions with zero non-hydrostatic pressure at the free surface and zero pressure gradient at the bottom are applied to get closed solutions. The momentum equations (Equation (2.6) and (2.7)) and continuity equation (Equation (2.5)) are discretized and coupled into the Poisson equation in Δq, which is the temporal change in the non-hydrostatic pressure. The Poisson equation is solved by the HYPRE (http://acts.nersc.gov/hypre), a software library for solving large-scale linear systems of equations on massively parallel computers. The BiCGSTAB method (Van Der Vorst 1992) together with ILU preconditioner (Meijerink and Van Der Vorst 1977) is chosen from the library. Velocities u, w, and pressure q are updated in this phase. The sequence of the computation for a time step is summarized as follows, and more details about the numerical procedure can be found in Zijlema and Stelling (2005).

Hydrostatic Step:

1. Start from the previous time step with unknowns $\eta^n,\ u^n,\ w^n$, andq^n;

2. Solve Equation (2.18) for an intermediate horizontal velocity u^{**};

$$\frac{u^{**}-u^n}{\Delta t}+g\frac{\partial \eta^n}{\partial x}+\frac{\partial q^n}{\partial x}+\frac{\partial q^n}{\partial \sigma}\frac{\partial \sigma}{\partial x^*}=-u^n\frac{\partial u^n}{\partial x} \tag{2.18}$$

3. Solve a tridiagonal linear system (Equation (2.19)) to obtain the correction $\Delta\eta = \eta^{n+1} - \eta^n$ for water level;

$$\frac{\Delta\eta}{\Delta t} - g\theta^2\Delta t\frac{\partial}{\partial x}\Big[D^n \cdot \frac{\partial\Delta\eta}{\partial x}\Big] = -\theta\frac{\partial}{\partial x}\Big(D^n\sum_{j=1}^{NZ} u_j^{**}\Delta\sigma_j\Big) - (1-\theta)\frac{\partial}{\partial x}\Big(D^n\sum_{j=1}^{NZ} u_j^{n}\Delta\sigma_j\Big) \tag{2.19}$$

where j denotes layer index.

4. Correct the water level and horizontal velocity using Equations (2.20) and (2.21) for η^{n+1} and u^*

$$\eta^{n+1} = \eta^n + \Delta\eta \tag{2.20}$$

$$\frac{u^* - u^{**}}{\Delta t} + g\theta\frac{\partial\Delta\eta}{\partial x} = 0 \tag{2.21}$$

Non-hydrostatic Step:

1. Solve Equation (2.22) for intermediate velocities w^*;

$$\frac{1}{2}\left(\frac{w_j^* - w_j^n}{\Delta t} + \frac{w_{j-1}^* - w_{j-1}^n}{\Delta t}\right) + \frac{\partial q_{j+1/2}^n}{\partial\sigma}\frac{1}{D^n} = \Big(-u^n\frac{\partial w^n}{\partial x} - {w_\sigma}^n\cdot\frac{\partial w^n}{\partial\sigma}\Big)_{j+1/2} \tag{2.22}$$

2. Solve the Poisson equation (2.23) (an asymmetric linear system) for pressure correction Δq;

$$\begin{aligned}\frac{\partial}{\partial x}\left[\frac{\partial\Delta q}{\partial x} + \frac{\partial\Delta q}{\partial\sigma}\frac{\partial\sigma}{\partial x^*}\right] + \frac{\partial}{\partial\sigma}\left(\frac{\partial\Delta q}{\partial x}\frac{\partial\sigma}{\partial x^*}\right) + \left[\left(\frac{\partial\sigma}{\partial x^*}\right)^2 + \frac{1}{D^2}\right]\frac{\partial}{\partial\sigma}\left(\frac{\partial\Delta q}{\partial\sigma}\right) \\ = \frac{1}{\Delta t}\left(\frac{\partial u^*}{\partial x} + \frac{\partial u^*}{\partial\sigma}\frac{\partial\sigma}{\partial x^*} + \frac{1}{D}\frac{\partial w^*}{\partial\sigma}\right)\end{aligned} \tag{2.23}$$

3. Update the non-hydrostatic pressure and velocities using Equations (2.24), (2.25), and (2.26) for $u^{n+1},\ w^{n+1}$ and q^{n+1}

$$q^{n+1} = q^n + \Delta q \tag{2.24}$$

$$\frac{u^{n+1} - u^*}{\Delta t} + \theta\left[\frac{\partial\Delta q}{\partial x} + \frac{\partial\Delta q}{\partial\sigma}\frac{\partial\sigma}{\partial x^*}\right] = 0 \tag{2.25}$$

$$\frac{1}{2}\left(\frac{w_j^{n+1} - w_j^*}{\Delta t} + \frac{w_{j-1}^{n+1} - w_{j-1}^*}{\Delta t}\right) + \theta\frac{\partial\Delta q_{j+1/2}}{\partial\sigma}\frac{1}{D^n} = 0 \tag{2.26}$$

2.3 Model performance

The dispersion accuracy of the Euler model was examined through simulation of linear and non-linear dispersive waves. Tests results were compared with exact solutions from the linear wave theory. To study the capability of this model in resolving linear dispersion properties and nonlinear effect, three test cases are discussed in this section: (1) linear standing waves in a closed basin; (2) linear progressive waves in a flume; and (3) non-linear standing waves in a closed basin.

2.3.1 Linear standing waves

The numerical model was first tested against the exact solution of standing waves with an amplitude $a_0 = 0.1$ m in a 20 m long closed basin. Dispersive waves ($kh = 2\pi$) were simulated to test the accuracy of this model. The computational domain contains 200 grids with uniform spacing of 0.1 m in the horizontal direction, and two layers with uniform thickness in the vertical direction. The time step Δt was set as $T/400$, where T is the wave period. Figure 2.2 (upper panel) shows the comparison of the numerical and exact surface elevations at $x = 10$ m. The surface elevation was normalized by the wave amplitude a_0 and time was normalized by the wave period T. The computed surface elevations agree very well with the exact solution.

Define the relative dispersion error as $\Delta_e = |c_{model} - c_e| \ / \ c_e$. Figure 2.3 shows that the relative dispersion error reduces as the number of the layers increases, and approaches a constant. For highly dispersive waves, more layers are required for achieving sufficiently accurate results. Finer vertical resolution can help improve the dispersion accuracy, but the computational cost goes up quickly as the vertical resolution of a non-hydrostatic Euler model increases. For this reason, in Section 2.4, we present a method to achieve high dispersion accuracy using a small number of layers (e.g. two or three layers).

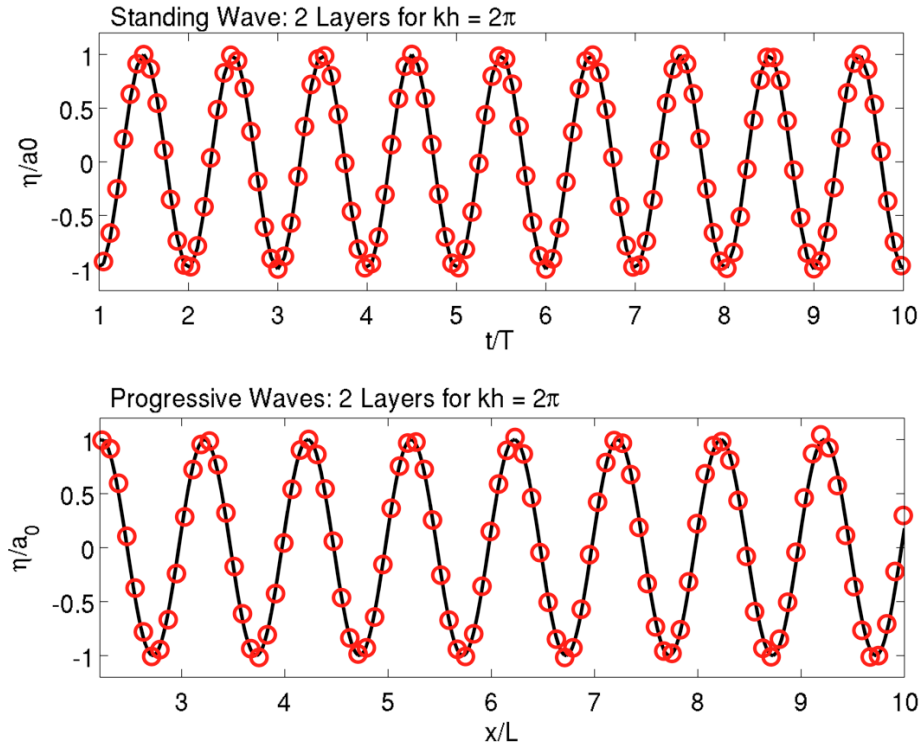

FIGURE 2.2. Comparisons between the numerical (circles) and exact (solid line) surface elevations for standing waves (upper panel) and progressive waves (lower panel) with $kh = 2\pi$ using two uniform layers.

2.3.2 Linear progressive waves on a flat bottom

The second test case is the linear progressive waves propagating in constant water depth. A wave train with amplitude $a_0 = 10^{-3}$ m and wavelength $L = 10$ m is generated at the left end of a 160 m long flume. The water depth is set as 10 m to make waves highly dispersive ($kh = 2\pi$). A 20 m long sponge zone is added at the right end of the flume to absorb the outgoing waves and minimize the reflection. The Courant number is defined as

$$Cr = \frac{\Delta t}{\Delta x}\left[\sqrt{gh} + \max(u)\right] \tag{2.27}$$

The computational domain used a uniform grid spacing of 0.2 m in the horizontal direction, and two layers with uniform thickness in the vertical direction. The time integration with respect to the convection terms is of explicit type. Thus, the Courant number was set as 0.1567, and the time step Δt was determined accordingly, which gives $\Delta t = T/800$, where T is the wave

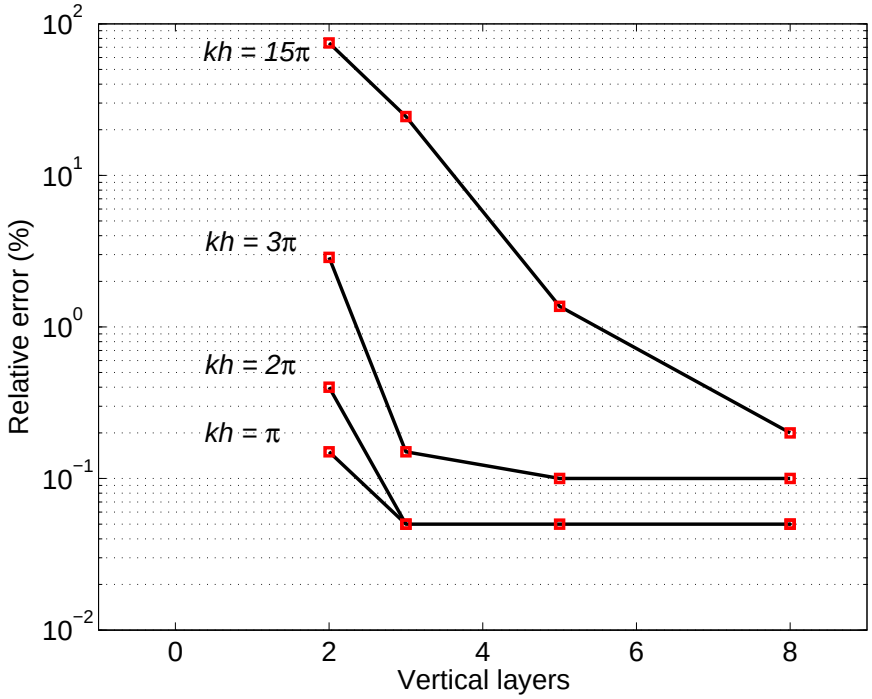

FIGURE 2.3. Relative dispersion error at $x = 10$ m as a function of the number of layers and wave dispersion parameter kh

period. The high horizontal and temporal resolution minimizes the discretization errors in the x direction and time. Figure 2.2 (lower panel) shows the comparisons of numerical and analytical surface elevations at $t = 80$ s. The surface elevation was normalized by the wave amplitude a_0 and time was normalized by the wave period T. The computed surface elevations agree well with the exact solution from the linear wave theory. The numerical result was taken one wave length from the left boundary to avoid small disturbances introduced by the inflow boundary.

2.4 Linear dispersion analysis

2.4.1 Linear dispersion properties for an N-layer model

In this section, the phase speed of linear waves simulated by the aforementioned non-hydrostatic Euler model is derived. The Keller-box scheme and the same layout of variables (i.e., velocities, pressure and surface elevation) are used in the derivation for the sake of consistency.

The dispersion error is obtained by comparing this phase speed against the analytical phase speed from the linear wave theory.

The linearized governing equations in the Cartesian coordinate are written as follows:

$$\frac{\partial u}{\partial x} + \frac{\partial w}{\partial z} = 0 \tag{2.28}$$

$$\frac{\partial u}{\partial t} + g\frac{\partial \eta}{\partial x} + \frac{\partial q}{\partial x} = 0 \tag{2.29}$$

$$\frac{\partial w}{\partial t} + \frac{\partial q}{\partial z} = 0 \tag{2.30}$$

$$\frac{\partial \eta}{\partial t} + \frac{\partial}{\partial x}\int_{-h}^{0} u dz = 0 \tag{2.31}$$

The computational domain is divided into N layers. The layer thickness is denoted as $\Delta z_j = \alpha_j h$ ($j = 1,\ 2,\ \ldots,\ N,$ from bottom layer to top layer), where Δz_j is the thickness of layer j; h is the water depth; α_j is the ratio of thickness of layer j to the water depth. α_j satisfies the equality $\sum \alpha_j = 1$.

The derivation starts with the quasi-discrete vertical momentum equation, obtained by discretizing Equation (2.30) in the vertical direction only.

$$\frac{1}{2}\left(\frac{\partial w_{j+1}}{\partial t} + \frac{\partial w_j}{\partial t}\right) + \frac{q_{j+1} - q_j}{\Delta z_{j+1}} = 0, \quad j = 0,\ \ldots,\ N-1 \tag{2.32}$$

The vertical momentum equation is discretized at the center of the layer, rather than at the interface of the layer. A flat bottom is considered here, thus $w_0 = 0$ and $\partial w_0/\partial t = 0$. The time derivative of vertical velocity is obtained from Equation (2.32).

$$\frac{\partial w_1}{\partial t} = -2\frac{q_1 - q_0}{\alpha_1 h} \tag{2.33}$$

$$\frac{\partial w_j}{\partial t} = -2\frac{q_j - q_{j-1}}{\alpha_j h} - \frac{\partial w_{j-1}}{\partial t}, \quad j = 2,\ \ldots,\ N \tag{2.34}$$

By taking the temporal derivative of Equation (2.28) and the spatial derivative of Equation (2.29), and doing subtraction, we get

$$\frac{1}{\Delta z_j}\left(\frac{\partial w_j}{\partial t}-\frac{\partial w_{j-1}}{\partial t}\right)-g\frac{\partial^2\eta}{\partial x^2}-\frac{1}{2}\left(\frac{\partial^2 q_j}{\partial x^2}+\frac{\partial^2 q_{j-1}}{\partial x^2}\right)=0,\quad j=1,\ \ldots,\ N \tag{2.35}$$

The time derivative of vertical velocity from Equation (2.33) and (2.34), and the free surface dynamic boundary condition (i.e. $q_N = 0$) are substituted into Equation (2.35), yielding

$$-2\frac{q_1-q_0}{\alpha_1^2h^2}-g\frac{\partial^2\eta}{\partial x^2}-\frac{1}{2}\left(\frac{\partial^2 q_1}{\partial x^2}+\frac{\partial^2 q_0}{\partial x^2}\right)=0 \tag{2.36}$$

$$-2\frac{q_j-q_{j-1}}{\alpha_j^2h^2}-4\sum_{s=1}^{N-1}(-1)^s\frac{q_{j-s}-q_{j-s-1}}{\alpha_{j-s}\alpha_j h^2}-g\frac{\partial^2\eta}{\partial x^2}-\frac{1}{2}\left(\frac{\partial^2 q_j}{\partial x^2}+\frac{\partial^2 q_{j-1}}{\partial x^2}\right)=0,\quad j=2,\ \ldots,\ N \tag{2.37}$$

The pressure, the horizontal velocity and the surface elevation can be expressed in harmonic forms

$$q_j=Q_je^{i\theta},\quad u_j=U_je^{i\theta},\quad \eta=Ae^{i\theta} \tag{2.38}$$

where $\theta = kx - \omega t$, k is the wave number, and ω is the angular frequency. According to the linear wave theory, the pressure can be further expressed as

$$q_j=m_jgAe^{i\theta} \tag{2.39}$$

Substituting Equation (2.39) into Equation (2.36) and (2.37) leads to a system of linear equations for m_j, which is

$$-2\frac{m_1-m_0}{\alpha_1^2}+(kh)^2+\frac{1}{2}\big(m_0+m_1\big)(kh)^2=0 \tag{2.40}$$

$$-2\frac{m_j-m_{j-1}}{\alpha_j^2}-4\sum_{s=1}^{k-1}(-1)^s\frac{m_{j-s}-m_{j-s-1}}{\alpha_{j-s}\alpha_j}+(kh)^2+\frac{1}{2}\big(m_j+m_{j-1}\big)(kh)^2=0,\quad j=2,\ \ldots,\ N \tag{2.41}$$

By virtue of the Cramer's rule (Cramer, 1750), m_j can be expressed as a rational polynomial function of kh, with the maximum power equals to $2N$. The ratios of layer thicknesses to the water depth (α_j) play as free parameters in this function.

Applying the rectangle rule to Equation (2.31) yields

$$\frac{\partial \eta}{\partial t} + \frac{\partial}{\partial x} \sum_{j=1}^{N} u_j \Delta z_j = 0 \tag{2.42}$$

By substituting the expression of m_j, and harmonic forms of u, q and η into Equation (2.29) and (2.31), a system of linear equations for U_j and A is obtained:

$$-\omega A + kh \sum_{j=1}^{N} \alpha_j U_j = 0 \tag{2.43}$$

$$\big[1 + \frac{1}{2}\big(m_j + m_{j-1}\big)\big] gkA - \omega U_j = 0, \quad j = 1, \ \ldots, \ N \tag{2.44}$$

In order to get a non-trivial solution for U_j and A, the determinant of the matrix must be equal to zero, which leads to the phase speed of linear waves simulated using this Euler model. The calculations were performed using MATHEMATICA.

2.4.2 Two-layer model

For a two layer model ($j = 2$), the pressure coefficients m_j can be expressed as:

$$m_0 = \frac{-2(a_1 - a_2 + a_3)(kh)^2}{(kh)^4 + (a_1 - 2a_2 + a_3)(kh)^2 + a_1 a_3} \tag{2.45}$$

$$m_1 = \frac{-2(kh)^4 - 2(a_1 - a_2)(kh)^2}{(kh)^4 + (a_1 - 2a_2 + a_3)(kh)^2 + a_1 a_3} \tag{2.46}$$

$$m_2 = 0 \tag{2.47}$$

where $a_1 = 4/\alpha_1^2, \ a_2 = -8/\alpha_1\alpha_2, \ a_3 = 4/\alpha_2^2$. The dispersion relationship for the two-layer model is expressed as

$$\omega^2 = gk\Big[kh\Big(1 + \frac{1}{2}\alpha_1(m_0 + m_1) + \frac{1}{2}\alpha_2 m_1\Big)\Big] \tag{2.48}$$

The phase speed c_{model} becomes

$$c_{model} = (gh)^{1/2}\Big[kh\Big(1 + \frac{1}{2}\alpha_1(m_0 + m_1) + \frac{1}{2}\alpha_2 m_1\Big)\Big]^{1/2} \tag{2.49}$$

The dispersion error is obtained by comparing this phase speed against the analytical phase speed, c_e, from the linear wave theory. The relative dispersion error $\Delta_e = |c_{model} - c_e| \ / \ c_e$ is obtained as

$$\Delta_e = \Big[\frac{kh}{\tanh(kh)}\Big(1 + \frac{1}{2}\alpha_1(m_0 + m_1) + \frac{1}{2}\alpha_2 m_1\Big)\Big]^{1/2} - 1 \tag{2.50}$$

For a 1% tolerance dispersion error, the two-equidistant-layer model can simulate waves with kh up to 7. This dispersion accuracy is consistent with that of SWASH. A simple loop algorithm is devised to find out the optimal layer thickness. Since α_1 plays as the only free parameter in the dispersion error expression for the two-layer model, we started at $\alpha_1 = 0.01$ (1% of water depth h) with increment of 0.001 and select the optimal α_1 to maximize the range of kh for a given tolerance dispersion error. A summary of the optimization results is shown in Table 2.1. For simulating waves with a fixed kh value, Equation (2.50) can be utilized to determine an appropriate layer distribution for achieving the minimum dispersion error.

TABLE 2.1. Optimal layer distribution for the two-layer model

Tolerance dispersion error (%)	Upper limit of kh range	Layer distribution (percentage of the water depth) from bottom to top
0.1	0.32	51% - 49%
0.5	0.86	50% - 50%
1	9.08	67% - 33%

To examine the model's dispersion properties, a series of numerical tests, both standing wave tests and progressive wave tests, were conducted. The phase errors were quantified and compared with the theoretically derived results (i.e. Equation (2.50)). Excellent agreement has been obtained although small discrepancies between numerical and analytical phase speeds were observed for progressive wave test cases because of the inflow and outflow boundary effect. In the following parts of this chapter, only standing wave test results are discussed. The wavelength L is fixed as 20 m, and the water depth h varies. The wave amplitude a_0 is set as 10^{-4} m to eliminate nonlinear effects.

Figure 2.4 shows the comparison of the relative phase errors obtained theoretically and numerically using equidistant (upper panel) and optimal (lower panel) layer distributions with a 1% tolerance dispersion error. The numerical results exhibit excellent agreement with the theoretical estimates, which indicates that the derived phase speed accurately represents the linear dispersion properties of this model. Figure 2.5 shows the theoretical and numerical phase speeds with the optimal layer distribution. The wave speeds were normalized by the exact solution from the linear wave theory. As seen in the inset, the simulated free surface elevations are in good agreement with the exact solution for $kh = 9.08$.

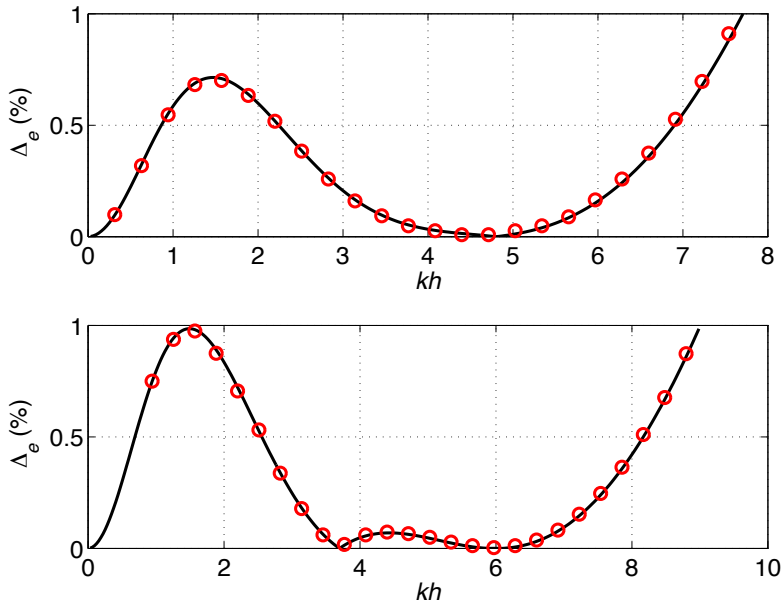

FIGURE 2.4. Comparison of the relative phase errors obtained theoretically (solid lines) and numerically (circles) using two equally distributed (upper panel) and optimally distributed (lower panel) layers bounded by a 1% tolerance dispersion error.

2.4.3 Three-layer model

For a three-layer model ($j = 3$), the pressure coefficient m_j can be expressed as:

$$m_0 = \frac{B_1^0(kh)^2 + B_2^0(kh)^4 + B_3^0(kh)^6}{C_0 + C_1(kh)^2 + C_2(kh)^4 + C_3(kh)^6} \tag{2.51}$$

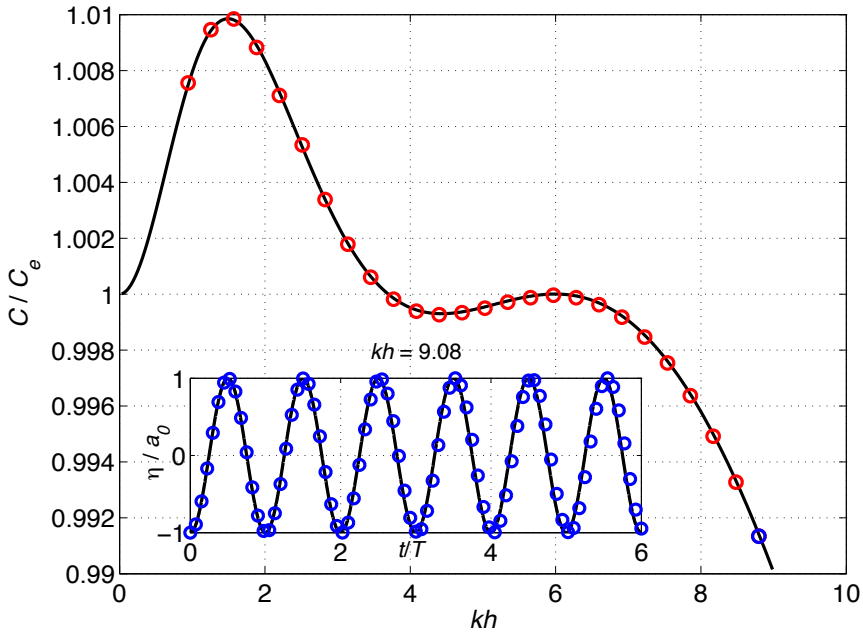

FIGURE 2.5. Comparison of the theoretically derived (solid line) and numerically obtained (circles) phase speeds with two optimally distributed layers. Inset: comparison of numerical (circles) and exact (solid line) solutions of surface elevations for $kh = 9.08$.

$$m_1 = \frac{B_1^1(kh)^2 + B_2^1(kh)^4}{C_0 + C_1(kh)^2 + C_2(kh)^4 + C_3(kh)^6} \tag{2.52}$$

$$m_2 = \frac{B_1^2(kh)^2 + B_2^2(kh)^4 + B_3^2(kh)^6}{C_0 + C_1(kh)^2 + C_2(kh)^4 + C_3(kh)^6} \tag{2.53}$$

$$m_3 = 0 \tag{2.54}$$

where the coefficients $B_1^0,\ B_2^0,\ B_1^1,\ B_2^1,\ B_1^2,\ B_2^2,\ B_3^2,\ C_0,\ C_1,\ C_2$ and C_3 are given in Appendix A. The dispersion relationship for the three-layer model is expressed as

$$\omega^2 = gk\left[kh\left(1 + \frac{1}{2}\alpha_1(m_0 + m_1) + \frac{1}{2}\alpha_2(m_1 + m_2) + \frac{1}{2}\alpha_3 m_2\right)\right] \tag{2.55}$$

The phase speed c_{model} becomes

$$c_{model} = (gh)^{1/2}\left[1 + \frac{1}{2}\alpha_1(m_0 + m_1) + \frac{1}{2}\alpha_2(m_1 + m_2) + \frac{1}{2}\alpha_3 m_2\right]^{1/2} \tag{2.56}$$

and the dispersion error Δ_e is obtained as

$$\Delta_e = \left[\frac{kh}{\tanh(kh)}\left(1 + \frac{1}{2}\alpha_1(m_0 + m_1) + \frac{1}{2}\alpha_2(m_1 + m_2) + \frac{1}{2}\alpha_3 m_2\right)\right]^{1/2} - 1 \tag{2.57}$$

For a 1% tolerance dispersion error, the three-equidistant-layer model can simulate waves with kh up to 16.4. Two variables α_1 and α_2 play as free parameters in the selection of the optimal layer thicknesses. A summary of the optimization results is shown in Table 2.2.

TABLE 2.2. Optimal layer distribution for the three-layer model

Tolerance dispersion error (%)	Upper limit of kh range	Layer distribution (percentage of the water depth) from bottom to top
0.1	0.5	33.4% - 33.3% - 33.3%
0.5	23.5	45% - 43% - 12%
1	49.5	68% - 26.5% - 5.5%

Figure 2.6 shows the comparison of the relative phase errors obtained theoretically and numerically using equidistant (upper panel) and optimal (lower panel) layer distributions bounded by a 1% tolerance dispersion error. The numerical results exhibit excellent agreement with the theoretical estimates. Figure 2.7 shows the theoretical and numerical phase speeds with the optimal layer distribution. The wave speeds were normalized by the exact solution from the linear wave theory. As seen in the inset, the simulated free surface elevations are in good agreement with the exact solution for $kh = 49.5$.

For the three-layer model, the highest polynomial order of kh in the numerator and denominator in the expression of phase speed reaches 6, compared with 4 for the two-layer model. This explains why the three-layer model can produce more accurate results than the two-layer model. The dispersion accuracy is drastically improved by increasing the number of layers or by using optimal layer distribution as shown in Figure 2.8.

2.5 Evaluation of the nonlinear effect

2.5.1 Nonlinearity parameter

The aforementioned dispersion relationships were derived assuming wave steepness ka (where a is the characteristic wave amplitude) was infinitely small, or $ka \ll 1$. However, for large amplitude waves, the wave properties and analytical dispersion relationships involve a

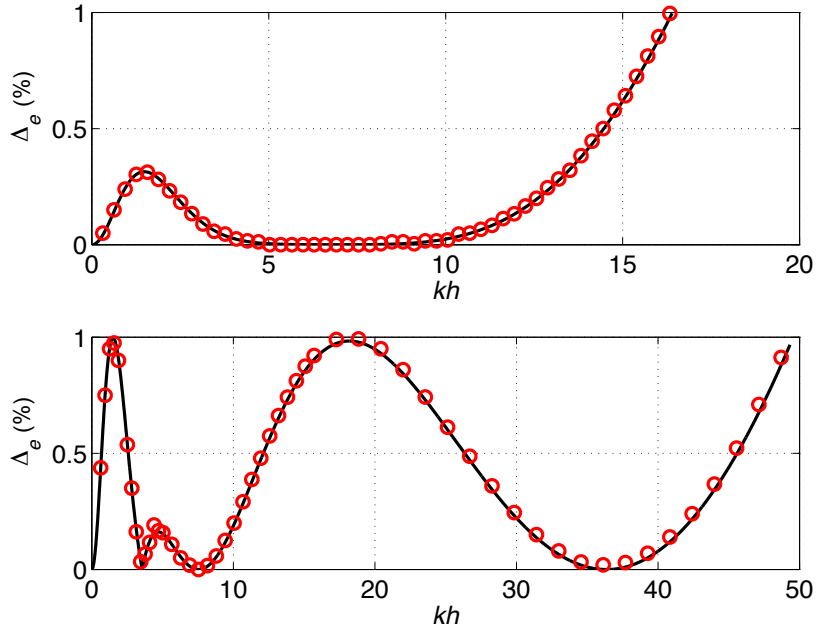

FIGURE 2.6. Comparison of the relative phase errors obtained theoretically (solid lines) and numerically (circles) using three equally distributed (upper panel) and optimally distributed (lower panel) layers bounded by a 1% tolerance dispersion error.

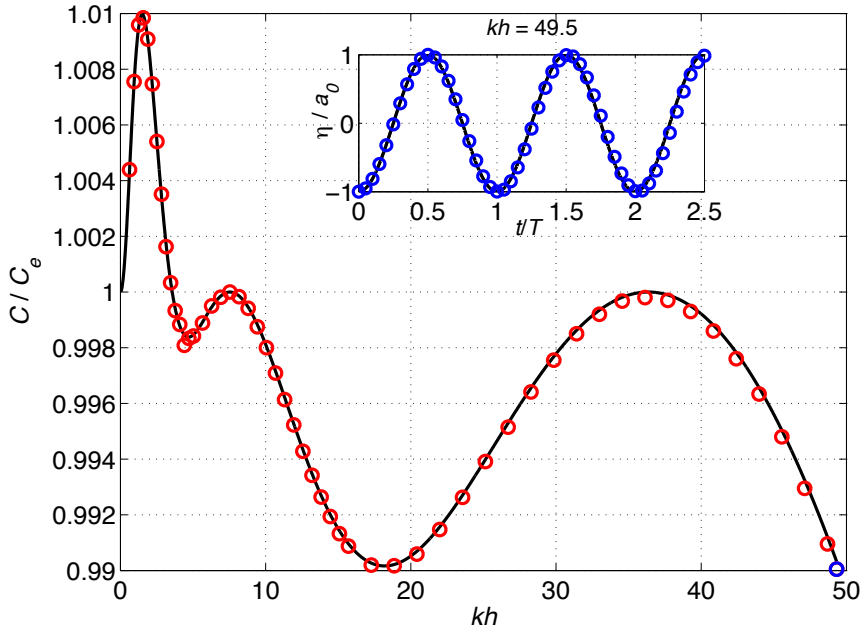

FIGURE 2.7. Comparison of the theoretically derived (solid line) and numerically obtained (circles) phase speeds with three optimally distributed layers. Inset: comparison of numerical (circles) and exact (solid line) solutions of surface elevations for $kh = 49.5$.

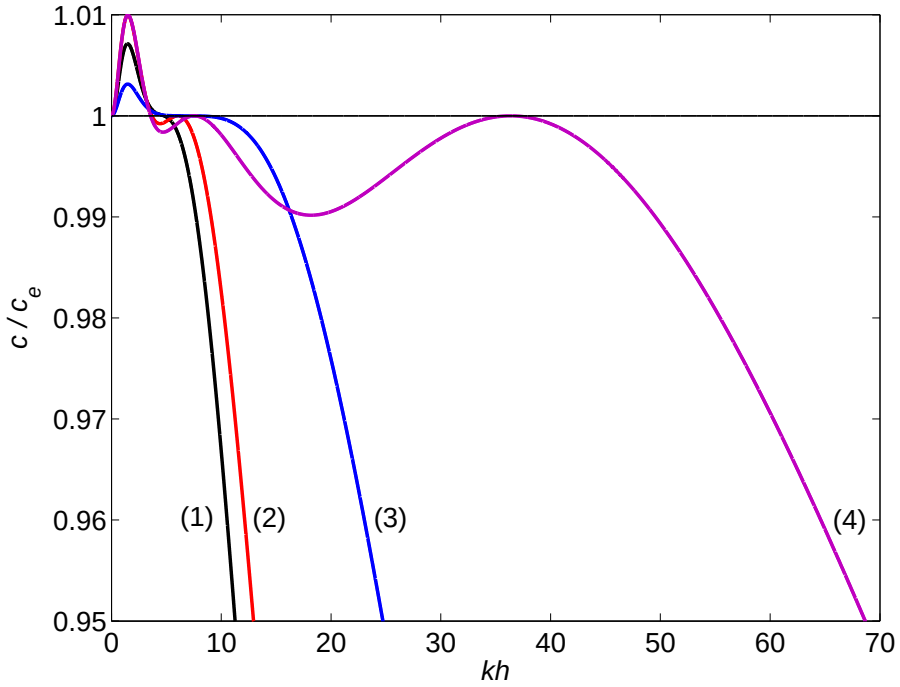

FIGURE 2.8. Comparison of relative phase speeds for the two-layer and three-layer model using equidistant and optimal layer distributions. Curve (1): Two layers with constant layer thickness; (2) Two layers with optimal layer distribution; (3): Three layers with constant layer thickness; (4): Three layers with optimal layer distribution.

power series of ka (e.g. Sobey 2009); therefore, the nonlinearity can be scaled by the wave steepness ka. The breaking criterion limits the maximum amplitude of wave to be $2a/L \approx 0.14$ $(ka \approx 0.44)$ in deep water (Michell 1893; Longuet-Higgins 1973). The derivation of dispersion relationship for nonlinear waves is not trivial due to nonlinear terms in the governing equations. However we can attain the dispersion curves numerically.

Nonlinear standing waves with an amplitude a_0 sloshing in a 20 m long closed basin were simulated to examine the performance of this Euler model in simulating nonlinear dispersive waves. Exact solutions, based on a fifth-order Stokes theory (Sobey 2009), were used to specify the initial conditions and verify the model results. The analytical solutions of surface elevation and velocities can be found in Appendix C. The non-linear dispersion relationship derived by

Sobey (2009) reads

$$(gk)^{1/2} \sum_{i=1}^{5} (ka_0)^{(i-1)} D_i = 2\pi/T \tag{2.58}$$

where D_i are dimensionless coefficients given in Appendix B. The phase speed, affected by the wave nonlinearity, becomes a function of kh and ka_0. The three-layer model using the optimal vertical layout was utilized to predict waves with four wave steepnesses, ranging from linear ($ka_0 = 0.000314$), weakly nonlinear ($ka_0 = 0.157$), strongly nonlinear ($ka_0 = 0.314$) to the wave breaking limit ($ka_0 = 0.44$). Also, for a given tolerance dispersion error (1%), the maximum kh is found for ka_0 ranging from 0.000314 to 0.44 with an increment of 0.05.

2.5.2 Numerical results

Figure 2.9 shows the comparison of the relative phase speeds (c/c_e) obtained theoretically (linear) and numerically (nonlinear) for the four types of waves. For nonlinear waves the phase speed follows a similar trend to the derived phase speed for linear waves but deviates proportionally with the increase of ka_0; therefore, the optimal layer distribution based on the linear dispersion relationship of the discretized Euler equations can also be utilized to simulate nonlinear waves within a range of ka_0 and kh. Table 2.3 lists the maximum kh for different ka_0 with the dispersion error limited to 1% . In practical applications, if ka_0 is known, a rough range of kh can be estimated and within this range the optimized model can provide numerical results with a dispersion error less than 1% .

Figure 2.10 shows the comparison of the modeled surface elevation and fifth-order Stokes solution (Sobey 2009) under four types of wave conditions corresponding to the maximum kh values of 49.50, 11.95, and 2.83, respectively. It is seen that the numerical model with the optimized layer thickness captures the wave nonlinearity quite well in comparison with the Stokes solutions of nonlinear stranding waves.

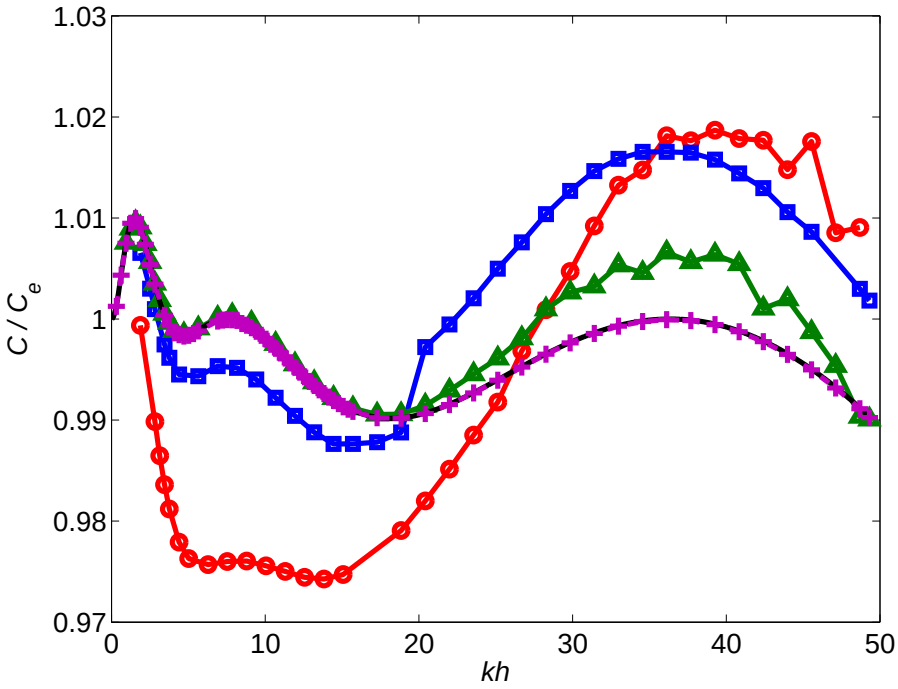

FIGURE 2.9. Comparison of relative phase speeds obtained from theoretical derivation (black solid line) and numerical experiments for linear waves ($ka_0 = 3e-4$, cross), weakly nonlinear waves ($ka_0 = 0.157$, triangle), strongly nonlinear waves ($ka_0 = 0.314$, square), and extremely nonlinear waves ($ka_0 = 0.440$, circle).

TABLE 2.3. The maximum kh for different ka_0 with 1% dispersion error.

ka_0	maximum kh
0.000314 - 0.16	49.50
0.2	13.82
0.25	12.57
0.314	11.94
0.35	4.40
0.4	3.45
0.44	2.83

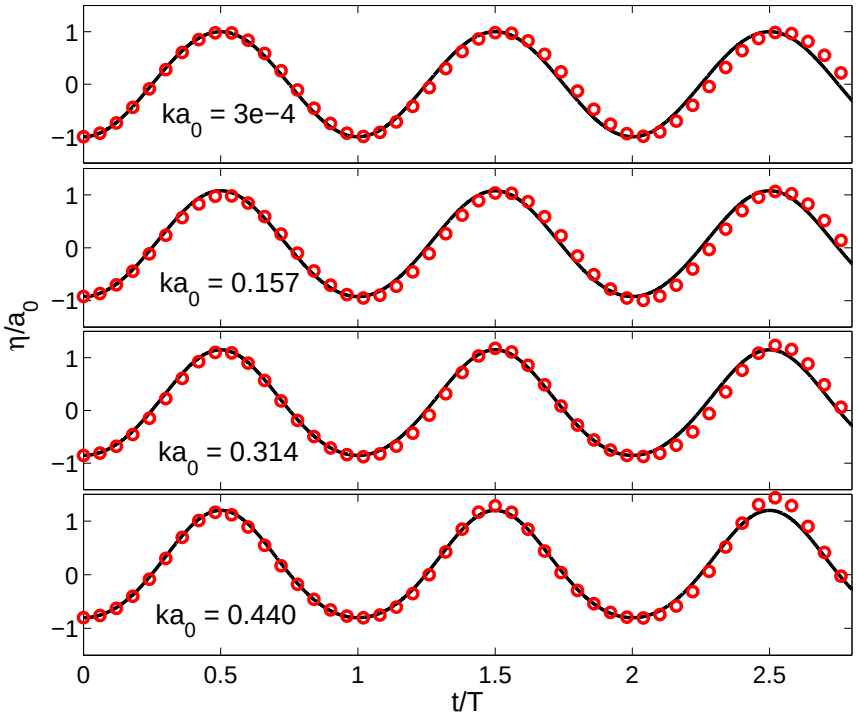

FIGURE 2.10. Comparison of numerical (circles) and fifth-order Stokes (solid line) solutions of surface elevations for linear waves ($ka_0 = 3e-4,$ and $kh = 49.50$), weakly nonlinear waves ($ka_0 = 0.157,$ and $kh = 49.50$), strongly nonlinear waves ($ka_0 = 0.314,$ and $kh = 11.94$), and extremely nonlinear waves ($ka_0 = 0.440,$ and $kh = 2.83$).

2.6 Conclusions

A model for simulating the propagation of fully dispersive, nonlinear water waves was developed following the Keller-box scheme and the numerical algorithm presented in the SWASH model. The aim of this chapter was to develop a theoretically sound method to optimize non-hydrostatic Euler models for extremely dispersive, nonlinear water waves. The key findings are as follows:

1. The theoretical phase speed of linear waves simulated by the non-hydrostatic Euler model is provided in this chapter. It is a rational polynomial function of the dimensionless water depth, kh, and the layer thicknesses encompassing the water column appear as free parameters in this function. The dispersion error thereupon is obtained by comparing this phase speed against the exact solution from the linear wave theory;

2. For a 1% tolerance dispersion error, the optimal layer distribution of a two-layer model from bottom to top is 67% and 33% of the water depth, and with this optimal layer distribution the model can simulate waves up to $kh = 9.08$;

3. For a 1% tolerance dispersion error, the optimal layer distribution of a three-layer model from bottom to top is 68%, 26.5% and 5.5% of the water depth, and with this optimal layer distribution the model can simulate waves up to $kh = 49.5$;

4. The phase speed of simulated nonlinear waves follows a trend similar to linear waves; therefore, the optimal layer distribution can be applied to nonlinear waves simulations as well. A table is provided for estimating the applicable range of kh for a given ka_0 to simulate nonlinear waves with less than a 1% dispersion error;

5. It has been shown that the derived dispersion relationships for two- and three-layer models are valid. Such a technique can be extended to any number of layers. Moreover, the methodology can be applied to other non-hydrostatic models for water waves to minimize the number of layers needed to simulate a wide spectrum of ocean waves from deep to shallow waters.

CHAPTER 3 A NEW APPROACH TO NON-HYDROSTATIC EULER MODEL FOR WATER WAVES

3.1 Introduction

In past two decades, discontinuous Galerkin (DG) methods have gain popularity in computational fluid dynamics owing to their high-order accuracy and geometric flexibility. The DG methods, firstly proposed by Reed and Hill (1973), have been generalized for systems of hyperbolic conservation laws by the pioneering work of Cockburn et al. (e.g. Cockburn and Shu 1989, 1990, 1991, 1998; Cockburn et al. 1989). The class of DG methods is in essence a combination of finite volume (FV) and finite element (FE) methods. It combines merits of both methods. An extensive review of DG methods can be found in Cockburn et al. (2000).

DG methods have been applied to shallow water equations (e.g. Aizinger et al. 2000; Aizinger and Dawson 2002; Blain and Massey 2005; Eskilsson and Sherwin 2004; Kubatko et al. 2006; Dawson et al. 2011; Lai and Khan 2012; Xing et al. 2010; Xing and Zhang 2013), Bousinessq-type equations (e.g. Eskilsson and Sherwin 2005, 2006; Engsig-Karup et al. 2006, 2008; Kesserwani et al. 2008a, 2008b), and compressible Euler equations for gas dynamics (e.g. San and Kara 2014; Tang and Warnecke 2005; Bassi et al. 2005). DG methods have also been applied to computational fluid dynamic (CFD) problems based on Navier-Stokes (N-S) equations, both compressible (e.g. Bassi and Rebay 1997; Hartmann and Houston 2006a, 2006b) and incompressible flows (e.g. Liu and Shu 2000; Cockburn et al. 2005a, 2005b; Grooss and Hesthaven 2006; Mozolevski et al. 2006; Shahbazi et al. 2007; Steinmoeller et al. 2013).

Eskilsson and Sherwind (2004) presented a modal spectral/hp element DG model for simulating nonlinear shallow water waves on unstructured triangular meshes. Optimal convergence was achieved for smooth problems. Unlike the CG models, in the dam-break test case, the Gibbs oscillations owing to the sharp gradients were confined to the neighboring of the shock fronts without polluting the solutions in the whole domain. Dawson et al. (2011) presented an appli-

cation of a DG method to hurricane storm surge modeling. Features such as handling spherical coordinates, maintaining still flows (well-balanced scheme), improving the slope-limiting (stability post-processing) were added to the DG method for capturing water overtopping of levees and other structures. Giraldo and Warburton (2008) presented a high-order nodal DG method for the two-dimensional oceanic nonlinear shallow water (NSW) equations. The adoption of straight-edged triangular elements obviates the need for a mass matrix, and better represents the continental coastlines for tsunami modeling. Test results show that the DG model is superior to the spectral element (SE) model for all polynomial orders and test cases considered. Xing et al. (2010) constructed high order DG methods for NSW equations, which can maintain the still water steady state exactly and preserve the non-negativity of the water height without violating mass conservation. Xing and Zhang (2013) extended the methods on unstructured triangular meshes. The positivity-preserving limiter is reformulated and the resulting scheme guarantees the positivity of the water depth.

DG methods are known well-suited for hyperbolic problems but with one potential disadvantage over continuous Galerkin (CG) methods, that is the degrees of freedom in DG methods are associated with the number of elements, while in the CG methods they are associated with the number of nodes. By coupling CG methods with DG, the overall degrees of freedom can be reduced while still retaining a local conservative, flux continuous solution. Dawson and Proft (2002a) developed and analyzed two approaches for shallow water flow modeling based on discontinuous and continuous approximating spaces. In the first approach, the primitive continuity equation was discretized using a DG method, while the momentum equation was approximated with a continuous approximation. In the second approach, both equations were solved by DG methods. A particular DG method, non-symmetric interior penalty Galerkin (NIPG) method (Riviere et al. 1999) was utilized for the momentum equation. Dawson and Proft (2002b) formulated a coupled DG-CG method for transport equations, where convection is dominant. Blain

and Massey (2005) presented a coupled DG-CG shallow water model to simulate coastal ocean dynamics. Dawson et al. (2006) proposed a new approach for the NSW equations by combining a DG method for solving continuity equation with a standard CG method for solving momentum equation. This model was compared with the advanced circulation (ADCIRC) model, which is based on the finite element methods.

Boussinesq-type equations are also commonly used in coastal engineering. Up to certain limits in dispersion, Boussinesq-type equations capture all the important nearshore wave phenomena including diffraction, refraction, nonlinear wave-wave interactions and wave-structure interactions. Eskilsson and Sherwind (2005, 2006) applied the DG method to the Boussinesq equations for weakly nonlinear, weakly dispersive water waves. A scalar method was employed to improve the computational efficiency for high-order expansions. Engsig-Karup et al. (2006) developed a nodal DG method solving a set of high-order Boussinesq-type equations for modelling highly nonlinear and dispersive water waves in one horizontal dimension. And later this method was extended to two horizontal dimensions by Engsig-Karup et al. (2008) and was demonstrated high accuracy in solving linear and weakly nonlinear wave-structure problems in complex domains of arbitrary shapes.

Since most Boussinesq-type models assume an irrotational or a partially-rotational flow field, they are valid up to the breaking point. Beyond the breaking point, vortices are generated, and any model neglecting the horizontal vorticity component will not be able to capture the vertical variation of wave-induced currents. An alternative to the Boussinesq modeling of surf-zone dynamics is the so-called Boussinesq-Green-Naghdi equations that retain the polynomial structure and rotational features in the velocity fields. Panda et al. (2014) presented a local DG (LDG) method for Boussinesq-Green-Naghdi equations. A stability analysis based on the Fourier transformation was carried out for the linearized equations and numerical tests were

conducted for testing not only linear dispersion properties but also non-linear transformation of dispersive waves.

The Boussinesq-Green-Naghdi equations are only capable of modeling nonlinear dispersive waves up to a certain limit in dispersion and assume polynomial approximations for the vertical profile of the velocity field. Another type of models is based on the incompressible N-S equations or the Euler equations of fluid motion.

Shahbazi et al. (2007) introduced an effective three-step algebraic splitting DG scheme for the incompressible N-S equations with explicit treatment of the nonlinear term and an implicit treatment of the Stokes operator. The interior penalty (IP) method was employed for the viscous term. Grooss and Hesthaven (2006) presented a nodal high-order DG method on a fully unstructured grid for unsteady free surface flows. The problem was treated as a two-fluid problem with the interface described by a level set.

An N-S or Euler solver can generally be divided into hydrostatic and non-hydrostatic parts corresponding to procedures for solving hydrostatic (or the surface elevation) and non-hydrostatic pressure. In the non-hydrostatic part, a Poisson equation, an elliptic problem for which the DG methods are not originally intended, is always yielded. For a unified analysis of DG methods for elliptic problems, the reader is referred to Arnold et al. (2000, 2002). An overview of the performance of DG methods with different fluxes can be found in Cockburn et al. (2000). The standard procedure in DG methods when discretizing second order derivatives is to split the system into two first order equations through the introduction of an auxiliary variable. The choice of flux at the element interfaces determines the type of DG formulation. Two commonly used DG formulations are the classical Bassi-Rebay (Bassi and Rebay 1997) and the LDG schemes (Cockburn and Shu 1998). Other formulations include the interior penalty (IP) method developed by Douglas et al. (1976).

The Poisson solver is considered as the most computationally expensive; therefore continuous approximations are more efficient compared with discontinuous approximations due to smaller degrees of freedom. Botti and Pietro (2011) presented a pressure-correction scheme for the incompressible N-S equations combining a DG approximation for the velocity and a standard CG approximation for the pressure. In particular, the velocity is approximated by modal shape functions (i.e. monomials), while pressure is discretized by means of nodal shape functions (i.e. Lagrange polynomials). Liu and Shu (2000) developed a DG method for the two-dimensional incompressible N-S equations in the vorticity stream-function formulation. The momentum equation is treated explicitly using a DG method and the stream function is obtained by a standard Poisson solver using a continuous Galerkin method.

How to choose the numerical flux at the element boundaries is an essential component of the DG methods. The selection of numerical flux is problem-dependent. For practical applications involving large-amplitude waves, discontinuous flows or shocks, models with a careful design of numerical flux (e.g. Bradford and Sanders 2005; Ma 2012) can circumvent the spurious oscillations caused by the nonlinear nature of the problem. Approximate Riemann solvers, such as Lax-Friedrichs flux, Roe flux (Roe 1981), Engquist-Osher (Engquist and Osher 1981), Harten-Lax-Van Leer (HLL) or Harten-Lax-van Leer-Contact (HLLC) flux (Toro et al. 1994), etc., provide a wide range of choices. The commonly used numerical flux for wave problems are Lax-Friedrichs flux (e.g. Engisg-Karup et al. 2007, Xing et al. 2010), local Lax-Friedrichs flux (e.g. Dawson et al. 2011) and HLL/HLLC flux (e.g. Eskilsson et al. 2011; Ma et al. 2012; Schwanenberg and Harms 2004 ; Tassi et al. 2007). A comprehensive discussion and details of different numerical fluxes can be found in LeVeque (2002). A study of the performance of the Runge-Kutta DG method based on different numerical fluxes is provided by Qiu et al. (2006). Shock-capturing methods, such as essentially non-oscillatory (e.g. Shu and Oscher 1988), monotone upwind, total variation diminishing (e.g. Harten 1983; Gottlieb and

Shu 1998; Zhang and Shu 2010) have been proposed to suppress unphysical oscillations around shocks and discontinuities. Such techniques render stability and robustness of models without degrading the high-order accuracy. San and Kara (2014) investigated the performance of the extended high-resolution shock capturing schemes by solving hyperbolic conservation laws in gas dynamics.

The primary objective of this chapter is to develop an efficient and accurate approach to solve Euler equations for fully dispersive and highly nonlinear water waves. DG methods, combining the merits of FV and FE methods, are capable of handling complex physical domains, capturing shocks, steep gradient and sharp fronts, and providing high-order approximations within elements with the use of high-order interpolating functions. Moreover, the elementwise formulation of DG methods enables local conservation of mass and momentum, makes the model highly parallelizable, and renders hp-adaptivity (here h is the mesh size and p is the polynomial degree) which allows locally refining the mesh and high-order approximations within elements. The high-order approximations make possible more accurate solutions on unstructured grids.

One main drawback of DG methods is that the employment of high-order polynomial brings in large degrees of freedom, which increase the computational cost. Coupling a CG method, in particular a SE method with DG, can greatly reduce the overall degrees of freedom.

Although DG methods have been developed for nonlinear shallow water (NSW) equations, Boussinesq equations, and incompressible N-S equations, there are shortcomings like: 1) NSW models are unable to accurately predict the propagation of short waves due to the hydrostatic assumption, 2) Boussinesq models lack varying velocities throughout the water column, and 3) N-S models are limited to small scale flow problems because of the expensive computational cost. There is no application of DG methods to solve Euler equations for water waves in a large area.

The Keller-box scheme (Zijlema and Stelling 2005, 2008; Zhu et al. 2014) based on the FD method is suitable for simulating highly dispersive waves with a relatively small number of layers in the vertical direction (two or three layers). The merits of DG, SE, and FD methods are combined by applying all three methods to the Euler solver for horizontal discretization in the hydrostatic part, horizontal discretization in the Poisson equation, and vertical discretization for the whole model, respectively. The numerical libraries provided by Hesthaven and Warburton (2007) have been extended to solve the hydrostatic part of the model. To obtain third-order temporal accuracy, a three-stage optimal Strong Stability-Preserving Runge-Kutta (SSP-RK) scheme (Gottlieb et al. 2001) is employed for time integration.

3.2 Governing equations and boundary conditions

3.2.1 Governing equations

The propagation of fully dispersive, nonlinear water waves is governed by the continuity equation and the incompressible Euler equations, which in Cartesian coordinates (x^*, z^*) are written as

$$\frac{\partial D}{\partial t^*} + \frac{\partial Du}{\partial x^*} + \frac{\partial Dw}{\partial z^*} = 0 \tag{3.1}$$

$$\frac{\partial Du}{\partial t^*} + \frac{\partial Duu}{\partial x^*} + \frac{\partial Duw}{\partial z^*} + D\frac{\partial p}{\partial x^*} = 0 \tag{3.2}$$

$$\frac{\partial Dw}{\partial t^*} + \frac{\partial Duw}{\partial x^*} + \frac{\partial Dww}{\partial z^*} + D\frac{\partial p}{\partial z^*} = 0 \tag{3.3}$$

where u and w are the velocity components in the x^*-, z^*-direction respectively, p is the total pressure. The physical computational domain is vertically bounded by the bottom $z^* = -h(x^*)$ and the free surface $z^* = \eta(x^*,\, t^*)$. $D(x^*,\, t^*) = \eta(x^*,\, t^*) + h(x^*)$ is the total water depth. To accurately represent the uneven bottom and the time dependent free surface, a σ-coordinate (Phillips 1957) is adopted.

$$t = t^*, \quad x = x^*, \quad \sigma = \frac{z^* + h}{D} \tag{3.4}$$

The mapped computational domain is a stationary rectangular area, with σ ranging from 0 to 1 corresponding to the bottom and the free surface, respectively. Normalize the total pressure p by the water density ρ, and divide it into hydrostatic part $g(\eta - z^*)$ and non-hydrostatic part q. Here, g is the gravitational acceleration. Applying the chain rule, the governing equations in the σ-coordinate $(x,\ \sigma,\ t)$ become

$$\frac{\partial D}{\partial t} + \frac{\partial Du}{\partial x} + \frac{\partial w_\sigma}{\partial \sigma} = 0 \tag{3.5}$$

$$\frac{\partial Du}{\partial t} + \frac{\partial}{\partial x}\Big[(Du)^2/D + \frac{1}{2}gD^2\Big] + \frac{\partial u w_\sigma}{\partial \sigma} - gD\frac{\partial h}{\partial x} + D\bigg(\frac{\partial q}{\partial x} + \frac{\partial q}{\partial \sigma}\frac{\partial \sigma}{\partial x^*}\bigg) = 0 \tag{3.6}$$

$$\frac{\partial Dw}{\partial t} + \frac{\partial}{\partial x}\Big(Duw\Big) + \frac{\partial w w_\sigma}{\partial \sigma} + D\bigg(\frac{\partial q}{\partial \sigma}\frac{\partial \sigma}{\partial z^*}\bigg) = 0 \tag{3.7}$$

where u and w are components of velocity in the x- and σ- direction, respectively, and

$$w_\sigma = D\frac{d\sigma}{dt^*} = D\bigg(\frac{\partial \sigma}{\partial t^*} + u\frac{\partial \sigma}{\partial x^*} + w\frac{\partial \sigma}{\partial z^*}\bigg) \tag{3.8}$$

$$\frac{\partial \sigma}{\partial x^*} = \frac{1}{D}\frac{\partial h}{\partial x} - \frac{\sigma}{D}\frac{\partial D}{\partial x}, \quad \frac{\partial \sigma}{\partial z^*} = \frac{1}{D}, \quad \frac{\partial \sigma}{\partial t^*} = \frac{1}{D}\frac{\partial h}{\partial t} - \frac{\sigma}{D}\frac{\partial D}{\partial t} \tag{3.9}$$

The kinematic boundary conditions at the free surface $(\sigma = 1)$ and the impermeable bottom $(\sigma = 0)$ are:

$$w|_{\sigma=1} = \frac{\partial \eta}{\partial t} + u\frac{\partial \eta}{\partial x} \tag{3.10}$$

$$w|_{\sigma=0} = -u\frac{\partial h}{\partial x} \tag{3.11}$$

The dynamic boundary condition at the free surface $(\sigma = 1)$ is zero atmospheric pressure

$$q|_{\sigma=1} = 0 \tag{3.12}$$

The depth-integrated continuity equation can be obtained by integrating Equation (3.1) through the water column. After applying the kinematic boundary conditions, the resulting equation in σ-coordinate reads

$$\frac{\partial \eta}{\partial t} + \frac{\partial}{\partial x}\bigg[D\int_0^1 u d\sigma\bigg] = 0 \tag{3.13}$$

To achieve high dispersion accuracy with two or three layers throughout the water column, we only apply the DG approach for discretizations in x-direction, and use FD method for discretizations in σ-direction to keep the merit of Keller-box scheme. The governing equations in Equation (3.6), (3.7) and (3.13) can be reformulated in a compact vector form

$$\frac{\partial \mathbf{U}}{\partial t} + \frac{\partial \mathbf{F}(\mathbf{U})}{\partial x} = \mathbf{S}(\mathbf{U}) \tag{3.14}$$

where $\mathbf{U} = [D,\ Du,\ Dw]^\top$ is the primary unknown variables. $\mathbf{F}(\mathbf{U}) = \big[\int_0^1 (Du)d\sigma,\ (Du)^2/D + \frac{1}{2}gD^2,\ (Du)(Dw)/D\big]^T$ is the numerical flux. The superscript "$\top$" denotes the transpose. $\mathbf{S}(\mathbf{U})$ is the quasi-source term including $\mathbf{S}_\sigma$, $\mathbf{S_h}$ and $\mathbf{S_p}$

$$\mathbf{S}_\sigma = \begin{bmatrix} 0 \\ -\frac{\partial u\omega_\sigma}{\partial \sigma} \\ -\frac{\partial w\omega_\sigma}{\partial \sigma} \end{bmatrix},\ \mathbf{S_h} = \begin{bmatrix} 0 \\ gD\frac{\partial h}{\partial x} \\ 0 \end{bmatrix},\ \mathbf{S_p} = \begin{bmatrix} 0 \\ -D\big(\frac{\partial q}{\partial x} + \frac{\partial q}{\partial \sigma}\frac{\partial \sigma}{\partial x^*}\big) \\ -D\big(\frac{\partial q}{\partial \sigma}\frac{\partial \sigma}{\partial z^*}\big) \end{bmatrix}$$

3.2.2 Boundary conditions

Boundary conditions are required at all boundaries of the physical domain to obtain a unique solution. The present model includes the following types of boundaries:

(i) At the free surface, the zero atmospheric pressure ($q = 0$) is enforced when solving the Poisson equation. The normal velocity w at the free surface can either be obtained by solving the momentum equation or be enforced by the kinematic boundary condition

$$w|_{\sigma=1} = \frac{\partial \eta}{\partial t} + u\frac{\partial h}{\partial x} \tag{3.15}$$

(ii) At the bottom, the normal velocity w is specified with the kinematic boundary condition.

$$w|_{\sigma=0} = -\frac{\partial h}{\partial t} - u\frac{\partial h}{\partial x} \tag{3.16}$$

(iii) At the closed boundaries, free-slip boundary conditions are imposed, which means that both the normal velocity and the tangential stress are set to zero. The pressure gradient is set to zero in the Poisson equation.

3.3 Numerical method

In this paper, we present a non-hydrostatic wave model using DG and SE methods for the horizontal discretization and a FD method for the vertical discretization. More specifically, in the hydrostatic phase, a nodal DG formulation is applied to horizontally discretize Equation (3.14) to obtain discontinuous approximations of the surface elevation and velocities, while in the non-hydrostatic phase, a SE formulation is applied to horizontally discretize the Poisson equation to obtain continuous approximations of the non-hydrostatic pressure. The Keller-box scheme (Keller 1971; Lam and Simpson 1976), based on a FD method, has the capability of resolving frequency dispersion accurately with low vertical resolution (two or three layers) (Zhu et al. 2014). The FD formulation is applied to vertically discretize Equation (3.14) and the Poisson equation. The computational domain in σ-coordinate $[0,\ L] \times [0,\ 1]$ is divided into $NX \times NZ$ rectangular cells with width of Δx and height of $\Delta\sigma_k = \sigma_{k+1} - \sigma_k,\ (k = 1,\ \ldots,\ NZ)$. The grid points in x- and σ-direction are denoted as

$$\{x_i \mid x_i = i\Delta x,\ \ i = 0,\ \ldots,\ NX\} \quad \text{and} \quad \{\sigma_{k+1} \mid \sigma_{k+1} = \sigma_k + \Delta\sigma_k,\ \ k = 1,\ \ldots,\ NZ\} \tag{3.17}$$

The velocity components are distributed in a vertically-staggered manner, (i.e. u and w are located at $(i, k+1/2)$ and (i, k), respectively). The free surface elevation η is defined at (i) and the non-hydrostatic pressure q at (i, k). The pressure is defined at the layer interface due to the implementation of the Keller-box scheme. Therefore, the zero pressure boundary condition at the free surface can be enforced without approximation. Figure 3.1 illustrates the layout of the all variables.

3.3.1 The discontinuous Galerkin horizontal discretization

The non-overlapping elements in x-direction is denoted by $I^k = [x_k,\ x_{k+1}]$. The superscript "k" is the element index. In each element the local approximate solution $\mathbf{U}_h^k$ is represented

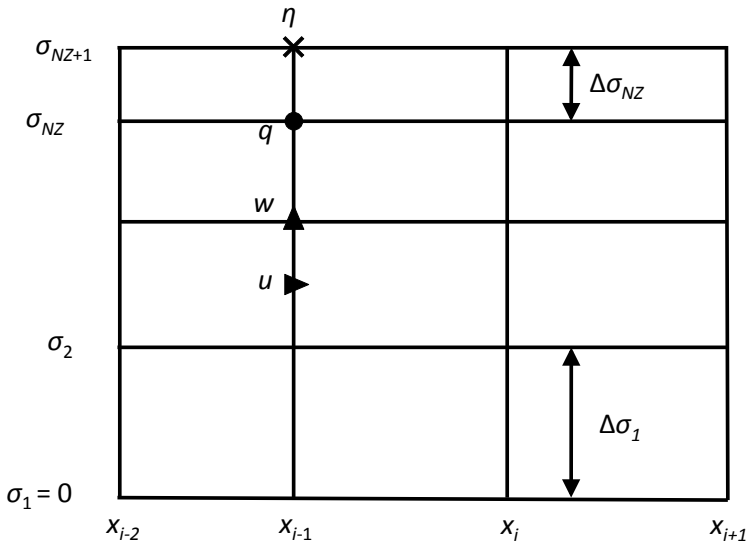

FIGURE 3.1. The layout of the variables

by a Lagrange interpolating polynomial of order $N_p - 1$ based on local nodes x_i^k as

$$x \in I^k : \quad \mathbf{U}^k(x,\, t) \approx \mathbf{U}_h^k(x,\, t) = \sum_{i=1}^{N_p} \mathbf{U}_h^k(x_i^k,\, t) l_i^k(x) \tag{3.18}$$

where $l_i^k(x)$ is the ith Lagrange interpolating polynomial. The subscript "h" indicates that it is an approximate solution. The weak elementwise formulation of Equation (3.14) is

$$\int_{I^k} \left(\frac{\partial \mathbf{U}}{\partial t} + \frac{\partial \mathbf{F}(\mathbf{U})}{\partial x} \right) l_i^k(x) dx = \int_{I^k} \mathbf{S}(\mathbf{U}) l_i^k(x) dx \tag{3.19}$$

Integration by parts twice yields the strong formulation

$$\int_{I_k} \Big(\frac{\partial \mathbf{U}_h^k}{\partial t} + \frac{\partial \mathbf{F}_h^k}{\partial x} \Big) l_i^k(x) dx = \oint_{\partial I^k} \hat{\mathbf{n}} \cdot (\mathbf{F}_h^k - \mathbf{F}^*) l_i^k(x) dx + \int_{I_k} \mathbf{S}_h^k l_i^k(x) dx \tag{3.20}$$

where $\hat{\mathbf{n}}$ is the outward pointing normal vector on element boundary ∂I^k. The numerical flux $\mathbf{F}^*$ is the solution at the element boudary. The specification of numerical flux is crucial since it passes information between adjacent elements. The choices for the numerical flux are problem-dependent. A comprehensive discussion of fluxes and approximated Riemann solvers can be

found in LeVeque (2002). Techniques for designing appropriate fluxes to minimize the dissipation can be found in Burmann and Steamm (2007) and Cockburn and Dong (2007). In this chapter, we use Lax-Friedrichs flux:

$$\mathbf{F}^*(\mathbf{U}_h^-,\ \mathbf{U}_h^+) = \frac{1}{2}\big[\mathbf{F}(\mathbf{U}_h^-) + \mathbf{F}(\mathbf{U}_h^+)\big] + \frac{c}{2}\big(\mathbf{U}_h^+ - \mathbf{U}_h^-\big) \tag{3.21}$$

where $c = \max\ \big(|u| + \sqrt{gh}\big)$ is the maximum wave speed. For the sake of simplicity, we only present the elementwise operation of the u-momentum equation. The momentum equations in other directions and the free-surface governing equation can be treated in a similar way. Also the superscript "k" and subscript "h" are omitted for simplicity. The u-momentum component in Equation (3.20) is

$$\int_I \Big(\frac{\partial U}{\partial t} + \frac{\partial (F^u)}{\partial x}\Big) \cdot l_i(x)dx = \oint_{\partial I} \hat{\mathbf{n}} \cdot ((F^u) - (F^u)^*) \cdot l_i(x)dx + \int_I S^u \cdot l_i(x)dx \tag{3.22}$$

where $U = Du$. The superscript "u" denotes the corresponding u-component in Equation (3.20). Within each element, the unknowns are defined at local quadrature points. Putting them in a vector form yields $\vec{U} = \big[U(x_1),\ U(x_2),\ \cdots,\ U(x_{Np})\ \big]^\top$. $\vec{F^u}$ and $\vec{S^u}$ are defined as $\vec{F^u} = F^u(\vec{U})$ and $\vec{S^u} = S^u(\vec{U})$. Three operators M, Q, H are defined as

$$M_{ij} = \int_I l_i l_j dx, \quad Q_{ij} = \int_I l_i \frac{dl_j}{dx} dx \quad , \quad H_{ij} = \oint_{\partial I} l_i l_j dx \tag{3.23}$$

To facilitate the computations, we map the kth element $x \in [x_k,\ x_{k+1}]$ onto a reference interval $\zeta \in [-1,\ 1]$ by

$$x(\zeta) = x_k + \frac{\Delta x}{2}(1 + \zeta) \tag{3.24}$$

The local Gauss-Lobatto-Legendre points $\{x_i\}_{i=1,\,2,\,...,\,N_p}$ are then mapped to $\{\zeta_i\}_{i=1,\,2,\,...,\,N_p}$. The matrices in Equation (3.23) become

$$M_{ij} = \frac{\Delta x}{2}\int_{-1}^{1} l_i(\zeta) l_j(\zeta) d\zeta, \quad Q_{ij} = \int_{-1}^{1} l_i(\zeta)\frac{dl_j}{d\zeta} d\zeta, \quad H_{ij} = \oint_{-1}^{1} l_i(\zeta) l_j(\zeta) d\zeta \tag{3.25}$$

and Equation (3.22) becomes

$$M \cdot \frac{d\vec{U}}{dt} + Q \cdot \vec{F^u} = H\left(\hat{\mathbf{n}} \cdot \left(\vec{F^u} - \vec{F^u}^*\right)\right) + M \cdot \vec{S^u} \tag{3.26}$$

Define an operator $\mathscr{L}(\vec{U}) = -(M)^{-1} \cdot Q \cdot \vec{F^u} + (M)^{-1} \cdot H\left(\hat{\mathbf{n}} \cdot \left(\vec{F^u} - \vec{F^u}^*\right)\right) + \vec{S^u}$. Equation (3.26) can be written as a system of ODE

$$\frac{d\vec{U}}{dt} = \mathscr{L}(\vec{U}) \tag{3.27}$$

The implementation of stability post-processing or slope limiter is desirable and necessary to prevent non-physical oscillations. The classic MUSCL (Monotone Upstream-centered Scheme for Conservation Laws) limiter (Thomas 1999; LeVeque 2002) is employed in this model. Details on this limiter can be found in Hesthaven and Warburton (2008).

3.3.2 Vertical discretization

Owing to the implementation of the Keller-box scheme, instead of solving the vertical momentum equation at the layer interface, where the vertical velocity w is located, we discretize it at the center of each layer

$$\frac{1}{2}\left(\frac{d\vec{W}_j}{dt} + \frac{d\vec{W}_{j-1}}{dt}\right) = \mathscr{L}(\vec{W}_{j-1/2}) \tag{3.28}$$

with $\vec{W}_0$ imposed by the bottom kinematic boundary condition. The second-order central difference scheme is used to discretize the vertical derivative terms in the governing equations. In the Poisson equation, the boundary conditions with zero non-hydrostatic pressure at the free surface and zero pressure gradient at the bottom are applied to close the system.

Keller-box scheme is advantageous for highly dispersive waves because it takes the average of the vertical momentum equation at both the upper and lower interfaces of the same layer. As demonstrated in Stelling and Zijlema (2003), the accuracy of the frequency dispersion for relative short waves can be significantly improved by applying the Keller-box method. Zhu et al. (2014) presents an analytical dispersion relationship of a numerical model with Keller-box

scheme. For a 1% tolerance dispersion error, the Euler model with uniform two-layer distribution is capable of simulating linear waves up to $kh = 7.7$, and with the optimal two-layer distribution (67% and 33% of the total water depth from bottom to top) the model is capable of simulating linear waves up to $kh = 9.1$, where kh is the dimensionless wave number, representing the dispersion property of the waves.

3.3.3 The Runge-Kutta time discretization

The optimal third-order three-stage Strong Stability-Preserving Runge-Kutta (SSP-RK) (Gottlieb et al. 2001) method is adopted for time integration. At each stage, the free-surface governing equation is treated explicitly, the momentum equations are handled with a projection method. At each stage, the computation procedure can be divided into two phases, hydrostatic and non-hydrostatic. In the hydrostatic phase, the hydrostatic part of the pressure, or the surface elevation, and intermediate velocities are computed, whereas in the non-hydrostatic phase, the non-hydrostatic pressure is computed and velocities are updated. The slope limiter is applied at each stage of the SSP-RK scheme. The procedure of stage I is illustrated as follows.

Hydrostatic phase at stage I:

The continuity equation is discretized as

$$\frac{\vec{D}^{(1)} - \vec{D}^{n}}{\Delta t} = -(M)^{-1} \cdot Q \cdot \vec{F^{D}} + (M)^{-1} \cdot H\left(\hat{\mathbf{n}} \cdot \left(\vec{F^{D}} - \vec{F^{D}}^{*}\right)\right) + \vec{S_{\mathbf{h}}^{D}} \tag{3.29}$$

The non-hydrostatic pressure, q, is excluded from the momentum equations at this phase. The momentum equations are discretized as

$$\frac{\vec{U}^{*} - \vec{U}^{n}}{\Delta t} = -(M)^{-1} \cdot Q \cdot \vec{F^{u}} + (M)^{-1} \cdot H\left(\hat{\mathbf{n}} \cdot \left(\vec{F^{u}} - \vec{F^{u}}^{*}\right)\right) + \vec{S_{\mathbf{h}}^{u}} + \vec{S_{\sigma}^{u}} \tag{3.30}$$

$$\frac{\vec{W}^{*} - \vec{W}^{n}}{\Delta t} = -(M)^{-1} \cdot Q \cdot \vec{F^{w}} + (M)^{-1} \cdot H\left(\hat{\mathbf{n}} \cdot \left(\vec{F^{w}} - \vec{F^{w}}^{*}\right)\right) + \vec{S_{\mathbf{h}}^{w}} + \vec{S_{\sigma}^{w}} \tag{3.31}$$

with the superscript "$*$" for U and W denoting intermediate values.

Non-hydrostatic phase at stage I:

$$\frac{\vec{U}^{(1)} - \vec{U}^{*}}{\Delta t} = \vec{S_{\mathbf{P}}^{u}} \tag{3.32}$$

$$\frac{\vec{W}^{(1)} - \vec{W}^{*}}{\Delta t} = \vec{S_{\mathbf{P}}^{w}} \tag{3.33}$$

For simplicity, we use the notations of $\frac{\vec{W}^{*}-\vec{W}^{n}}{\Delta t}$ and $\frac{\vec{W}^{(1)}-\vec{W}^{*}}{\Delta t}$ in Equation (3.31) and (3.33) to represent the averaged vertical momentum equation as shown in Equation (3.28). Substituting Equation (3.31) and (3.33) into the continuity equation

$$\frac{\partial u}{\partial x} + \frac{\partial u}{\partial \sigma}\frac{\partial \sigma}{\partial x^{*}} + \frac{\partial w}{\partial \sigma}\frac{\partial \sigma}{\partial z^{*}} = 0 \tag{3.34}$$

yields a Poisson equation in σ-coordinate

$$\frac{\partial}{\partial x}\left[\frac{\partial q}{\partial x}+\frac{\partial q}{\partial \sigma}\frac{\partial \sigma}{\partial x^{*}}\right]+\frac{\partial}{\partial \sigma}\left(\frac{\partial q}{\partial x}\frac{\partial \sigma}{\partial x^{*}}\right)+\left[\left(\frac{\partial \sigma}{\partial x^{*}}\right)^{2}+\frac{1}{D^{2}}\right]\frac{\partial}{\partial \sigma}\left(\frac{\partial q}{\partial \sigma}\right) = \frac{1}{\Delta t}\left(\frac{\partial u^{*}}{\partial x}+\frac{\partial u^{*}}{\partial \sigma}\frac{\partial \sigma}{\partial x^{*}}+\frac{1}{D}\frac{\partial w^{*}}{\partial \sigma}\right) \tag{3.35}$$

A SE method is utilized to solve the Poisson equation as described in Section 3.3.4. The solution to the Poisson equation updates velocities in the non-hydrostatic phase, which give the final first stage estimates $(\vec{D}^{(1)},\ \vec{U}^{(1)},\ \vec{W}^{(1)})$.

The same procedure is followed at stage II and results in $(\vec{D}^{(2)},\ \vec{U}^{(2)},\ \vec{W}^{(2)})$. According to the three-stage SSP-RK method, we update the final estimates of unknowns at stage II through the following formulation

$$\left(\vec{D}^{(2)},\ \vec{U}^{(2)},\ \vec{W}^{(2)}\right) = \frac{3}{4}\left(\vec{D}^{n},\ \vec{U}^{n},\ \vec{W}^{n}\right) + \frac{1}{4}\left(\vec{D}^{(2)},\ \vec{U}^{(2)},\ \vec{W}^{(2)}\right) \tag{3.36}$$

Stage III results in $(\vec{D}^{(3)},\ \vec{U}^{(3)},\ \vec{W}^{(3)})$ and the final estimates of unknowns at stage III are

$$\left(\vec{D}^{n+1},\ \vec{U}^{n+1},\ \vec{W}^{n+1}\right) = \left(\vec{D}^{(3)},\ \vec{U}^{(3)},\ \vec{W}^{(3)}\right) = \frac{1}{3}\left(\vec{D}^{n},\ \vec{U}^{n},\ \vec{W}^{n}\right) + \frac{2}{3}\left(\vec{D}^{(3)},\ \vec{U}^{(3)},\ \vec{W}^{(3)}\right) \tag{3.37}$$

3.3.4 Discretizations of the Poisson equation

A hybrid FD-SE formulation is employed to discretize the Poisson equation (3.35). A second-order central differencing method is utilized for the vertical discretization and a SE method is employed for the horizontal discretization. Equation (3.35) can be re-written as

$$\frac{\partial^2 q}{\partial x^2} + r_1(x,\ \sigma)\frac{\partial^2 q}{\partial x \partial \sigma} + r_2(x,\ \sigma)\frac{\partial^2 q}{\partial \sigma^2} + r_3(x,\ \sigma)\frac{\partial q}{\partial \sigma} = r_4(x,\ \sigma) \tag{3.38}$$

with

$$r_1(x,\ \sigma) = 2\frac{\partial \sigma}{\partial x^*}, \quad r_2(x,\ \sigma) = \left(\frac{\partial \sigma}{\partial x^*}\right)^2 + \frac{1}{D^2}, \quad r_3(x,\ \sigma) = \frac{\partial}{\partial x}\left(\frac{\partial \sigma}{\partial x^*}\right) \tag{3.39}$$

and

$$r_4(x,\ \sigma) = \frac{1}{\Delta t}\left(\frac{\partial u^*}{\partial x} + \frac{\partial u^*}{\partial \sigma}\frac{\partial \sigma}{\partial x^*} + \frac{1}{D}\frac{\partial w^*}{\partial \sigma}\right) \tag{3.40}$$

At jth-layer, the discretized form of Equation (3.38) becomes

$$\begin{aligned}
\frac{d^2 q^{(j)}}{dx^2} \quad &+ \quad r_1^{(j)} \cdot \frac{1}{2\Delta\sigma_j \Delta\sigma_{j-1}} \cdot \left[\Delta\sigma_{j-1}\frac{dq^{(j+1)}}{dx} - \Delta\sigma_j \frac{dq^{(j-1)}}{dx} + (\Delta\sigma_j - \Delta\sigma_{j-1})\frac{dq^{(j)}}{dx}\right] \\
&+ \quad r_2^{(j)} \cdot \frac{1}{0.5\Delta\sigma_j \Delta\sigma_{j-1}(\Delta\sigma_j + \Delta\sigma_{j-1})} \cdot \left[\Delta\sigma_{j-1} q^{(j+1)} + \Delta\sigma_j q^{(j-1)} - (\Delta\sigma_{j-1} + \Delta\sigma_j) q^{(j)}\right] \\
&+ \quad r_3^{(j)} \cdot \frac{1}{2\Delta\sigma_j \Delta\sigma_{j-1}} \cdot \left[\Delta\sigma_{j-1} q^{(j+1)} - \Delta\sigma_j q^{(j-1)} + (\Delta\sigma_j - \Delta\sigma_{j-1}) q^{(j)}\right] = r_4^{(j)}
\end{aligned} \tag{3.41}$$

where the superscript "(j)" is the layer index. Organizing Equation (3.41) yields

$$\frac{d^2 q^{(j)}}{dx^2} + a^{(j)}\frac{dq^{(j)}}{dx} + b^{(j)} q^{(j)} + c^{(j)}\frac{dq^{(j-1)}}{dx} + g^{(j)} q^{(j-1)} + e^{(j)}\frac{dq^{(j+1)}}{dx} + f^{(j)} q^{(j+1)} = r_4^{(j)}. \tag{3.42}$$

Following the Galerkin method, we multiply Equation (3.42) by the Lagrange interpolation polynomial $l_n(x)$, integrate by parts the first term on the left-hand side, and re-arrange the formulation into

$$\begin{aligned}
\int_0^L \frac{dq^{(j)}}{dx}\frac{dl_n}{dx}dx \quad &+ \quad \int_0^L a^{(j)}\frac{dq^{(j)}}{dx} l_n dx + \int_0^L b^{(j)} q^{(j)} l_n dx \\
&+ \quad \int_0^L c^{(j)}\frac{dq^{(j-1)}}{dx} l_n dx + \int_0^L g^{(j)} q^{(j-1)} l_n dx \\
&+ \quad \int_0^L e^{(j)}\frac{dq^{(j+1)}}{dx} l_n dx + \int_0^L f^{(j)} q^{(j+1)} l_n dx = \int_0^L r_4^{(j)} l_n dx
\end{aligned} \tag{3.43}$$

Over element $I^k = [x_k,\ x_{k+1}]$, the non-hydrostatic pressure $q^{(j)}$ can be approximated as

$$q^{(j)^k}(x) \approx \sum_{i=1}^{m} q^{(j)^k}(x_i^k) l_i^k(x) \tag{3.44}$$

where $\{x_i^k\}_{i=1,\,2,\,...,\,m}$ is a set of local Gauss-Lobatto-Legendre points, $q^{(j)^k}(x_i^k)$ is the unknown nodal value, and the superscript "k" is the element index. For simplicity the superscript "k" is omitted.

In this approach, we employ equal-order velocity and pressure approximations; thus the same set of Gauss-Lobatto-Legendre points are utilized in both DG and SE formulations. Applying the mapping in Equation (3.24) yields the following elementwise formulation

$$\begin{aligned}\frac{2}{\Delta x}\int_{-1}^{1}\frac{dq^{(j)}}{d\zeta}\frac{dl_n}{d\zeta}d\zeta \quad &+ \quad \int_{-1}^{1} a^{(j)}\frac{dq^{(j)}}{d\zeta}l_n d\zeta + \frac{\Delta x}{2}\int_{-1}^{1} b^{(j)}q^{(j)}l_n d\zeta \\ &+ \quad \int_{-1}^{1} c^{(j)}\frac{dq^{(j-1)}}{d\zeta}l_n d\zeta + \frac{\Delta x}{2}\int_{-1}^{1} g^{(j)}q^{(j-1)}l_n d\zeta \\ &+ \quad \int_{-1}^{1} e^{(j)}\frac{dq^{(j+1)}}{d\zeta}l_n d\zeta + \frac{\Delta x}{2}\int_{-1}^{1} f^{(j)}q^{(j+1)}l_n d\zeta = \frac{\Delta x}{2}\int_{-1}^{1} r_4^{(j)}l_n d\zeta\end{aligned} \tag{3.45}$$

The coefficients $a^{(j)},\ b^{(j)},\ c^{(j)},\ g^{(j)},\ e^{(j)},\ f^{(j)}$ and $r_4^{(j)}$ can be approximated as

$$a^{(j)}(\zeta) \approx \sum_{i=1}^{m} a^{(j)}(\zeta_i)l_i(\zeta),\quad b^{(j)}(\zeta) \approx \sum_{i=1}^{m} b^{(j)}(\zeta_i)l_i(\zeta),\quad c^{(j)}(\zeta) \approx \sum_{i=1}^{m} c^{(j)}(\zeta_i)l_i(\zeta) \tag{3.46}$$

$$g^{(j)}(\zeta) \approx \sum_{i=1}^{m} g^{(j)}(\zeta_i)l_i(\zeta),\quad e^{(j)}(\zeta) \approx \sum_{i=1}^{m} e^{(j)}(\zeta_i)l_i(\zeta),\quad f^{(j)}(\zeta) \approx \sum_{i=1}^{m} f^{(j)}(\zeta_i)l_i(\zeta) \tag{3.47}$$

and

$$r_4{}^{(j)}(\zeta) \approx \sum_{i=1}^{m} r_4{}^{(j)}(\zeta_i)l_i(\zeta) \tag{3.48}$$

Substituting the approximations in Equations (3.44), (3.46), (3.47) and (3.48) into Equation (3.45) yields

$$\frac{2}{\Delta x}\sum_{i=1}^{Np} q^{(j)}(\zeta_i)\int_{-1}^{1}\frac{dl_i}{d\zeta}\frac{dl_n}{d\zeta}d\zeta+\sum_{i=1}^{Np}\sum_{s=1}^{Np} q^{(j)}(\zeta_i)a^{(j)}(\zeta_s)\int_{-1}^{1}\frac{dl_i}{d\zeta}l_s l_n d\zeta+$$
$$\frac{\Delta x}{2}\sum_{i=1}^{Np}\sum_{s=1}^{Np} q^{(j)}(\zeta_i)b^{(j)}(\zeta_s)\int_{-1}^{1} l_s l_i l_n d\zeta+\sum_{i=1}^{Np}\sum_{s=1}^{Np} q^{(j-1)}(\zeta_i)c^{(j)}(\zeta_s)\int_{-1}^{1}\frac{dl_i}{d\zeta}l_s l_n d\zeta+$$
$$\frac{\Delta x}{2}\sum_{i=1}^{Np}\sum_{s=1}^{Np} q^{(j-1)}(\zeta_i)g^{(j)}(\zeta_s)\int_{-1}^{1} l_s l_i l_n d\zeta+\sum_{i=1}^{Np}\sum_{s=1}^{Np} q^{(j+1)}(\zeta_i)e^{(j)}(\zeta_s)\int_{-1}^{1}\frac{dl_i}{d\zeta}l_s l_n d\zeta+$$
$$\frac{\Delta x}{2}\sum_{i=1}^{Np}\sum_{s=1}^{Np} q^{(j+1)}(\zeta_i)f^{(j)}(\zeta_s)\int_{-1}^{1} l_s l_i l_n d\zeta=\frac{\Delta x}{2}\sum_{s=1}^{Np} r_4^{(j)}(\zeta_i)\int_{-1}^{1} l_s l_n d\zeta \tag{3.49}$$

Put the local unknowns and right-hand side term $r_4^{(j)}$ in vector forms of $\vec{q}^{(j)}=\left[q^{(j)}(\zeta_1),\ q^{(j)}(\zeta_2),\ \cdots,\ q^{(j)}(\zeta_{N_p})\ \right]^\top$ and $\vec{r_4}^{(j)}=\left[r_4^{(j)}(\zeta_1),\ r_4^{(j)}(\zeta_2),\ \cdots,\ r_4^{(j)}(\zeta_{N_p})\ \right]^\top$, respectively. Equation (3.49) can be written as

$$L\cdot\vec{q}^{(j)}+A^{(j)}\cdot\vec{q}^{(j)}+B^{(j)}\cdot\vec{q}^{(j)}+C^{(j)}\cdot\vec{q}^{(j-1)}+G^{(j)}\cdot\vec{q}^{(j-1)}$$
$$+E^{(j)}\cdot\vec{q}^{(j+1)}+F^{(j)}\cdot\vec{q}^{(j+1)}=M\cdot\vec{r_4}^{(j)} \tag{3.50}$$

or

$$(L+A^{(j)}+B^{(j)})\cdot\vec{q}^{(j)}+(C^{(j)}+G^{(j)})\cdot\vec{q}^{(j-1)}+(E^{(j)}+F^{(j)})\cdot\vec{q}^{(j+1)}=M\cdot\vec{r_4}^{(j)} \tag{3.51}$$

with these matrices defined as

$$L_{in}=\frac{2}{\Delta x}\int_{-1}^{1}\frac{dl_i}{d\zeta}\frac{dl_n}{d\zeta}d\zeta,\quad A_{in}^{(j)}=\sum_{s=1}^{Np} a^{(j)}(\zeta_s)\int_{-1}^{1}\frac{dl_i}{d\zeta}l_s l_n d\zeta, \tag{3.52}$$

$$B_{in}^{(j)}=\frac{\Delta x}{2}\sum_{s=1}^{Np} b^{(j)}(\zeta_s)\int_{-1}^{1} l_s l_i l_n d\zeta,\quad C_{in}^{(j)}=\sum_{s=1}^{Np} c^{(j)}(\zeta_s)\int_{-1}^{1}\frac{dl_i}{d\zeta}l_s l_n d\zeta, \tag{3.53}$$

$$G_{in}^{(j)}=\frac{\Delta x}{2}\sum_{s=1}^{Np} g^{(j)}(\zeta_s)\int_{-1}^{1} l_s l_i l_n d\zeta,\quad E_{in}^{(j)}=\sum_{s=1}^{Np} e^{(j)}(\zeta_s)\int_{-1}^{1}\frac{dl_i}{d\zeta}l_s l_n d\zeta \tag{3.54}$$

$$F_{in}^{(j)} = \frac{\Delta x}{2} \sum_{s=1}^{Np} f^{(j)}(\zeta_s) \int_{-1}^{1} l_s l_i l_n d\zeta \tag{3.55}$$

This system is closed by enforcing the Neumann boundary condition ($\frac{\partial q}{\partial \sigma} = 0$) at the bottom and Dirichlet boundary condition ($q = 0$) at the free surface. The overall degree of freedom of this system is N_g ($N_g = N_p \cdot NX \cdot NZ$). The global unknowns q and the right-hand side term r_4 can be assembled in vector forms as

$$\vec{q} = \left[q_1^{(1)}(\zeta_1), \cdots, q_1^{(1)}(\zeta_{N_p}), \cdots, q_{NX}^{(1)}(\zeta_1), \cdots, q_{NX}^{(1)}(\zeta_{N_p}), \cdots, q_{NX}^{(NZ)}(\zeta_1), \cdots, q_{NX}^{(NZ)}(\zeta_{N_p})\right]^\top, \tag{3.56}$$

$$\vec{r_4} = \left[r_4{}_1^{(1)}(\zeta_1), \cdots, r_4{}_1^{(1)}(\zeta_{N_p}), \cdots, r_4{}_{NX}^{(1)}(\zeta_1), \cdots, r_4{}_{NX}^{(1)}(\zeta_{N_p}), \cdots, r_4{}_{NX}^{(NZ)}(\zeta_1), \cdots, r_4{}_{NX}^{(NZ)}(\zeta_{N_p})\right]^\top \tag{3.57}$$

And the global discretized governing equation can be assembled as

$$\begin{pmatrix} L + A^{(1)} + B^{(1)} & C^{(1)} + G^{(1)} + E^{(1)} + F^{(1)} & 0 & \cdots & 0 \\ C^{(2)} + G^{(2)} & L + A^{(2)} + B^{(2)} & E^{(2)} + F^{(2)} & & \vdots \\ 0 & \ddots & \ddots & \ddots & 0 \\ \vdots & & C^{(NZ-1)} + G^{(NZ-1)} & L + A^{(NZ-1)} + B^{(NZ-1)} & E^{(NZ-1)} + F^{(NZ-1)} \\ 0 & \cdots & 0 & C^{(NZ)} + G^{(NZ)} & L + A^{(NZ)} + B^{(NZ)} \end{pmatrix} \cdot \vec{q}$$

$$= \begin{pmatrix} M & & 0 \\ & \ddots & \\ 0 & & M \end{pmatrix} \cdot \vec{r_4} \tag{3.58}$$

The resulting linear system is solved using the BiCGSTAB method with the ILU (incomplete LU) preconditioner.

3.3.5 Overall algorithm

The computation within one time step is comprised of three stages, and each stage is comprised of hydrostatic and non-hydrostatic phase. The sequence of the computation in one time step can be summarized as follows:

1. Start the sequence from the previous time step with unknowns $D^n, (Du)^n, (Dw)^n, q^n$;

2. Solve Equations (3.29), (3.30), and (3.31) to obtain $D^{(1)},\ (Du)^*$ and $(Dw)^*$;

3. Solve Equation (3.58) to obtain the non-hydrostatic pressure q;

4. Update velocities with Equations (3.32) and (3.33) for $(Du)^{(1)}$ and $(Dw)^{(1)}$. So far, we have estimates for unknowns at stage I;

5. Repeat steps 1-4 and obtain $D^{(2)},\ (Du)^{(2)}$ and $(Dw)^{(2)}$;

6. Update the final estimates of unknowns at stage II using Equation (3.36);

7. Repeat steps 1-4 and obtain $D^{(3)},\ (Du)^{(3)}$ and $(Dw)^{(3)}$;

8. Update the final estimates of unknowns at stage III using Equation (3.37);

9. $(D^{n+1}, (Du)^{n+1}, (Dw)^{n+1}) = (D^{(3)}, (Du)^{(3)}, (Dw)^{(3)})$.

3.4 Model verifications

We firstly demonstrate the numerical convergence rate of the Poisson solver by considering a manufactured partial differential problem. To study the accuracy and capability of this model in resolving linear dispersion properties and nonlinear effect, linear and nonlinear standing wave test cases are conducted. The dispersion accuracy of the Euler model is examined through the analytical dispersion relationship (Zhu et al. 2014). In linear and nonlinear standing waves tests, we set $N_p = 3$ and $NX = 10$. To examine the numerical dispersion relationship, finer horizontal resolutions are required, and we set $N_p = 5$ and $NX = 10$. The time step Δt is adaptive, determined by

$$\Delta t = \text{CFL} \cdot \min\left(\min_{k,\,j}\left(\min_{i}\Delta x\right)\Big/\left(|u_{k,j}| + \sqrt{gh}\right),\ \min_{k,\,j}\Delta\sigma_j D_k\big/|w_{k,j}|\right) \tag{3.59}$$

where CFL is the Courant-Friedrichs-Lewy numer, taken to be 0.1. "k" is element index, "i" is local quadrature point index, and "j" is layer index. g is fixed to 9.806 m/s^2.

3.4.1 Convergence tests of Poisson solver

The convergence rate of the Poisson solver is tested using a manufactured solution. Let

$$r_1(x,\ \sigma) = r_2(x,\ \sigma) = r_3(x,\ \sigma) = \cos(x)$$

$$r_4(x,\ \sigma) = -\cos(x)\Big[\frac{\cosh(\sigma+1)}{\cosh(1)} - 1\Big] - r_1(x)\sin(x)\frac{\sinh\sigma + 1}{\cosh(1)} + r_2(x)\cos(x)\frac{\cosh(\sigma+1)}{\cosh(1)} + r_3(x)\cos(x)\frac{\sinh(\sigma+1)}{\cosh(1)}$$

in the Poisson equation (3.38), and the manufactured solution q_{exact} becomes

$$q_{exact}(x,\ \sigma) = \cos(x)\Big[\frac{\cosh(\sigma+1)}{\cosh(1)} - 1\Big].$$

Firstly, the convergence rate of the vertical discretization is studied by fixing $NX = 50$ and $Np = 2$, and varying NZ. The errors are measured in the L^1-norm ($\| q - q_{exact} \|_{L_1} = \int | q - q_{exact} | dxd\sigma$). Our analysis predicts second-order convergence as shown in Figure 3.2.

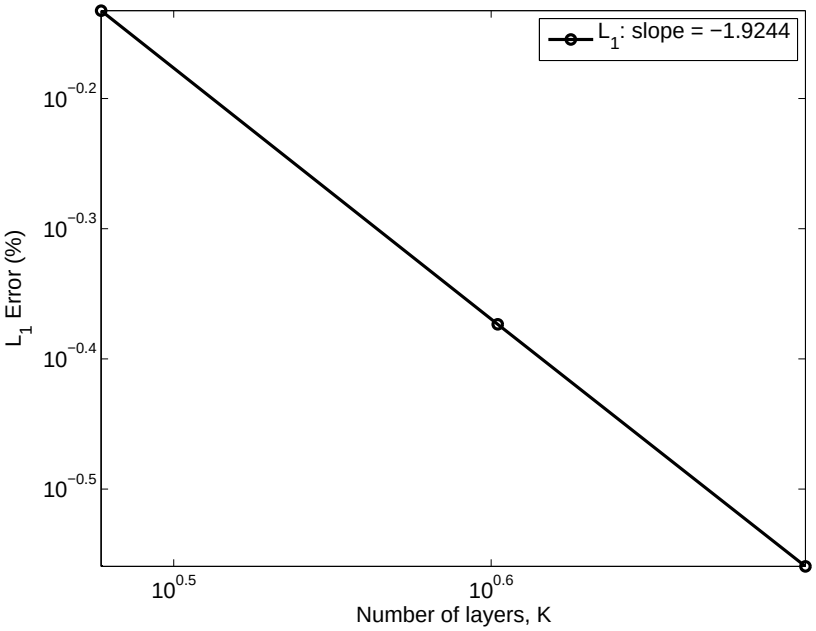

FIGURE 3.2. Convergence rate of the Poisson solver of the vertical disretization.

To minimize the computational cost, we consider a 1D Poisson equation to study the h-convergence of the Poisson solver, because for cases of $Np > 2$ and with limited vertical layers (around 10 layers), the computational errors introduced by the vertical discretization could be overwhelming compared with the ones introduced by the horizontal discretization. The 1D Poisson equation is

$$\frac{\partial^2 q}{\partial x^2} + r_1(x)\frac{\partial q}{\partial x} + r_2(x)q = r_4(x,\ \sigma) \tag{3.60}$$

with $r_1(x,\ \sigma) = r_2(x,\ \sigma) = \cos(x)$ and $r_4(x,\ \sigma) = -\cos(x) - r_1(x)\sin(x) + r_2(x)\cos(x)$. The manufactured solution is $q_{exact}(x,\ \sigma) = \cos(x)$. In Figure 3.3 we observe that the solutions converge with the order of $O(h^{Np+1})$.

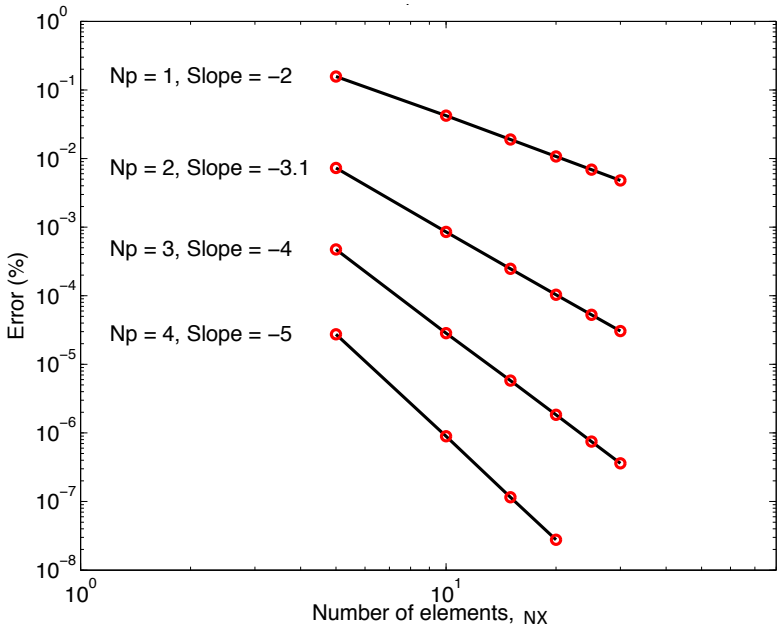

FIGURE 3.3. h-convergence of the Poisson solver with Np = 1, 2, 3 and 4

3.4.2 Linear standing waves in a closed basin

We first consider a standing wave with an amplitude $a_0 = 0.1$ m in a 10 m long closed basin with 10 m deep water. The model is initially set up as

$$D = h + a_0 \cos\left(\frac{\pi x}{10}\right), \quad 0 \le x \le 20 \tag{3.61}$$

The computational domain is divided to 100 grids with uniform spacing of 0.1 m in the horizontal direction. The wave with $kh = 2\pi$ is highly dispersive, but only two uniform layers is needed with relative dispersion error of 0.25% owing to the Keller-box scheme. The numerical solution are compared with the analytical solution from the linear wave theory

$$D = h + a_0 \cos\left(\frac{\pi x}{10}\right) \cos(\omega t), \quad 0 \leq x \leq 20 \tag{3.62}$$

where ω is the wave frequency determined by the dispersion relationship. Figure 3.4 shows a comparison of the numerical and exact surface elevations at $x = 10$ m. The surface elevation was normalized by the wave amplitude a_0 and time was normalized by the wave period T. The computed surface elevations agree well with the exact solution.

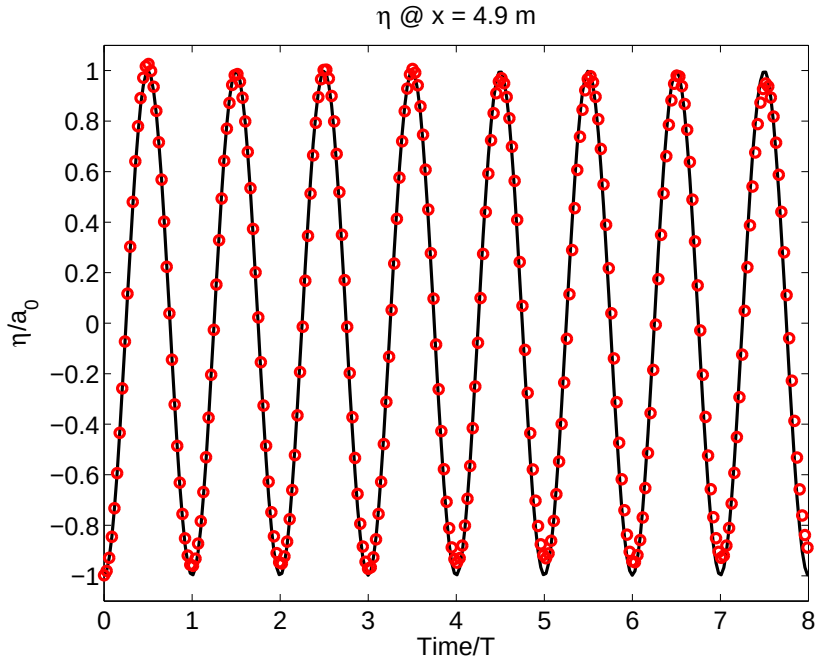

FIGURE 3.4. A comparison between the numerical (dash line) and exact (solid line) surface elevations for standing waves with $kh = 2\pi$ using two uniform layers.

3.4.3 Nonlinear standing waves in a closed basin

Nonlinear standing waves with an amplitude a_0 sloshing in a 20 m long closed basin were simulated to examine the performance of this Euler model in simulating nonlinear dispersive

waves. Exact solutions, based on a fifth-order Stokes theory (Sobey 2009), were used to specify the initial conditions and verify the model results. The analytical solutions of surface elevation and velocities can be found in Appendix C. The non-linear dispersion relationship derived by Sobey (2009) reads

$$(gk)^{1/2} \sum_{i=1}^{5} (ka_0)^{(i-1)} D_i = 2\pi/T \tag{3.63}$$

where D_i are dimensionless coefficients given in Appendix B. The phase speed, affected by the wave nonlinearity, becomes a function of kh and ka_0. Two layers with the suggested optimal layer distribution from Chapter 2 are employed to predict waves with four wave steepnesses, ranging from linear ($ka_0 = 0.000628$), weakly nonlinear ($ka_0 = 0.157$), strongly nonlinear ($ka_0 = 0.314$) to the wave breaking limit ($ka_0 = 0.44$). Figure 3.5 shows the comparison of the modeled surface elevation and fifth-order Stokes solution (Sobey 2009) under four types of wave conditions corresponding to $kh = 9.0478$. It is seen that the numerical model with the optimized layer thickness captures the wave nonlinearity quite well in comparison with the Stokes solutions of nonlinear stranding waves.

3.4.4 Numerical dispersion relationship

Chapter 2 presents the analytical dispersion relationship of a two-/three-layer numerical model using the Keller-box scheme. Figure 3.6 - 3.7 shows the comparison of the relative phase errors obtained theoretically and numerically using two layers with equal and optimal distributions with a 1% tolerance dispersion error. The wavelength L is fixed as 10 m, and the water depth h varies. The wave amplitude a_0 is set as 10^{-4} m to eliminate nonlinear effects. The numerical results exhibit excellent agreement with the theoretical dispersion relationship.

3.5 Conclusions

An efficient and accurate approach is developed to solve Euler equations for fully dispersive and highly nonlinear water waves. Discontinuous Galerkin, finite difference, and spectral element formulations are used for horizontal discretization, vertical discretization, and the Pois-

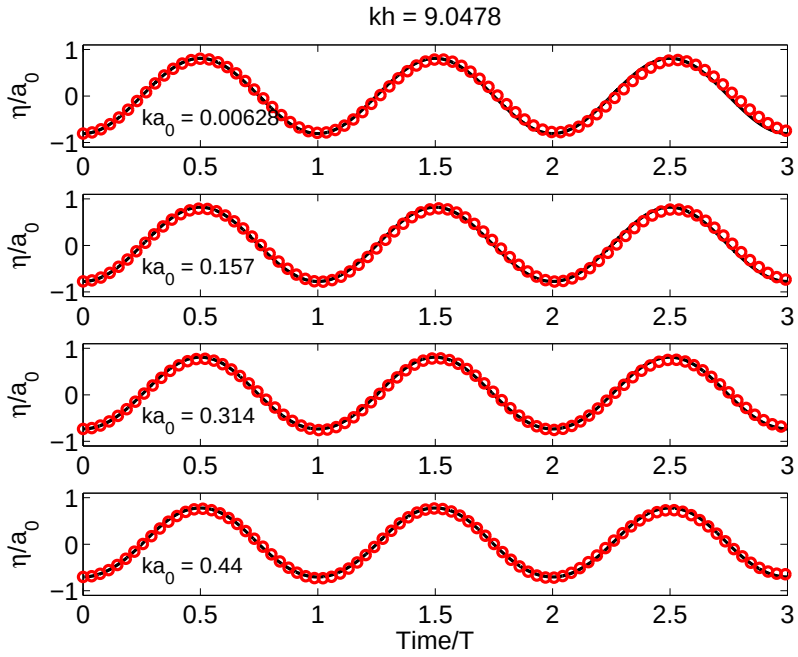

FIGURE 3.5. Comparison of numerical (circles) and fifth-order Stokes (solid line) solutions of surface elevations for linear waves ($ka_0 = 0.00628$), weakly nonlinear waves ($ka_0 = 0.157$), strongly nonlinear waves ($ka_0 = 0.314$), and extremely nonlinear waves ($ka_0 = 0.440$) with $kh = 9.0478$.

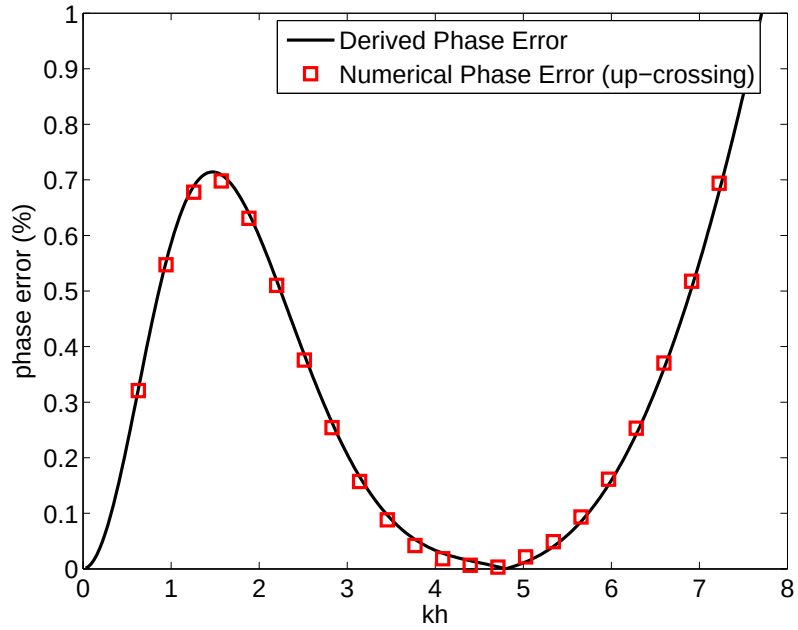

FIGURE 3.6. Comparison of the relative phase errors obtained theoretically (solid lines) and numerically (circles) using two equally distributed bounded by a 1% tolerance dispersion error

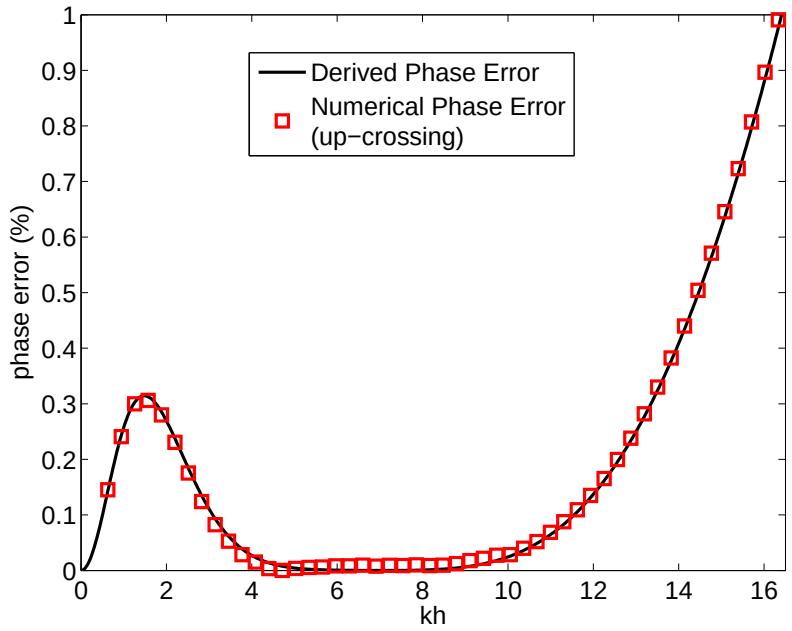

FIGURE 3.7. Comparison of the relative phase errors obtained theoretically (solid lines) and numerically (circles) using three equally distributed bounded by a 1% tolerance dispersion error

son equation, respectively. The Keller-box scheme is adopted for its capability of resolving frequency dispersion accurately with low vertical resolution (two or three layers). A three-stage optimal Strong Stability-Preserving Runge-Kutta (SSP-RK) scheme is employed for time integration. The local elements are connected together by numerical fluxes, evaluated using the Lax-Friedrichs and HLL Riemann solvers. Besides the well-recognized advantages of DG methods, this hybrid DG-SE-FD approach significantly reduces the overall degree of freedom compared with a complete DG approach. The methodology is proved to produce accurate results for fully dispersive and highly nonlinear wave problem. The numerical dispersion relationship agrees well with the theoretical dispersion relationship.

CHAPTER 4 NUMERICAL MODELING OF SURFACE WAVES OVER SUBMERGED FLEXIBLE VEGETATION [1]

4.1 Introduction

Coastal wetlands have been recognized as a buffer zone protecting the inner land and a natural erosion barrier stabilizing the shoreline. By attenuating incoming waves and trapping sediment in vegetated areas, the coastal vegetation can provide substantial protection from erosion. Considerable effort has been devoted to field studies (e.g. Bradley and Houser 2009; Jadhav et al. 2013; Jadhav and Chen 2013), laboratory experiments (e.g. Stratigaki et al. 2011; Koftis et al. 2013; Ozeren et al. 2013; Anderson and Smith 2014) and numerical simulations (e.g. Li and Yan 2007; Dijkstra and Uittenbogaard 2010; Suzuki et al. 2011; Wu et al. 2012; Tang et al. 2013; Blackmar et al. 2014; Zhan et al. 2014) aimed at quantifying vegetation-induced wave attenuation, and understanding wave-vegetation interactions.

Most natural vegetation is deformable, which reduces the flow resistance. In contrast to the large number of models neglecting vegetation motions, only a small number of models consider the vegetation swaying effect. A simple but less robust way is to reduce the drag coefficient to achieve the equivalent wave attenuation (Kobayashi et al. 1993). The drag coefficient due to swaying is not only a function of the plant rigidity but also influenced by the degree of submergence and hydrodynamic conditions. The calibrated drag coefficients are on the order of 0.1 in Kobayashi et al. (1993). However, application of this method is limited because of the uncertainty of the drag coefficient. Zhao and Chen (2013) extended and unified resistance formulations for rigid and deformable plants under both emergent and submergent conditions. A resistance formulation together with an empirical relationship between the deflected vegetation height and the flow drag exerted on vegetation elements were utilized to iteratively determine

[1] This chapter has appeared in "Journal of Engineering Mechanics". Zhu, L. and Chen, Q. (2015). "Numerical Modeling of Surface Waves over Submerged Flexible Vegetation." J. Eng. Mech., A4015001. doi:10.1061/(ASCE)EM.1943-7889.0000913. It is reprinted by permission of ASCE.

the changing drag force and vegetation deformation. Li and Xie (2011) investigated the hydrodynamics of submerged flexible vegetation with or without foliage using a 3D non-hydrostatic model with the σ-coordinate for the treatment of the free surface. The effective stem height was determined by an empirical formulation obtained by solving a bending equation in a sufficient large number of cases with different conditions. Only the effective height of the deformed vegetation was included to account for the reduction of drag due to plant deformation under combined wave and current conditions.

A different methodology is to solve the vegetation motion from a force balance equation and incorporate relative velocities into the vegetation-induced resistance (Asano et al. 1992, Dubi and Torum 1996; Mendez et al. 1999; Ikeda et al. 2001; Maza et al. 2013). The balance of forces for the vegetation motion includes buoyancy, damping, stiffness of the vegetation, and gravity as restoring forces, and drag and inertia as driving forces (Asano et al. 1992; Ikeda et al. 2001). Mullarney et al. (2010) presented a theoretical relationship between the movement of single-stem vegetation and water particle based on the cantilever beam theory, balancing stiffness with drag on stem elements. The model assumed negligible inertia and buoyancy, small deformations, and thin near-vertical stems. A dimensionless parameter S was proposed to measure vegetation stiffness. This parameter incorporates material and geometric properties of the vegetation, as well as wave period and velocity. When S approaches 0, stems move with the surrounding fluid particles except in a thin near-bed elastic boundary layer, whereas when S approaches infinity, stem deflections approach zero but lead the displacements of surrounding fluid particles by 90°. Mullarney et al. (2010) also concluded that the simulated dissipation by the flexible stems was about 30% of the dissipation caused by equivalent rigid stems.

Maza et al. (2013) presented a two-dimensional model on the vertical plane based on the Reynolds Average Navier-Stokes (RANS) equations for modeling wave attenuation due to submergent flexible vegetation. Instead of solving the full force balance equation for the deforma-

tion of each stem, their model solves the displacement at the top of each stem and assumes a linear variation of vegetation deflection along the stem as proposed by Dupont et al. (2010). The linear assumption of stem deformation is limited to small deflections and applicable only to intermediate and completely rigid vegetation. Ikeda et al. (2001) included the wavy motion of deformable plants into a two-dimensional large eddy simulation to identify the effect of honami on turbulent flow structure. The model utilized a plant grid to track the displacement of each stem. An exponential distribution of drag force was assumed for computing the stem displacement. The relative velocities were utilized to compute the vegetation-induced resistance in both models.

The motivation of this paper is to develop a robust vegetation model that solves the complete force balance equation for plant deformation in an efficient way. This model can be coupled with any phase-resolving wave model, such as Boussinesq-type models (e.g. Madsen et al. 1992; Chen et al. 2000; Lynett and Liu 2004; Shi et al. 2012), non-hydrostatic models (e.g. Wu et al. 2010; Zijlema et al. 2011; Ma et al. 2012), and RANS-VOF models (e.g. Lin and Liu 1998). At each computation step of the wave model, the flow information such as velocities and surface elevation will be fed into the vegetation model, which computes the effective vegetation height and vegetation-induced resistance in return. These outcomes will be fed back to the wave model for the next step of computation. To reduce the computational cost, a high order finite element method (FEM) is utilized for the proposed vegetation model. In this paper, the proposed vegetation model is coupled with an existing non-hydrostatic model for testing and demonstration purpose. The results of the vegetation model exhibit a 4th-order convergence rate. Rigorous verifications are carried out to assure the accuracy of the proposed model.

4.2 Model Description

4.2.1 Governing equations for wave propagation and numerical model

In the current study, the Non-Hydrostatic WAVE model (NHWAVE), excluding turbulence and diffusion, is adapted to simulate wave propagation over a patch of submerged deformable vegetation. For completeness, the continuity equation and momentum equations with the vegetation-induced resistance are listed as follows:

$$\frac{\partial u}{\partial x^*} + \frac{\partial w}{\partial z^*} = 0 \tag{4.1}$$

$$\frac{\partial u}{\partial t^*} + u\frac{\partial u}{\partial x^*} + w\frac{\partial u}{\partial z^*} + \frac{\partial p}{\partial x^*} + F_v = 0 \tag{4.2}$$

$$\frac{\partial w}{\partial t^*} + u\frac{\partial w}{\partial x^*} + w\frac{\partial w}{\partial z^*} + \frac{\partial p}{\partial z^*} = 0 \tag{4.3}$$

where, (x^*, z^*) is the Cartesian coordinate, u and w are the velocity components in the x^*-, z^*-direction respectively, and p is the total pressure. F_v, the vegetation-induced forces, can be expressed as

$$F_v = \frac{1}{2}C_D b_v N|u - u_v|(u - u_v) + VN\big[C_M\dot{u} - (C_M - 1)\dot{u}_v\big] \tag{4.4}$$

in which C_D, b_v, N, u, u_v, V and C_M are drag coefficient, area per unit height of each vegetation stand normal to the horizontal velocity, number of vegetation stands per unit horizontal area, fluid velocity, vegetation motion, volume per unit height of each vegetation stand, and inertia coefficient, respectively. The first term of F_v is drag and the second term is inertia.

The wave model is based on the σ-coordinate $(x,\ \sigma)$, which can accurately capture the moving free surface and uneven bottom geometry. The mapping formulation is given by

$$t = t^*,\ \ x = x^*,\ \ \sigma = \frac{z^* + h}{D} \tag{4.5}$$

where $D(x,t) = h(x) + \eta(x,t)$, in which $h(x)$ is the still water depth, $\eta(x,t)$ is the surface elevation. The transformed governing equations become

$$\frac{\partial D}{\partial t} + \frac{\partial Du}{\partial x} + \frac{\partial D\omega}{\partial \sigma} = 0 \tag{4.6}$$

$$\frac{\partial Du}{\partial t} + \frac{\partial Du^2}{\partial x} + \frac{1}{2}g\frac{\partial D^2}{\partial x} + \frac{\partial Du\omega}{\partial \sigma} + D\left(\frac{\partial q}{\partial x} + \frac{\partial q}{\partial \sigma}\frac{\partial \sigma}{\partial x^*}\right) + DF_v = 0 \tag{4.7}$$

$$\frac{\partial Dw}{\partial t} + \frac{\partial Duw}{\partial x} + \frac{\partial D\omega w}{\partial \sigma} + \frac{\partial q}{\partial \sigma} = 0 \tag{4.8}$$

where $\omega(x, \sigma, t)$ is the vertical velocity in the σ-coordinate, equaling zero at the bottom $(\sigma = 0)$ and free surface $(\sigma = 1)$. F_v is the vegetation-induced forces and q is the non-hydrostatic pressure. The free surface is governed by the integrated continuity equation

$$\frac{\partial D}{\partial t} + \frac{\partial}{\partial x}\left(D\int_0^1 ud\sigma\right) = 0 \tag{4.9}$$

The wave model employs a combined finite volume and finite difference method with a second order nonlinear Strong Stability-Preserving (SSP) Runge-Kutta scheme (Gottlieb et al. 2001). All variables are defined at the cell center and the numerical fluxes at the cell interfaces are approximated using the HLL Riemann solver (Harten et al. 1983). To avoid spurious oscillations introduced by the large nonlinearity in the simulations of large amplitude waves, especially for short waves, a Total Variation Diminishing (TVD) method is used by applying the minmod pre-processing slope limiter (Toro 2001). The details of numerical schemes, discretization and the algorithm can be found in Ma et al. (2012) and Shi et al. (2012).

4.2.2 Governing equation for vegetation motion and vegetation model

The balance of forces for the vegetation motion includes buoyancy, damping, stiffness of the vegetation, and gravity as restoring forces, and drag and inertia as driving forces. At $t = t^{n+1}$, the governing equation for vegetation motion is given by (Ikeda et al. 2001)

$$\begin{aligned}\rho_v V\ddot{\xi}^{n+1} + C_1\dot{\xi}^{n+1} + EI{\xi_z^{(4)}}^{n+1} &= \frac{1}{2}\rho_f C_D b_v\left|\dot{W}^{n+1} - \dot{\xi}^{n+1}\right|\left(\dot{W}^{n+1} - \dot{\xi}^{n+1}\right) \\ &+ \rho_f(C_M - 1)V(\ddot{W}^{n+1} - \ddot{\xi}^{n+1}) \\ &+ \rho_f V\ddot{W}^{n+1} - (\rho_f - \rho_v)gV{\xi_z^{(1)}}^{n+1} \end{aligned} \tag{4.10}$$

with

$$\xi(0,\, t^{n+1}) = \xi_z^{(1)}(0,\, t^{n+1}) = 0 \quad \text{and} \quad \xi_z^{(2)}(l_0,\, t^{n+1}) = \xi_z^{(3)}(l_0,\, t^{n+1}) = 0 \tag{4.11}$$

where ξ is the horizontal displacement of the vegetation stand, W is the water particle movement, ρ_v is the vegetation density, ρ_f is the fluid density, E is the Young's modulus, I is the second moment of stem area, C_1 is the damping coefficient and l_0 is the vegetation length. The overhead dot denotes time derivative, and the subscript z denotes the differentiation along the vegetation stem and the superscript denotes the order of the derivative in z. The superscript n denotes the time step. Viscous shear stresses acting on the interface and the bottom are neglected because the drag resistance of the vegetation is predominant for most practical applications. This vegetation motion model has the following assumptions: (i) plant motion remains inside the same fluid grid cell, and (ii) there is no interaction between neighboring plants.

High-order finite element methods (FEM) have been utilized in structural and fluid dynamic analysis. A high-order FEM (Hughes 1987), and the semi-implicit time scheme, is employed to solve the deformation equation for each vegetation stem. The vegetation stem l_0 is divided into N elements, intercepted with $N+1$ nodes: $\{z_i \mid 0 = z_0 < z_1 < z_2 < \ldots < z_N = l_0\}$. The length of each element is $h_e = l_0/N$. At element $[z_k,\ z_{k+1}]$, Hermite cubic shape functions $N_i(z), i = 1, \ldots, 4$, defined below are introduced as weight functions for achieving fourth-order accuracy,

$$\begin{aligned} N_1 &= 1 - 3\Big(\frac{z}{h_e}\Big)^2 + 2\Big(\frac{z}{h_e}\Big)^3, \qquad N_2 = z\Big(1 - \tfrac{z}{h_e}\Big)^2, \\ N_3 &= 3\Big(\frac{z}{h_e}\Big)^2 - 2\Big(\frac{z}{h_e}\Big)^3, \quad N_4 = z\Big[\Big(\tfrac{z}{h_e}\Big)^2 - \tfrac{z}{h_e}\Big]. \end{aligned} \tag{4.12}$$

and semi-implicit method is employed to discretize the quadratic term in the drag force as

$$\left|\dot{W}^{n+1}-\dot{\xi}^{n+1}\right|\left(\dot{W}^{n+1}-\dot{\xi}^{n+1}\right)\simeq\left|\dot{W}^{n}-\dot{\xi}^{n}\right|\left(\dot{W}^{n+1}-\dot{\xi}^{n+1}\right). \tag{4.13}$$

For simplicity, we remove the superscript "$n+1$" in Equation (4.10) and rewrite the governing equation as

$$f_1\ddot{\xi}+f_2\dot{\xi}+f_3\xi_z^{(4)}+f_4\xi_z^{(1)}=f_5\dot{W}+f_6\ddot{W} \tag{4.14}$$

where

$$\begin{aligned}
f_1 &= \rho_v V+\rho_f(C_M-1)V && (4.15)\\
f_2 &= C_1+\frac{1}{2}\rho_f C_D b_v\left|\dot{W}-\dot{\xi}\right|^n && (4.16)\\
f_3 &= EI && (4.17)\\
f_4 &= (\rho_f-\rho_v)gV && (4.18)\\
f_5 &= \frac{1}{2}\rho_f C_D b_v\left|\dot{W}-\dot{\xi}\right|^n && (4.19)\\
f_6 &= \rho_f V C_M && (4.20)
\end{aligned}$$

The approximate solution to Equation (4.14) can be expanded into

$$\xi(z,t)=\sum_{i=1}^{N}\xi_i(t)r_i(z) \tag{4.21}$$

where $\xi_i(t)=\xi(z_i,\ t)$ is the nodal value at node z_i and $r_i(z)$ is the weight function. Multiply Equation (4.14) with $r_j(z), j=1,\ldots,4$, integrate over $[z_k,\ z_{k+1}]$ and apply the chain rule in reverse. The weak form of the governing equation becomes

$$\begin{aligned}
&f_1\textstyle\int_{z_k}^{z_{k+1}}\ddot{\xi}r_j(z)dz+f_2\int_{z_k}^{z_{k+1}}\dot{\xi}r_j(z)dz+f_3\int_{z_k}^{z_{k+1}}\xi_z^{(2)}r_j^{(2)}(z)dz+f_4\int_{z_k}^{z_{k+1}}\xi_z^{(1)}r_j(z)dz\\
&\qquad=f_5\textstyle\int_{z_k}^{z_{k+1}}\dot{W}r_j(z)dz+f_6\int_{z_k}^{z_{k+1}}\ddot{W}r_j(z)dz
\end{aligned} \tag{4.22}$$

Substituting Equation (4.21) into Equation (4.22), we get

$$\begin{aligned}
&f_1\textstyle\sum_i\ddot{X}_i\int_{z_k}^{z_{k+1}}r_i(z)r_j(z)dz+f_2\sum_i\dot{X}_i\int_{z_k}^{z_{k+1}}r_i(z)r_j(z)dz+f_3\sum_i X_i\int_{z_k}^{z_{k+1}}r_i^{(2)}(z)r_j^{(2)}(z)dz+\\
&\qquad f_4\textstyle\sum_i X_i\int_{z_k}^{z_{k+1}}r_i^{(1)}(z)r_j(z)dz=f_5\int_{z_k}^{z_{k+1}}\dot{W}r_j(z)dz+f_6\int_{z_k}^{z_{k+1}}\ddot{W}r_j(z)dz
\end{aligned} \tag{4.23}$$

Let weight functions to be the same as Hermite shape functions. Exchanging the sequence of the integration and summation in Equation (4.23) and performing mapping to element $[z_k,\ z_{k+1}]$ as $s = (z - z_k)/h_e$, we obtain the local equation in the matrix form

$$f_1\mathbf{J}^k\ddot{X}^k + f_2\mathbf{J}^k\dot{X}^k + f_3\mathbf{K}^kX^k + f_4\mathbf{M}^kX^k = f_5B^k + f_6C^k \tag{4.24}$$

where $\mathbf{K}^k$, $\mathbf{J}^k$, $\mathbf{M}^k$ and B^k, C^k, defined below are local matrices and vectors over element $[z_k,\ z_{k+1}]$ with the dimensions of 4×4 and 4×1, and $X^k = [\xi_k,\ , \frac{d\xi_k}{dz},\ , \xi_{k+1},\ \frac{d\xi_{k+1}}{dz}]$ is the local unknown vector.

$$K_{ij} = \frac{1}{h_e^4}\int_0^1 N_i^{(2)}(s)N_j^{(2)}(s)ds \tag{4.25}$$

$$J_{ij} = \int_0^1 N_i(s)N_j(s)ds \tag{4.26}$$

$$M_{ij} = \frac{1}{h_e}\int_0^1 N_i^{(1)}(s)N_j(s)ds \tag{4.27}$$

$$B_j = \int_0^1 \dot{W}N_j(s)ds \tag{4.28}$$

$$C_j = \int_0^1 \ddot{W}N_j(s)ds \tag{4.29}$$

Assemble the local matrices $\mathbf{K}^k$, $\mathbf{J}^k$, $\mathbf{M}^k$ and local vectors B^k, C^k into global ones, $\mathbf{K}$, $\mathbf{J}$, $\mathbf{M}$ and B, C. The global matrix form of the governing equation can be expressed as

$$f_1\mathbf{J}\ddot{X} + f_2\mathbf{J}\dot{X} + f_3\mathbf{K}X + f_4\mathbf{M}X = f_5B + f_6C \tag{4.30}$$

The temporal discretization of Equation (4.30) utilizes an implicit time stepping scheme as follows

$$f_1\mathbf{J}\frac{X^{n+1} - 2X^n + X^{n-1}}{\Delta t^2} + f_2\mathbf{J}\frac{X^{n+1} - X^{n-1}}{2\Delta t} + f_3\mathbf{K}X^{n+1} + f_4\mathbf{M}X^{n+1} = f_5B + f_6C \tag{4.31}$$

Rearranging Equation (4.31) yields

$$\Big[\Big(\frac{f_1}{\Delta t^2} + \frac{f_2}{2\Delta t}\Big)\mathbf{J} + f_3\mathbf{K} + f_4\mathbf{M}\Big]X^{n+1} = f_5B + f_6C - \frac{f_1}{\Delta t^2}\mathbf{J}(X^{n-1} - 2X^n) + \frac{f_2}{2\Delta t}\mathbf{J}X^{n-1} \tag{4.32}$$

As the deflection ξ as well as the gradient of the deflection (ξ_z) are fixed to be zero at the bottom, we enforce the elements of the first two columns and rows of $\left[\left(\frac{f_1}{\Delta t^2}+\frac{f_2}{2\Delta t}\right)\mathbf{J}+f_3\mathbf{K}+f_4\mathbf{M}\right]$ to be zero, and its upper left 2×2 submatrix to be an identity matrix. Also, we enforce the first two elements of the vector on the right hand side of Equation (4.32) to be zero.

A procedure is provided in Appendix to calculate the vegetation deflection and swaying motion. To couple the vegetation model and wave model, we first solve the vegetation motion equation using fluid velocities from previous time steps, and calculate the drag and inertia forces using the relative velocity, u_{rel} (= $\dot{W}-\dot{\xi}$). The forces will be substitute back to the horizontal momentum equation for the next time step of computation. This vegetation model can be coupled with any phase-resolving wave model, as illustrated in Figure 4.1.

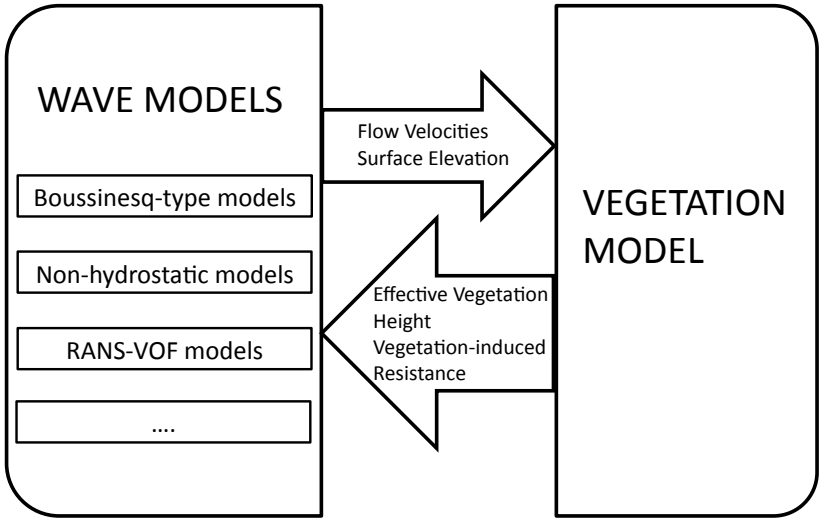

FIGURE 4.1. A sketch of wave and vegetation model coupling

The FEM with cubic weight functions gives fourth-order convergence rate while the central-differencing finite-difference method (FDM) gives second-order. Compared to FDM, the high-order FEM permits the use of a small number of elements to achieve the desired accuracy, which will reduce computational costs for large-scale vegetation computation. Figure 4.2 shows the

numerical convergence rates of our model using both FEM and FDM. This demonstrates the consistency and correctness of the numerical solution to the vegetation motion equation.

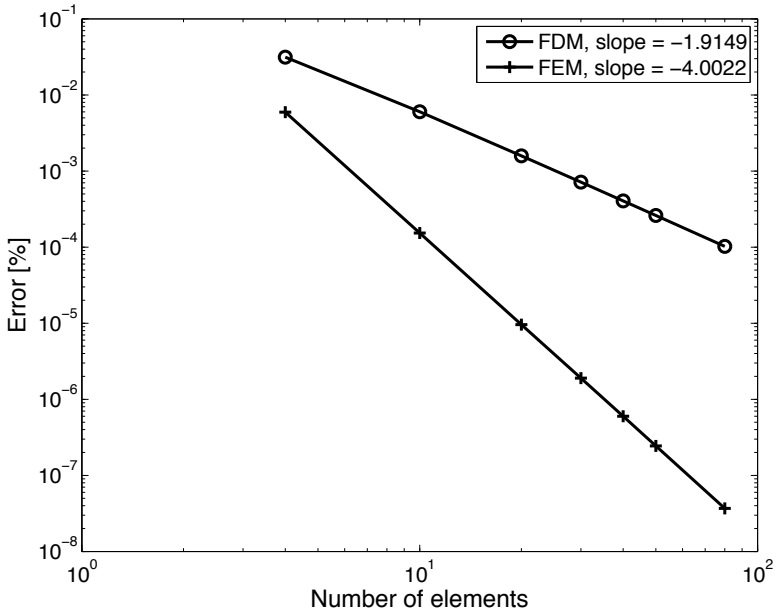

FIGURE 4.2. Numerical convergence rates of FEM and FDM for solving vegetation motion

4.3 Model Verification

4.3.1 Deflection of single-stem swaying vegetation

The numerical results of single-stem vegetation deflection obtained from our fully-coupled wave and vegetation model are compared with analytical solutions presented in Mullarney et al. (2010). In that work, a theoretical relationship between the movements of water particle and single-stem vegetation was derived based on the Euler-Bernoulli equation and compared with field observation. Buoyancy, inertia, damping and gravity were neglected and an assumption of small vegetation deformation was made. The drag force is linearized as

$$F_v = \frac{1}{2}\rho_f C_D r_0 |U^*| \left(\dot{W} - \dot{\xi}\right) \tag{4.33}$$

where ρ_f is water density, C_D is drag coefficient, r_0 is stem radius, $|U^*|$ is characteristic velocity magnitude defined as $\sqrt{8/\pi}$ times the depth-averaged RMS relative velocity, W is water particle movement, and ξ is vegetation deformation.

The wave condition and vegetation characteristics were combined into a single dimensionless parameter S

$$S = \frac{E r_0^3 T_0^2}{\rho_f C_D l_0^4 W_0} \tag{4.34}$$

where E is Young's modulus, T_0 is wave period, l_0 is stem length, and W_0 is characteristic water particle displacement, defined as the $2W_0 = |U^*|T_0$. The vegetation motion leads water motion, but such a phase difference decreases (from 90° to 0°) as S decreases. The magnitude of vegetation deformation decreases as S increases.

The computational domain has a constant water depth of 1.5 m. Regular waves with a height of 4 cm and a period of 2.95 s are generated at the inflow boundary. A single-stem plant is placed at one wavelength away from the inflow boundary. The length, radius of the stem is l_0 = 0.85 m, r_0 = 16 mm, respectively. The drag coefficient is considered to be constant: C_D = 2.0. The Young's modulus value, E, is the only free parameter for tuning S. A total of 8 simulations are carried out with different S, ranging from 0.0042 to 42. The numerical results of vegetation deformation (ξ) and water particle movement (W) are expanded as Fourier modes in time t and normal mode in the vertical coordinate z. The first few modes dominate the free vibration of vegetation stem. In this test case, we only compare the coefficients $\langle \xi \rangle$ and $\langle W \rangle$ of the first mode with the analytical solution for model verification.

Depending on the stiffness, vegetation stems may move like a cantilever or a whip driven by waves (Paul et al. 2012). Figure 4.3 illustrates the computed bending and swaying of extremely flexible vegetation ($S = 0.0042$), moderately flexible vegetation ($S = 0.42$), and stiff vegetation ($S = 42$), respectively. The deflection of stiff vegetation (e.g. salt-marshes) appears to follow a linear variation along the stem (Asano et al. 1992; Mendez et al. 1999; Maza et al.

2013); while the deflection of moderately flexible vegetation (e.g. sedge Schoenoplectus americanus) exhibits a non-linear variation under exponential forces (Ikeda et al. 2001). However for flexible vegetation (e.g. seagrasses) the blades show a whip-like motion, which can only be computed by solving Equation (4.10). Figure 4.4 shows the time series of the computed

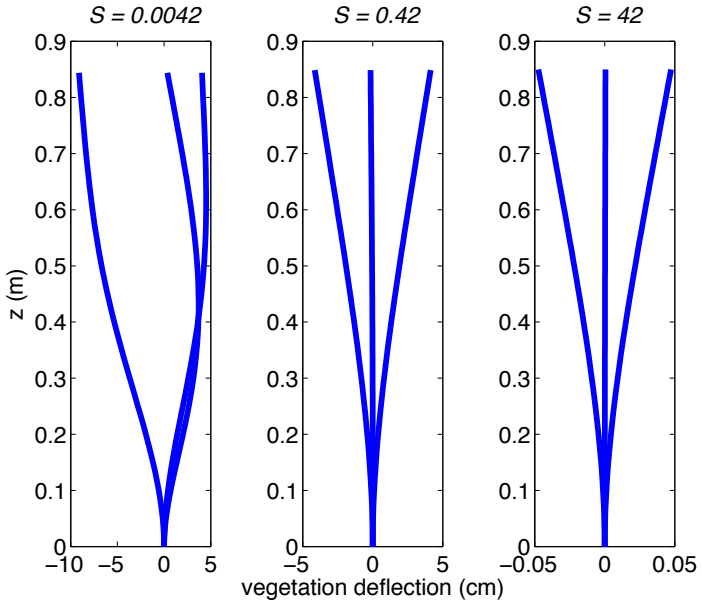

FIGURE 4.3. The computed bending and swaying of extremely flexible vegetation ($S = 0.0042$), moderately flexible vegetation ($S = 0.42$), and stiff vegetation ($S = 42$), respectively

surface elevation and deflection at the top end of the vegetation stem for aforementioned three vegetation cases. Because of the phase difference between the surface elevation and the water particle excursion ($90°$) as well as the phase differences between the vegetation deflection and water particle motion ($0° \sim 90°$), the maximum vegetation deflection and wave crests never synchronize for flexible vegetation. Figure 4.5 presents the comparison of theoretical and numerical relationships of $\langle\xi\rangle/\langle W\rangle$. The upper panel gives the phase angle of $\langle\xi\rangle/\langle W\rangle$, and the lower panel gives the magnitude of $\langle\xi\rangle/\langle W\rangle$. Excellent agreement is achieved. For extremely stiff vegetation, the plant stem barely moves in the water, thus exhibits almost a $90°$ phase shift between the vegetation deflection and water particle movement (or no phase difference between

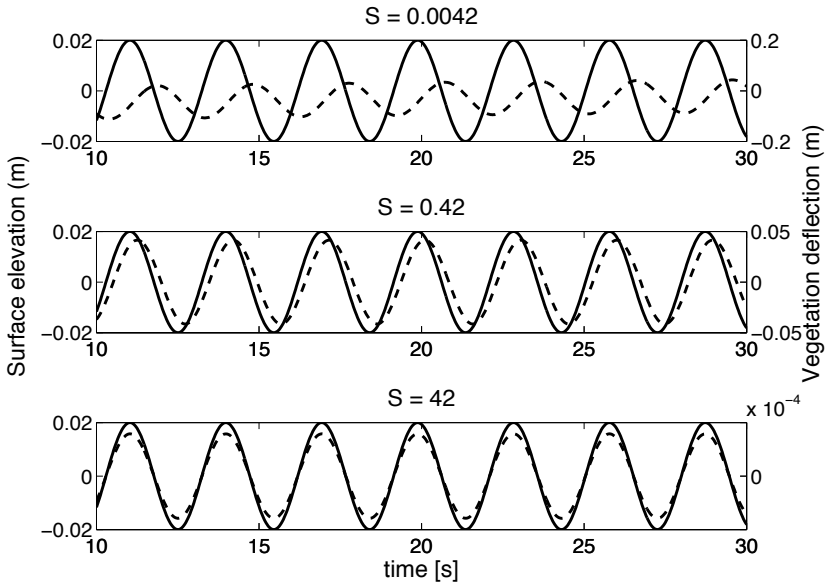

FIGURE 4.4. Modeled time series of surface elevation (solid line) and deflection (dashed line) at the top end of the vegetation stem for extremely flexible vegetation ($S = 0.0042$), moderately flexible vegetation ($S = 0.42$), and stiff vegetation ($S = 42$), respectively

the vegetation deflection and the free surface elevation). For extremely flexible vegetation, the stem follows the movement of surrounding water particles, thus exhibits almost 0° phase shift and the same movement as water particles.

Figure 4.6 illustrates the computed phase differences between the fluid velocity (dW/dt) and vegetation deflection speed ($d\xi/dt$) at the top end of the vegetation stem for aforementioned three vegetation cases. The numerical results are consistent with the theoretical relationships of $\langle\xi\rangle/\langle W\rangle$ shown in Figure 4.5.

Figure 4.7 shows the time series of the modeled unit drag force at the top end of the vegetation stem for aforementioned three vegetation cases. For stiff vegetation ($S = 42$), a larger drag force is produced and leads to larger energy dissipation; while for flexible vegetation ($S = 0.0042$), a smaller drag force is produced and leads to less energy dissipation.

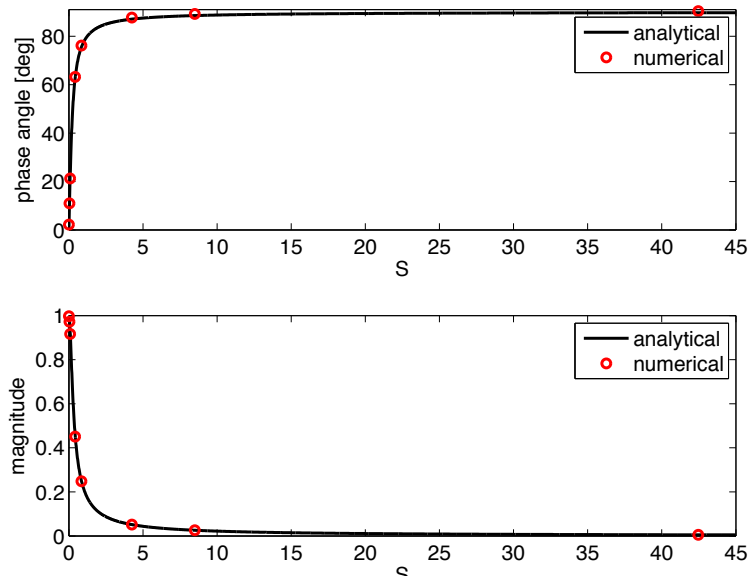

FIGURE 4.5. Theoretical and numerical relationships of $\langle \xi \rangle / \langle W \rangle$

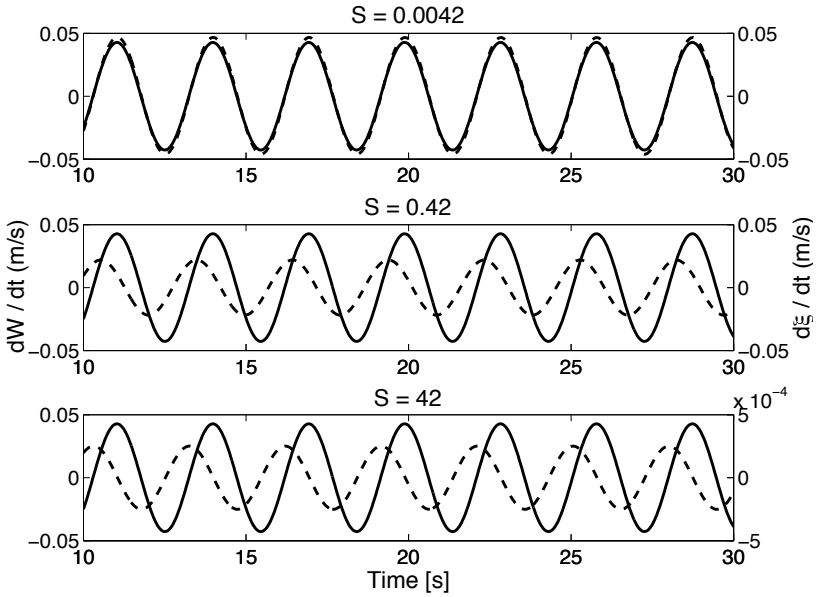

FIGURE 4.6. Computed fluid velocity (dW/dt, solid line) and vegetation deflection speed ($d\xi/dt$, dashed line) at the top end of the vegetation stem for extremely flexible vegetation ($S = 0.0042$), moderately flexible vegetation ($S = 0.42$), and stiff vegetation ($S = 42$), respectively

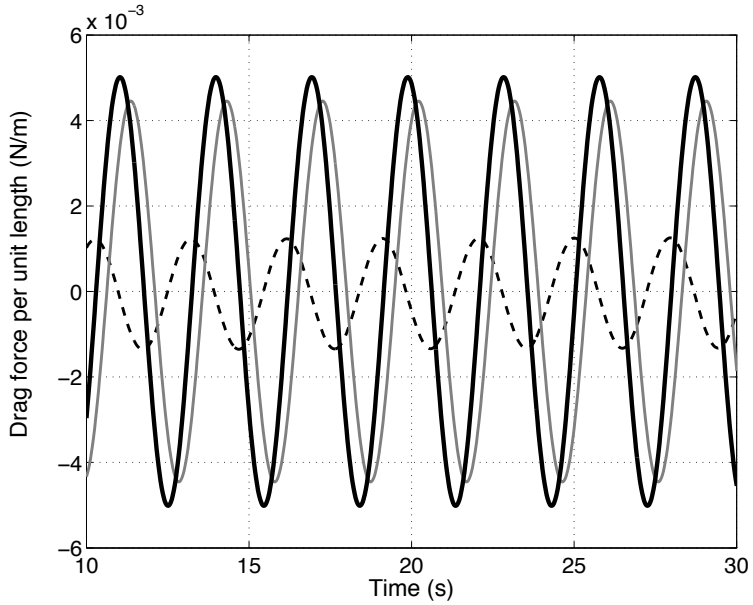

FIGURE 4.7. Modeled time series of unit drag forces at the top end of the vegetation stem for extremely flexible vegetation ($S = 0.0042$, dashed line), moderately flexible vegetation ($S = 0.42$, thin line), and stiff vegetation ($S = 42$, thick line), respectively

4.3.2 Wave attenuation due to multiple swaying vegetation

Asano et al. (1988) conducted a series of laboratory experiments using artificial seaweeds in a 27 m long, 0.5 m wide, and 0.7 m deep flume. The 8 m long vegetation patch was placed from 3 m to 11 m away from the wave maker, and artificial seaweeds were evenly distributed in this area with the density of 1490 and 1110 units/m^2. Each seaweed was 0.25 m long, 5.2 cm wide, and 0.03 mm thick, with a specific gravity of ρ_v/ρ_f = 0.9. A schematic of the numerical setup of the flume is shown in the top panel of Figure 4.9. The other properties of the vegetation stem, inertia coefficient, stiffness, are determined as C_M = 2.0 and E = 9.8$\times 10^6$ Pa, respectively (Asano et al. 1992). Eight numerical simulations are carried out with two different water depths, 0.45 and 0.52 m, respectively for waves with different frequencies, ranging from 0.5 to 1.4 Hz, and different heights. The wave surface elevations are measured at 1 m, 3 m, 5 m, and 7 m away from the front end of the vegetation patch. The complete form of Equation (4.10) is solved in the fully coupled wave-vegetation models with $\Delta x = L/50$ and $\Delta t = T/400$, where L is the wave

length and T is the wave period. The water column is divided into 10 layers and each vegetation stem is divided into 30 segments to minimize any numerical errors. The drag coefficient is the only calibration parameter to best fit the numerical results with experimental data using the method of least squares. Wave conditions, calibrated values of C_D, Reynolds number (Re), and Keulegan-Carpenter number (KC) as well as the vegetation population density are listed in Table 4.1. Re is defined as Re = $b_v u_c/\nu$ and KC is defined as KC = $u_c T/b_v$, where b_v is the plant width, u_c is the characteristic velocity acting on the vegetation, T is the wave period and ν is the kinematic viscosity.

TABLE 4.1. Wave conditions, calibrated values of C_D, Re and KC for 8 test cases of Asano et al. (1988)

Case	Water depth (m)	Wave height (m)	Wave period (s)	Population density (units/m^2)	Re	C_D	KC
1	0.52	0.086	2.00	1490	8544	0.25	6.32
2	0.52	0.093	1.43	1490	8015	0.40	4.24
3	0.45	0.136	1.43	1490	13668	0.40	7.23
4	0.45	0.061	0.83	1110	3897	1.50	1.20
5	0.45	0.138	1.00	1490	10842	0.25	4.01
6	0.45	0.113	1.25	1110	10512	0.40	4.86
7	0.52	0.166	1.25	1490	12802	1.00	5.92
8	0.45	0.123	1.43	1110	12362	0.70	6.54

Figure 4.8 shows the comparison of the experimental and numerical wave heights for 8 runs. The solid line represents the wave height computed by the fully-coupled wave-vegetation models and the dots represent the wave heights from the laboratory experiments. Good agreement is achieved.

A more recent experiment was conducted by Ozeren et al. (2013) (also see Wu et al. 2011) in a 20.6 m long, 0.69 m wide, and 1.22 m deep flume at the USDA-ARS National Sedimentation Laboratory (NSL) in Oxford, Mississippi. A 3.66 m long vegetation patch was placed 11.5 m away from the wave maker. A schematic of the numerical setup of the flume is shown in the lower panel of Figure 4.9. In order to reduce the computational cost, the numerical wave maker is placed 2 m from the edge of the vegetation patch. Nine test cases with submergent artifi-

cial plants (rigid and flexible) are selected to further verify our fully coupled wave-vegetation models.

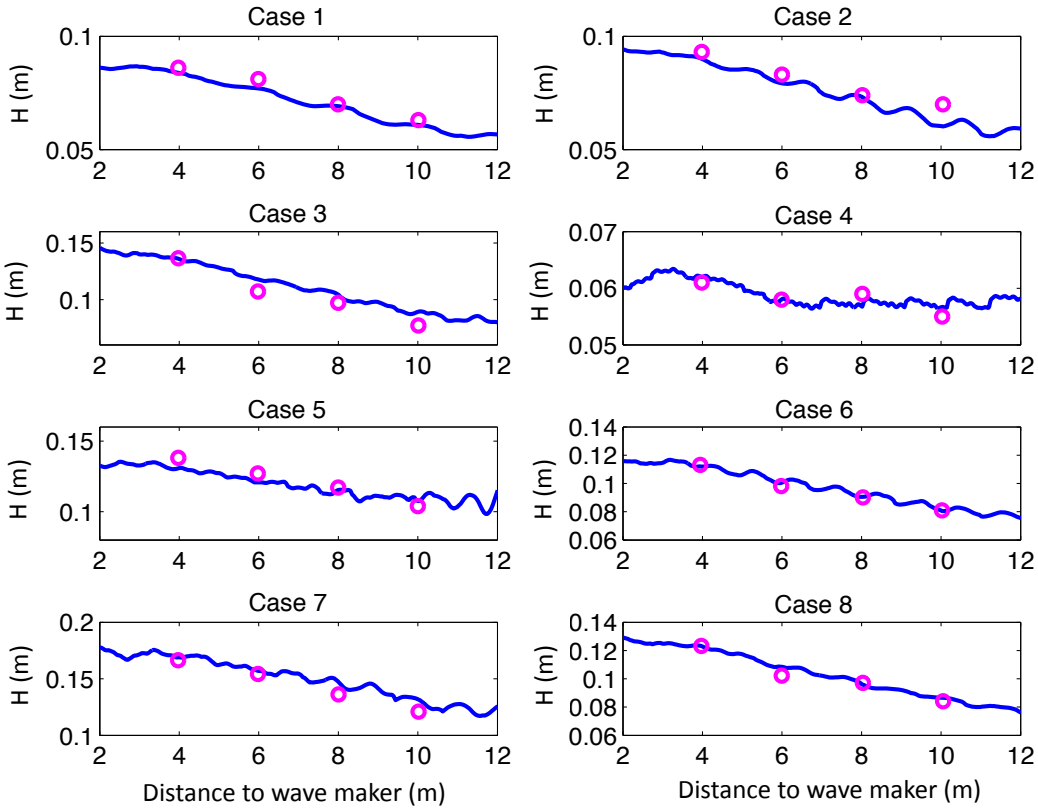

FIGURE 4.8. Numerical and experimental (Asano et al. 1988) wave heights (H) over submerged vegetation field

The rigid model vegetation was made of birch dowels with a length of 0.63 m and a diameter of 9.4 mm. Stems were evenly placed with densities of 350 and 623 units/m^2. The flexible model vegetation was ethylene propylene diene monomer (EPDM) foam-rubber cords with a length of 0.48 m and a diameter of 9.4 mm. The EPDM foam rubber has a density of 368 kg/m^3 and a modulus of elasticity of 4 MPa. Stems were evenly placed with a population density of 350 units/m^2.

The water depth in all nine simulations is 0.7 m. The wave surface elevations are measured at 1.5 m, 3 m, 4.5 m, and 6 m sway from the numerical wave maker. The complete form of Equation (4.10) is solved in the fully coupled wave-vegetation models with $\Delta x = L/50$ and

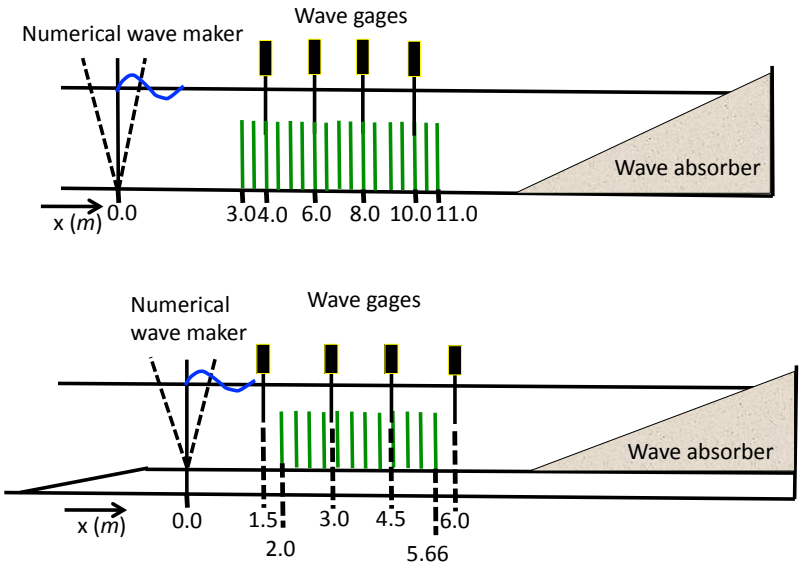

FIGURE 4.9. Schematic of the experimental setup of Asano et al. (1988) and Wu et al. (2011)

$\Delta t = T/400$, where L is the wave length and T is the wave period. The water column is divided into 10 layers and each vegetation stem is divided into 30 segments. The inertia coefficient C_M is fixed to be 2.0. The drag coefficient is the only calibration parameter to best fit the numerical results with experimental data using the method of least squares. Wave conditions, calibrated values of C_D, Re and KC as well as the vegetation population density are listed in Table 4.2.

TABLE 4.2. Wave conditions, calibrated values of C_D, Re and KC for 9 test cases of Wu et al. (2011)

Case	Wave conditions	Vegetation type	Population density (units/m^2)	Re	C_D	KC
1	Wave height = 0.052 m	rigid	350	1098	2.70	14.92
2	Wave period = 1.20 s		623	1098	2.90	14.92
3		flexible	350	735	20.0	9.97
4	Wave height = 0.117 m	rigid	350	2556	2.00	31.80
5	Wave period = 1.10 s		623	2556	2.00	31.80
6		flexible	350	1570	10.0	19.54
7	Wave height = 0.0846 m Wave period = 1.60 s	flexible	350	1414	17.0	24.94
8	Wave height = 0.0752 m Wave period = 1.00 s	flexible	350	1022	18.0	11.27
9	Wave height = 0.0752 m Wave period = 1.00 s	flexible	350	892	18.0	8.36

Figure 4.10 shows the comparison of the experimental and numerical wave heights for 9 runs. The solid line represents the wave height computed by the fully-coupled wave-vegetation models and the dots represent the wave heights from the laboratory experiments. Good agreement is achieved.

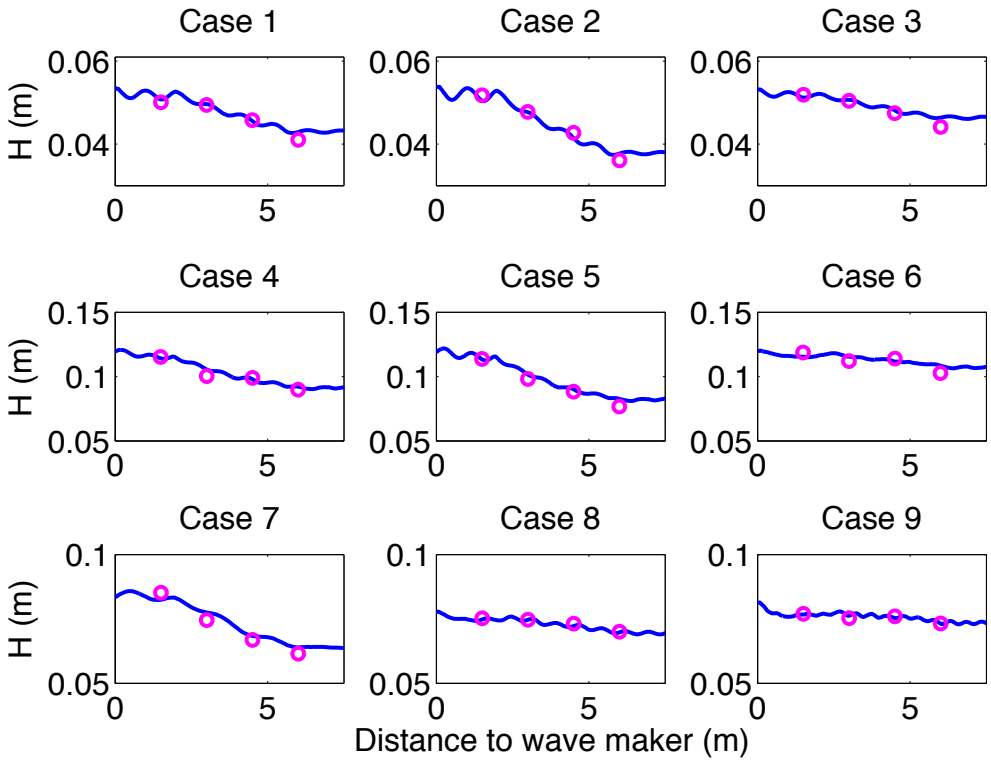

FIGURE 4.10. Numerical and experimental (Wu et al. 2011) wave heights (H) over submerged vegetation field

Kobayashi et al. (1993) proposed an empirical formula of C_D as a function of the Reynolds number Re. In the simulation, u_c is computed as the maximum value of the horizontal velocity at the front end of the vegetation patch at the top of the vegetation stem. The formula proposed by Kobayashi et al. (1993) assumed rigid vegetation, with C_D ranging from 0.15 to 0.19. However, the use of the fluid velocity relative to the vegetation motion in the drag force calculation leads to larger C_D values due to the reduced characteristic velocity u_c. Mendez et al. (1999) introduced

an empirical formula for rigid vegetation stems based on the calibration of their theoretical model using the laboratory data, as follows

$$C_D = 0.08 + \left(\frac{2200}{\text{Re}}\right)^{2.2} \qquad 200 < \text{Re} < 15500 \tag{4.35}$$

Mendez et al. (1999) also developed an empirical formula including the swaying motion of vegetation stems based on the calibration of their theoretical model using the laboratory data, as follows

$$C_D = 0.4 + \left(\frac{4600}{\text{Re}}\right)^{2.90} \qquad 2300 < \text{Re} < 20000 \tag{4.36}$$

Maza et al. (2013) proposed another empirical formula of C_D as

$$C_D = 1.61 + \left(\frac{4600}{\text{Re}}\right)^{1.90} \qquad 2000 < \text{Re} < 7000 \tag{4.37}$$

This formulation also considers the vegetation motion but is based on their numerical results calibrated for the best fit to laboratory measurements. The disagreement between these two formulas for flexible vegetation comes from: (1) different scale of vegetation stiffness, (2) different Re range, and (3) different methods to take into account the wave-vegetation interaction (Maza et al. 2013). Mendez et al. (1999) solved the problem based on the potential flow theory without considering turbulence effects, while Maza et al. (2013) solved the RANS equations with a *k*-ϵ turbulence model. Since our proposed model is based on the Euler equation without turbulence closure, the calibrated C_D value is compared with Mendez et al. (1999) formulation. Figure 4.11 shows the empirical relationships of C_D as a function of Re together with the calibrated value of C_D from the present study. The solid line represents the empirical formulation considering the vegetation swaying effect by Mendez et al. (1999), and the dashed-dotted line represents the formulation for rigid vegetation by Mendez et al. (1999). The dashed line represents the formulation by Maza et al. (2013). The calibrated values of C_D from our numerical simulations for experiments by Asano et al. (1988) are marked with dots, scattering along the

solid line. The calibrated values of C_D from our numerical simulations of the laboratory experiments described in Wu et al. (2012) are marked with crosses for rigid vegetation, and triangles for flexible vegetation, scattering out of the ranges of empirical formulations. However, they are in line with the extrapolation of the formulas for flexible vegetation (solid line) and rigid vegetation (dashed-dotted line) to low Re values. It is seen in Figure 4.11 that not only the vegetation rigidity, but also the turbulence closure in a hydrodynamic model influence the drag coefficient inferred from physical experiments.

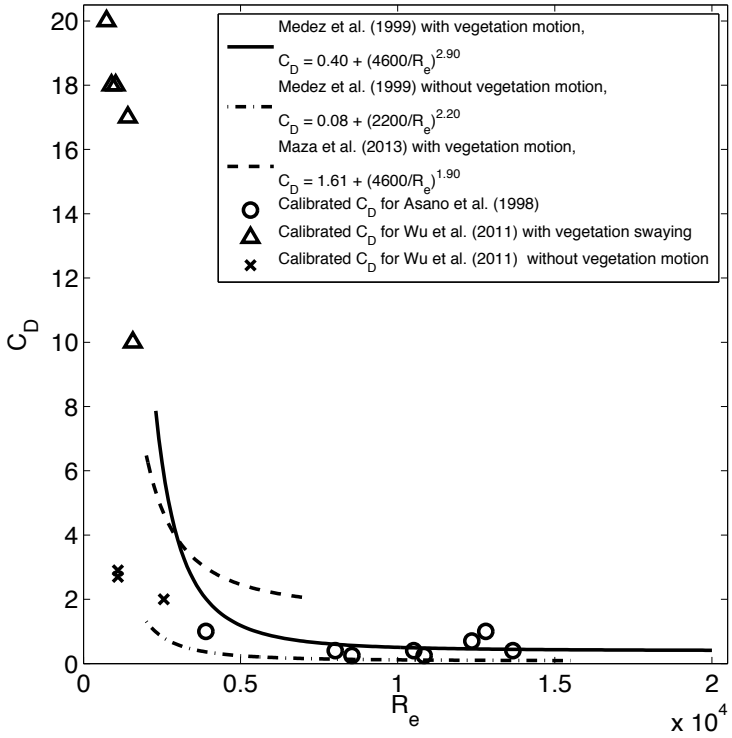

FIGURE 4.11. Empirical and calibrated C_D as a function of Re

4.4 Discussion

A scaling analysis is performed to understand the importance of each force involved in the vegetation motion. In the following derivation, we assume that the plant stem has a circular cross-section, but the procedure can be easily applied to plant stems with rectangular cross-section. The characteristic water particle displacement W_0, wave period T_0, stem length l_0, and

stem radius r_0 are used to non-dimensionalize Equation (4.10). Define the following dimensionless variables

$$\xi^* = \frac{\xi}{W_0}, \;\; W^* = \frac{W}{W_0}, \;\; z^* = \frac{z}{l_0}, \;\; t^* = \frac{t}{T_0}, \;\; I^* = \frac{I}{r_0^4}, \;\; V^* = \frac{V}{r_0^2} \tag{4.38}$$

Substituting Equation (4.38) into Equation (4.10) yields

$$\begin{aligned} &\frac{\rho_f r_0^2 W_0}{T_0^2} V^* \ddot{\xi}^* + \frac{C_1 W_0}{T_0} \dot{\xi}^* + \frac{E r_0^4 W_0}{l_0^4} I^* \xi^{*(4)}_z + \frac{(\rho_f - \rho_v) g r_0^2 W_0}{l_0} V^* \xi^{*(1)}_z = \\ &\frac{\rho_f C_D r_0 W_0^2}{T_0^2} \Big(\dot{W}^* - \dot{\xi}^*\Big)\Big|\dot{W}^* - \dot{\xi}^*\Big| + \frac{\rho_f r_0^2 W_0}{T_0^2} V^* \Big[C_M \ddot{W}^* - \big(C_M - 1\big)\ddot{\xi}^*\Big] \end{aligned} \tag{4.39}$$

The stiffness of vegetation stem is a primary restoring force in vegetation oscillation. Dividing Equation (4.39) by $E r_0^4 W_0 / l_0^4$ yields a dimensionless governing equation for vegetation motion

$$\begin{aligned} &\frac{\rho_v l_0^4}{E r_0^2 T_0^2} V^* \ddot{\xi}^* + \frac{C_1 l_0^4}{E r_0^4 T_0} \dot{\xi}^* + I^* \xi^{*(4)}_z + \frac{(\rho_f - \rho_v) g l_0^3}{E r_0^2} V^* \xi^{*(1)}_z = \\ &\frac{\rho_f C_D l_0^4 W_0}{E r_0^3 T_0^2} \Big(\dot{W}^* - \dot{\xi}^*\Big)\Big|\dot{W}^* - \dot{\xi}^*\Big| + \frac{\rho_f l_0^4}{E r_0^2 T_0^2} V^* \Big[C_M \ddot{W}^* - \big(C_M - 1\big)\ddot{\xi}^*\Big] \end{aligned} \tag{4.40}$$

Denote the dimensionless coefficient of each term as

$$S_1 = \frac{\rho_v l_0^4}{E r_0^2 T_0^2}, \;\; S_2 = \frac{C_1 l_0^4}{E r_0^4 T_0}, \;\; S_3 = \frac{(\rho_f - \rho_v) g l_0^3}{E r_0^2}, \;\; S_4 = \frac{\rho_f C_D l_0^4 W_0}{E r_0^3 T_0^2}, \;\; S_5 = \frac{\rho_f l_0^4}{E r_0^2 T_0^2} \tag{4.41}$$

The dimensionless governing equation can be rewritten as

$$\underline{S_1 V^* \ddot{\xi}^*} \; + \; \underline{S_2 \dot{\xi}^*} \; + \; \underline{I^* \xi^{*(4)}_z} + \underline{S_3 V^* \xi^{*(1)}_z} = \underline{S_4 (\dot{W}^* - \dot{\xi}^*)|\dot{W}^* - \dot{\xi}^*|} + \underline{S_5 V^* [C_M \ddot{W}^* - (C_M - 1)\ddot{\xi}^*]} \tag{4.42}$$

Buoyancy Damping Stiffness Gravity Drag Inertia

Equation (4.42) is an extension of the scaling analysis in Mullarney et al. (2010) to the full equation of force balance for the vegetation motion, where the left consists of the restoration forces and the right shows the driving forces. If we neglect forces other than stiffness and drag, Equation (4.42) becomes $S_4^{-1} I^* \xi^{*(4)}_z = \Big(\dot{W}^* - \dot{\xi}^*\Big)\Big|\dot{W}^* - \dot{\xi}^*\Big|$. S_4^{-1} is identical to S in Equation (4.34).

Comparing the two major driving forces, the importance of drag over inertia is given by

$$\frac{S_4}{S_5} = \frac{C_D W_0}{r_0} \propto \text{KC} \tag{4.43}$$

This ratio is proportional to the Keulegan-Carpenter number. For KC < 3, the inertia force is dominant and the drag force can be neglected; for $3 \leq$ KC < 15, the drag force can be assumed to be linear; for $15 \leq$ KC < 45, the full Morison equation should be employed and the drag force can no longer be linearized; for KC ≥ 45, the drag force is dominant and the inertia can be neglected (Journée and Massie 2001).

Comparing the restoring forces (e.g., damping, stiffness and gravity), the importance of the stiffness of the vegetation stem over other restoring forces is expressed by the factors S_2 and S_3. Damping is an important restoring force for vegetation motion compared with buoyancy and gravity. Inclusion of damping would affect the vegetation deformation, therefore the wave attenuation. Still ignoring inertia and gravity, but including damping, a theoretical relationship between the movement of vegetation stem and water particle can be derived from Mullarney et al. (2010). The drag is linearized as in Equation (4.33). The governing equation expressing a balance between damping, stiffness, and drag becomes

$$S_2 \dot{\xi}^* + I^* \xi_z^{(4)} = S_4 \left(\dot{W}^* - \dot{\xi}^* \right) \tag{4.44}$$

To be consistent with the expression in Mullarney et al. (2010), Equation (4.44) is rewritten as

$$(S_d + 1)\dot{\xi}^* + S I^* \xi_z^{(4)} = \dot{W}^* \tag{4.45}$$

where

$$S_d = \frac{S_2}{S_4} = \frac{C_1 T_0}{\rho_f C_D r_0 W_0} \tag{4.46}$$

We first look into the homogeneous differential equation

$$(S_d + 1)\dot{\xi}^* + S I^* \xi_z^{(4)} = 0 \tag{4.47}$$

Assuming $\xi(z,\ t) = \phi(z)f(t)$, and substituting this expression into Equation (4.47), we get

$$\frac{S}{S_d + 1} I^* \phi_n^{(4)} f + \phi_n f' = 0 \tag{4.48}$$

We get a new dimensionless stiffness $\hat{S}$, which incorporates characteristics of waves and material as well as geometric properties of the vegetation, especially the damping ratio.

$$\hat{S} = \frac{S}{S_d + 1} = \frac{E r_0^4 T_0^2}{l_0^4 (C_1 T_0 + \rho_f C_D r_0 W_0)} \tag{4.49}$$

The above analysis indicates that the theoretical expression of $\langle \xi \rangle / \langle W \rangle$ in Mullarney et al. (2010) can be applied to the case with both restoring forces of damping and stiffness if S is replaced by $\hat{S}$.

4.5 Conclusions

A fully coupled wave-vegetation model for simulating the interaction between water waves and submerged flexible plants has been developed, analyzed and validated. The wave model is based on the non-hydrostatic free surface flow model, NHWAVE, and the vegetation model solves the complete force balance equation for beam deformation using a high-order finite element method. The key findings are as follows:

1. The numerical model is in excellent agreement with the analytical solution given by Mullarney et al. (2010) for the single-stem swaying vegetation;

2. Numerical results agree well with two sets of experimental data of large-scale swaying vegetation. The calibrated values of C_D follow the empirical formulation proposed by Mendez et al. (1999). The new model for flexible vegetation solving the complete deformation equation with the fourth-order finite element method can be coupled with other existing nonlinear, dispersive wave models;

3. A scaling analysis has been performed on the complete force balance equation for beam deformation to help understand the significance of each force involved in the vegetation

vibration in response to the wave action. Dimensionless parameters have been derived to measure the relative importance of each force;

4. One of the new parameters allows for measuring the significance of the damping term in comparison with the stiffness term. The theoretical relationship between the vegetation deflection and water particle movement derived by Mullarney et al. (2010) has been extended to including both restoring forces. A new dimensionless parameter $\hat{S}$, incorporating characteristics of waves and material as well as geometric properties of the vegetation has been obtained. $\hat{S}$ approaches S if the damping term is much smaller than the stiffness term and negligible.

CHAPTER 5 SUMMARY AND CONCLUSIONS

The primary objective of this study is to develop an efficient and accurate non-hydrostatic wave model for fully dispersive and highly nonlinear waves, and investigate the interaction between waves and submerged flexible vegetation using a fully coupled wave-vegetation model. Two sets of equations, Euler equations in σ-coordinate and vegetation motion equation, have been solved. Different numerical methods including finite difference, finite volume, finite element, spectral element, and discontinuous Galerkin methods have been applied in this study.

Chapter 2 introduced an analytical dispersion relationship of waves simulated by Euler models utilizing the Keller-box scheme and central differencing for vertical discretization. The phase speed of linear waves simulated by the semi-discretized Euler model is expressed as a rational polynomial function of the dimensionless water depth, kh, and the layer distribution in the water column becomes an optimizable parameter in this function. The dispersion error has been obtained by comparing this phase speed against the exact solution based on the linear wave theory. It is shown that for a given dispersion error (e.g. 1%), the range of kh can be extended if the layer thicknesses are optimally selected.

A simple loop algorithm was devised to find out the optimal layer thickness. For instance, for the two-layer model, since the ratio of the bottom layer thickness to the water depth, α_1, plays as the only free parameter in the dispersion error expression, we started at $\alpha_1 = 0.01$ (1% of water depth h) with an increment of 0.001 and select the optimal α_1 to maximize the range of kh for the given tolerance dispersion error. For the two-layer model, with the tolerance dispersion error set as 1%, the upper limit of kh is 9.08 with the optimal layer distribution of 67%-33% (from bottom to top) of the water depth. For the three-layer model, with the tolerance dispersion error set as 1%, the upper limit of kh is 49.5 with the optimal layer distribution of 68% - 26.5% - 5.5% (from bottom to top) of the water depth.

For demonstration purpose, an Euler model for dispersive nonlinear water waves has been developed using the Keller-box scheme and following the numerical algorithm presented in Zijlema and Stelling (2005), except that the finite difference method and σ-coordinate are applied. The derived phase speed was tested against both numerical and exact solutions of standing waves for various cases. Excellent agreement was achieved. The model was also tested using the fifth-order Stokes theory for nonlinear standing waves. The phase speed of simulated nonlinear waves follows a trend similar to linear waves; therefore, the optimal layer distribution can be applied to nonlinear waves simulations as well.

The derivation of the dispersion relationships can be extended to any number of layers. The derived dispersion relationships for two- and three-layer models can also be applied to other Euler models that utilize the Keller-box scheme and central differencing for vertical discretization. Moreover, the methodology can be applied to other non-hydrostatic models for water waves to minimize the number of layers needed to simulate a wide spectrum of ocean waves from deep to shallow waters.

Chapter 3 developed an efficient and accurate approach to solve Euler equations for fully dispersive and highly nonlinear water waves. σ-coordinate was employed to allow high resolution near the bottom and capture the changing free surface. DG formulations were adopted for horizontal discretization. The numerical libraries provided by Hesthaven and Warburton (2007) have been extended to solve the hydrostatic part of the model. FD formulations and SE formulations were employed for vertical discretization and Poisson equations, respectively. The adoption of the Keller-box scheme (Zijlema and Stelling 2005, 2008; Zhu et al. 2014) is attributed to its capability of accurately simulating highly dispersive waves using a relatively small number of layers (two or three layers). And the employment of the SE method for the Poisson equation is in consideration of reducing the overall degrees of freedom since the existing DG-based N-S models for free surface waves (e.g. Grooss and Hesthaven 2006) are computationally expensive

due to their large degrees of freedom. The combination of DG and SE methods can improve the model efficiency for high-order approximations. A three-stage optimal Strong Stability Preserving Runge-Kutta (SSP-RK) scheme was employed for temporal integration. The local elements were connected together by numerical fluxes, evaluated using the Lax-Friedrichs and HLL Riemann solvers. The model was tested for standing waves based on analytical solutions. Also the numerical dispersion relationship of this model agreed well with the theoretical dispersion relationship presented in Chapter 2.

Further testing of the model is still needed. The current application is limited to one horizontal dimension and we seek to extend the model to two horizontal dimensions. The model also needs to incorporate wetting and drying algorithms, be applied to the simulation of wave breaking in the surf zone, wave run-up in the swash region, and breaking-generated currents, and be validated with laboratory data.

Chapter 4 presented a fully coupled wave-vegetation model for simulating the interaction between water waves and submerged flexible plants. Under the work of oscillatory flows, the vegetation motion is subjected to the balance of forces including buoyancy, damping, stiffness of the vegetation, and gravity as restoring forces, and drag and inertia as driving forces. The force balance equation governs the deformation of vegetation plants, and was solved by a high-order finite element method and an implicit time differencing scheme.

Mullarney and Henderson (2010) derived a theoretical relationship between the movement of single-stem vegetation and water particle based on the cantilever beam theory, balancing stiffness with drag on stem elements with the assumption of negligible inertia and buoyancy, small deformations, and thin near-vertical stems. The vegetation model presented in Chapter 3 was in excellent agreement with the analytical solution given by Mullarney and Henderson (2010) for the single-stem swaying vegetation. Also a scaling analysis has been performed on the complete force balance equation for beam deformation to help understand the significance

of each force involved in the vegetation vibration in response to the wave action. Dimensionless parameters have been derived to measure the relative importance of each force. For cases where damping becomes significant compared with other restoring forces, a theoretical relationship between movements of vegetation stem and water particle has been derived, and a dimensionless parameter, incorporating characteristics of waves and material as well as geometric properties of vegetation has been obtained.

This vegetation model can be coupled with any phase-resolving wave model, such as Boussinesq-type models (e.g. Madsen et al. 1992; Chen et al. 2000; Lynett and Liu 2004; Shi et al. 2012), non-hydrostatic models (e.g. Wu et al. 2010; Zijlema et al. 2011; Ma et al. 2012), and RANS-VOF models (e.g. Lin and Liu 1998). At each computation step of the wave model, the flow information such as velocities and surface elevation will be fed into the vegetation model, which computes the effective vegetation height and vegetation-induced resistance in return. These outcomes will be fed back to the wave model as a source term in the momentum equation for the next step of computation. In this study a vegetation deformation model has been developed, and the algorithm and numerical scheme by Ma et al. (2012) were implemented into the Euler solver. This fully coupled model has been rigorously validated by comparing numerical results with two sets of experimental data of large-scale swaying vegetation. Excellent agreement was achieved. The calibrated values of C_D followed the empirical formulation proposed by Mendez et al. (1999).

REFERENCES

[1] Agnon, Y., Madsen, P.A., Schäffer, H., 1999. A new approach to high order Boussinesq models. *J. Fluid Mech.* 399, 319-333.

[2] Aizinger, V., Dawson, C., Cockburn, B., Castillo, P., 2000. The local discontinuous Galerkin method for contaminant transport. *Adv. Water Resour.* 24(1), 73-87.

[3] Aizinger, V., Dawson, C., 2002. A discontinuous Galerkin method for two-dimensional flow and transport in shallow water. *Adv. Water Resour.* 25(1), 67-84.

[4] Anderson, M. E., Smith, J. M. and McKay, S. K., 2011. Wave dissipation by vegetation. *Coastal and Hydraulics Engineering Technical Note ERDC/CHL CHETN-I-82*. U.S. Army Engineer Research and Development Center, Vicksburg, MS.

[5] Anderson, M. E. and Smith, J. M., 2014. Wave attenuation by flexible, idealized salt marsh vegetation. *Coast. Eng.* 83, 82-92.

[6] Arnold, D., 1982. An interior penalty finite element method with discontinuous elements. *SIAM J. Numer. Anal.* 19, 742-760.

[7] Arnold, D.N., Brezzi, F., Cockburn, B., and Marini, D., 2000. Discontinuous Galerkin methods for elliptic problems. In Discontinuous Galerkin Methods: Theory, Computation and Applications. Springer-Verlag, Berlin, 135146.

[8] Arnold, D. N., Brezzi, F., Cockburn, B., Marini, L. D., 2002. Unified analysis of discontinuous Galerkin methods for elliptic problems. *SIAM J. Numer. Anal.* 39, 1749-1779.

[9] Asano, T., Tsutsui, S., and Sakai, T., 1988. Wave damping characteristics due to seaweed. *Proc. of the 35th Coastal Eng. Conf. in Japan.*, Japan Soc. of Civil Eng, Matsuyama, 138-142 (in Japanese).

[10] Asano, T., Deguchi, H., and Kobayashi, N., 1992. Interactions between water waves and vegetation. *Proc. of the 23rd Int. Conf. Coastal Eng. (ICCE)*, ASCE, 2710-2723.

[11] Augustin, L. N., Irish, J. L., and Lynett, P., 2009. Laboratory and numerical studies of wave damping by emergent and near-emergent wetland vegetation. *Coast. Eng.* 56, 332-340.

[12] Bai, Y., Cheung, K. F., 2013. Dispersion and nonlinearity of multi-layer non-hydrostatic free-surface flow.*J. Fluid Mech.* 726, 226.

[13] Bassi, F., Rebay, S., 1997. A high-order accurate discontinuous Galerkin finite element method for the numerical solution of the compressible Navier-Stokes equations. *J. Comput. Phys.* 131, 267-279.

[14] Bassi, F., Crivellini, A., Rebay, S., Savini, M., 2005. Discontinuous Galerkin solution of the Reynolds-averaged Navier Stokes and $k - \omega$ turbulence model equations. *Comput. Fluids* 34, 507-540.

[15] Blackmar, P. J., Cox, D. T., and Wu, W. C., 2014. Laboratory observations and numerical simulations of wave height attenuation in heterogeneous vegetation. *J. Waterway, Port, Coastal, Ocean Eng.* 140(1), 56-65.

[16] Blain, A., and Massey, C., 2005. Application of a coupled discontinuouscontinuous Galerkin finite element shallow water model to coastal ocean dynamics. *Ocean Model.* 10(34), 283-315.

[17] Botti, L., and Pietro, D., 2011. A pressure-correction scheme for convection-dominated incompressible flows with discontinuous velocity and continuous pressure. *J. Comput. Phys.* 230, 572-585.

[18] Bradley, K., and Houser, C., 2009. Relative velocity of seagrass blades: implications for wave attenuation in low-energy environments. *J. Geophys. Res.* 114, F01004.

[19] Bradford, S.F., and Sanders, B.F. 2005. Performance of high-resolution, non-level bed, shallow-water models. *J. Eng. Mech.* 131(10), 1073-1081.

[20] Casulli, V., Zanolli, P., 2002. Semi-implicit numerical modeling of nonhydrostatic free-surface flows for environmental problems. *Mathematical and Computer Modelling* 36, 1131-1149.

[21] Chazel, F., Benoit, M., Ern, A., Piperno, S., 2009. A double-layer Boussinesq-type model for highly nonlinear and dispersive waves. *R. Soc. Lond.* A 465, 2319-2346.

[22] Chen, Q., Madsen, P. A., Schäffer, H. A., Basco, D. R., 1998. Wave-current interaction based on an enhanced Boussinesq approach. *Coast. Eng.* 33, 11-39.

[23] Chen, Q., Madsen, P. A., Basco, D. R., 1999. Current effects on nonlinear interactions of shallow-water waves. *J. Waterw. Port Coast. Ocean Eng.* 125 (4), 176-186.

[24] Chen, Q. and Zhao, H., 2012. Theoretical models for wave energy dissipation caused by vegetation. *J. Eng. Mech.* 138(2), 221-229.

[25] Chen, Q., Fan, Q., Ko, S. H., Huang, H., Allen, G., 2011. An Euler solver for nonlinear water waves using a modified staggered grid and Gaussian quadrature approach. *Proc. of the 6th Int. Conf. on Fluid Mech.* June 30-July 3, 2011, Guangzhou, China.

[26] Cockburn, B., and Lin, S.Y., 1989. TVB Runge-Kutta local projection discontinuous Galerkin finite element method for conservation laws III: one-dimensional systems. *J. Comput. Phys.* 84, 90-113.

[27] Cockburn, B., and Shu, C.-W., 1989. TVB Runge-Kutta local projection discontinuous Galerkin finite element method for conservation laws. II. General framework. *Math. Comp.* 52(186), 411-435.

[28] Cockburn, B., and Shu, C.-W., 1998. The local discontinuous Galerkin method for time-dependent convection-diffusion systems. *SIAM J. Numer. Anal.* 35, 2440-2463.

[29] Cockburn, B., Hou, H., and Shu, C.-W., 1990. The Runge-Kutta local projection discontinuous Galerkin finite element method for conservation laws. IV. The multidimensional case. *Math. Comp.* 54(190), 545-581.

[30] Cockburn, B., and Shu, C.-W., 1991. The P^1-RKDG method for two-dimensional Euler equations of gas dynamics. *ICASE Report* 91-32.

[31] Cockburn, B., Karniadakis, G. E, and Shu. C.-W., 2000. The development of discontinuous Galerkin methods. Springer Berlin Heidelberg.

[32] Cockburn, B., Kanschat, G., Schötzau, D., 2005a. A locally conservative LDG method for the incompressible Navier-Stokes equations. *Math. Comp.* 74, 1067-1095.

[33] Cockburn, B., Kanschat, G., Schötzau, D., 2005b. The local discontinuous Galerkin method for linearized incompressible fluid flow: A review. *Comput. Fluids* 34, 491-506.

[34] Cramer, G., 1750. Intr. à l'analyse de lignes courbes algébriques (in French). Geneva, 657-659.

[35] Dalrymple, R. A., Kirby, J. T., and Hwang, P. A., 1984. Wave diffraction due to areas of energy dissipation. *J. Waterw. Port Coast. Ocean Eng.* 110, 67-79.

[36] Dalrymple, R.A., Rogers, B.D., 2006. Numerical modeling of water waves with the SPH method. *Coast Engng.* 53, 141-147.

[37] Dawson, C., Kubatko, E. J., Westerink, J. J., Trahan, C., Mirabito, C., Michoski, C., Panda, N., 2011. Discontinuous Galerkin methods for modeling Hurricane storm surge. *Adv. Water Resour.* 34(9), 1165-1176.

[38] Dawson, C., Proft, J., 2002a. Discontinuous and coupled continuous/discontinuous Galerkin methods for the shallow water equations. *Comput. Methods Appl. Mech. Engrg.* 191, 4721-4746.

[39] Dawson, C., Proft, J., 2002b. Coupling of continuous and discontinuous Galerkin methods for transport problems. *Comput. Methods Appl. Mech. Engrg.* 191, 3213-3231.

[40] Dawson, C., Westerink, J. Feyen, J., and Pothina, D. 2006. Continuous, discontinuous and coupled discontinuouscontinuous Galerkin nite element methods for the shallow water equations. *Int. J. Numer. Meth. Fluids* 52, 63-88.

[41] Dijkstra, J. T. and Uittenbogaard, R. E., 2010. Modeling the interaction between flow and highly flexible aquatic vegetation. *Water Resour. Res.* 46, W12547.

[42] Donea, J., Giuliani, S. and Halleux, J.P., 1982. An arbitrary lagrangian-eulerian finite element method for transient dynamic fluid-structure interactions. *Comput. Methods Appl. Mech. Engrg.* 33(1-3), 689-723.

[43] Douglas, J., Dupont, T., and Dupont, Jr., 1976. Interior penalty procedures for elliptic and parabolic Galerkin methods. *Lecture Notes in Physics* Springer-Verlag, Berlin, 58.

[44] DuPont, S., Gosselin, F., Py, C., de Langre, E., Hemon, P., and Brunet, Y., 2010. Modelling waving crops using large-eddy simulation: comparison with experiments and a linear stability analysis. *J. Fluid Mech.* 652, 5-44.

[45] Dubi, A., and Torum, A., 1996. Wave energy dissipation in kelp vegetation. *Proc. of the 25th Int. Conf. Coastal Eng. (ICCE)* ASCE, 2626-2639.

[46] Engsig-Karup, A. P., Hesthaven, J. S., Bingham, H. B., Madsen, P. A., 2006. Nodal DG-FEM solution of high-order Boussinesq-type equations. *J. Eng. Math.* 56, 351-370.

[47] Engsig-Karup, A. P., Hesthaven, J. S., Bingham, H. B., and Warburton, T., 2008. DG-FEM solution for nonlinear wave-structure interaction using Boussinesq-type equations. *Coast. Eng.* 55, 197208.

[48] Engquist, B., and Osher, S., 1981. One-sided difference approximations for nonlinear conservation laws. *Math. Comp.* 36, 321-351.

[49] Eskilsson, C., Sherwin, S. J., 2004. A triangular spectral=hp discontinuous Galerkin method for modelling 2D shallow water equations. *Int. J. Numer. Meth. Fluids* 45, 605-623.

[50] Eskilsson, C., Sherwin, S. J., 2005. Discontinuous Galerkin spectral/hp element modelling of dispersive shallow water systems. *J. Sci. Comput.* 22-23, 269-288.

[51] Eskilsson, C., Sherwin, S. J., 2006. Spectral/hp discontinuous Galerkin methods for modelling 2D Boussinesq equations. *J. Comput. Phys.* 212(2), 566-589.

[52] Fathi-Moghadam, M., Kashefipour, M., Ebrahimi, N., and Emamgholizadeh, S., 2011. Physical and numerical modeling of submerged vegetation roughness in rivers and flood plains. *J. Hydrol. Eng.* 16(11), 858-864.

[53] Giraldo, F. X., and Warburton, T., 2008. A high-order triangular discontinuous Galerkin oceanic shallow water model. *Int. J. Numer. Meth. Fluids* 56, 899-925.

[54] Grooss, J., and Hesthaven, J.S., 2006. A level set discontinuous Galerkin method for free surface flows. *Comput. Methods Appl. Mech. Engrg.* 195, 3406-3429.

[55] Gottlieb, S., Shu, C. W., and Tadmor, E., 2001. Strong stability-preserving high-order time discretization methods. *SIAM Rev.* 43 (1), 89-112.

[56] Gobbi, M.F., Kirby, J.T., 1999. Wave evolution over submerged sills: tests of a high-order Boussinesq model. *Coast. Eng.* 37, 57-96.

[57] Gustafsson, B., Kreiss, H.O., Oliger, J., 2001. Partial Differential Equations and Difference Approximations, John Wiley & Sons, New York.

[58] Harten, A., Lax, P., and Van Leer, B., 1983. On upstream differencing and Godunov-type schemes for hyperbolic conservation laws. *SIAM Rev.* 25(1), 35-61.

[59] Harten, A., 1983. High resolution schemes for hyperbolic conservation laws. *J. Comput. Phys.* 49, 357-393.

[60] Hartmann, R., Houston, P., 2006a. Symmetric interior penalty DG methods for the compressible Navier-Stokes equations I: Method formulation. *Int. J. Numer. Anal. Model.* 3, 1-20.

[61] Hartmann, R., Houston, P., 2006b. Symmetric interior penalty DG methods for the compressible Navier-Stokes equations II: Goal-oriented a posteriori error estimation. *Int. J. Numer. Anal. Model.* 3, 141-162.

[62] Harlow, F. H., Welch, J. E., 1965. Numerical calculation of time-dependent viscous incompressible flow of fluid with free surface. *Phys. Fluids* 8, 2182-2189.

[63] Hesthaven, J. S., Warburton, T., 2007. Nodal Discontinuous Galerkin Methods: Algorithms, Analysis, and Applications. Springer-Verlag, New York.

[64] Hirt, C. W., Nichols, B. D., 1981. Volume of fluid (vof) method for the dynamics of free boundaries. *J. Comput. Phys.* 39, 201-225.

[65] Hughes, T. J. R., 1987. The finite element method: linear static and dynamic finite element analysis. Prentice-Hall, Inc., Englewood Cliffs, New Jersey.

[66] HYPRE. http://acts.nersc.gov/hypre/ [accessed: Jan. 3, 2014].

[67] Iimura, K. and Tanaka, N., 2012. Numerical simulation estimating effects of tree density distribution in coastal forest on tsunami mitigation. *Ocean Eng.* 54, 223-232.

[68] Ikeda, S., Yamada, T., and Toda, Y., 2001. Numerical study on turbulent flow and honami in and above flexible plant canopy. *Int. J. Heat Fluid Flow* 22, 252-258.

[69] Jadhav, R. S. and Chen, Q., 2013. Probability distribution of wave heights attenuated by salt marsh vegetation during tropical cyclone. *Coast. Eng.* 82, 47-55.

[70] Jadhav, R. S., Chen, Q. and Smith, J. M., 2013. Spectral distribution of wave energy dissipation by salt marsh vegetation. *Coast. Eng.* 77, 99-107.

[71] Journée, J. M. J. and Massie, W. W., 2001. Offshore hydromechanics. 1st edition, Delft University of Technology.

[72] Kesserwani, G., Ghostine, R., Vazquez, J., Ghenaim, A., Mose, R., 2008a. Riemann solvers with Runge-Kutta discontinuous Galerkin schemes for the 1D shallow water equations. *J. Hydraul. Eng.* 134(2), 243-255.

[73] Kesserwani, G., Ghostine, R., Vazquez, J., Ghenaim, A., Mose, R., 2008b. Application of a second-order Runge-Kutta discontinuous Galerkin scheme for the shallow water equations with source terms. *Int. J. Numer. Meth. Fluids.* 56(7), 805-821.

[74] Kobayashi, N., Raichle, A. W., and Asano, T., 1993. Wave attenuation by vegetation. *J. Waterw. Port Coast. Ocean Eng.* 119(1), 30-48.

[75] Koftis, T., Prinos, P., and Stratigaki, V., 2013. Wave damping over artificial Posidonia oceanica meadow: A large-scale experimental study. *Coast. Eng.* 73, 71-83.

[76] Kubatko, E. J., Westerink, J. J., Dawson, C., 2006. hp discontinuous Galerkin methods for advection dominated problems in shallow water flow. *Comput. Methods Appl. Mech. Eng.* 196(1-3), 437- 451.

[77] Lai, W., Khan, A. A., 2012. A discontinuous Galerkin method for two-dimensional shallow water flows. *Int. J. Numer. Meth. Fluids.* 70(8), 939-960.

[78] LeVeque, R. J., 2002. Finite volume methods for hyperbolic problems. Cambridge University Press, Cambridge.

[79] Li, B.Q., 2006. Discontinuous finite elements in fluid dynamics and heat transfer. Springer Series in Computational Fluid and Solid Mechanics, Springer-Verlag, Berlin.

[80] Li, C. W. and Yan, K., 2007. Numerical investigation of wave-current-vegetation interaction. *J. Hydraul. Eng.* 133, 794-803.

[81] Li, C. W. and Xie, J. F., 2011. Numerical modeling of free surface flow over submerged and highly flexible vegetation. *Adv. Water Resour.* 34, 468-477.

[82] Lin, P. and Liu, P. L., 1998. A numerical study of breaking waves in the surf zone. *J. Fluid Mechanics* 359, 239-264.

[83] Liu, J. G., Shu, C.-W., 2000. A high-order discontinuous Galerkin method for 2D incompressible flows. *J. Comput. Phys.* 160, 577-596.

[84] Longuet-Higgins, M. S., 1973. On the form of the highest progressive and standing waves in deep water. *Proc. R. Soc. Lond.* A331, 445-456.

[85] Lynett, P., Liu, P.L.-F., 2004a. A two-layer approach to wave modeling. *R. Soc. Lond.* A8, 2637-2669.

[86] Lynett, P., Liu, P.L.-F., 2004b. Linear analysis of the multi-layer model. *Coast. Eng.* 51, 439-454.

[87] Ma, G., Shi, F., Kirby, J. T., 2012. Shock-capturing non-hydrostatic model for fully dispersive surface wave processes. *Ocean Modelling* 43-44, 22-35.

[88] Ma, G., Kirby, J. T., Su, S.-F., Figlus, J., and Shi, F. 2013. Numerical study of turbulence and wave damping induced by vegetation canopies. *Coast. Eng.* 80, 68-78.

[89] Madsen, P.A., Sorensen, O.R., 1992. A new form of Boussinesq equations with improved linear dispersion characteristics. Part 2. A slowly-varying bathymetry. *Coastal Eng.* 18, 183-204.

[90] Madsen, P.A., Schäffer, H.A., 1998. Higher order Boussinesq-type equations for surface gravity wavesderivation and analysis. *R. Soc. Lond.* A 356, 1-60.

[91] Madsen, P.A., Bingham, H.B., Liu, H., 2002. A new Boussinesq method for fully nonlinear waves from shallow to deep water. *J. Fluid Mech.* 462, 1-30.

[92] Meijerink JA, Van der Vorst HA., 1977. An iterative solution method for linear systems of which the coecient matrix is a symmetric M-matrix. *Mathematics of Computation* 31, 148-162.

[93] Méndez, F. J., Losada, I. J., Losada, M. A., 1999. Hydrodynamics induced by wind waves in a vegetation field. *J. Geophys. Res.* 104, 18383-18396.

[94] Maza, M., Lara, J. L., and Losada, I. J. 2013. A coupled model of submerged vegetation under oscillatory flow using Navier-Stokes equations. *Coast. Eng.* 80, 16-34.

[95] Michell, J. H., 1893. The highest waves in water. *Phil. Mag. London* 36, 430-437.

[96] Möller, I., T. Spencer, J.R. French, D.J. Leggett, and M. Dixon., 1999. Wave transformation over salt marshes: A field and numerical modelling study from North Norfolk, England. *Estuarine, Coastal, and Shelf Science* 49(3), 411-426.

[97] Mozolevski, I., Suli, E., Bosing, P., 2006. Discontinuous Galerkin finite element approximation of the two-dimensional Navier-Stokes equations in stream function formulation. *Comm. Numer. Methods Eng.* 23.

[98] Mullarney, J. C. and Henderson, S. M. 2010. Wave-forced motion of submerged single-stem vegetation. *J. Geophys. Res.* 115, C12061.

[99] Nwogu, O., 1993. Alternative form of Boussinesq equations for nearshore wave propagation. *J. Waterw. Port Coast. Ocean Eng.* 119 (6), 618-638.

[100] Osher, S., Sethian, J. A., 1988. Fronts propagating with curvature-dependent speed: Algorithms based on Hamilton-Jacobi formulations. *J. Comput. Phys.* 79, 12-49.

[101] Ozeren, Y., Wren, D. G., and Wu, W., 2013. Experimental Investigation of Wave Attenuation through Model and Live Vegetation. *J. Waterway, Port, Coastal, Ocean Eng.* 04014019.

[102] Panda, N., Dawson, C., Zhang, Y., Kennedy, A., Westerink, J., and Donahue, A., 2014. Discontinuous Galerkin methods for solving BoussinesqGreenNaghdi equations in resolving nonlinear and dispersive surface water waves. *J. Comput. Phys.* 273, 572-588.

[103] Paul, M., Bouma, T. J., and Amos, C. L., 2012. Wave attenuation by submerged vegetation: combining the effect of organism traits and tidal current. *Mar. Ecol. Prog. Ser.* 444, 31-41.

[104] Phillips, N.A., 1957. A coordinate system having some special advantages for numerical forecasting. *J. Meteor.* 14, 184-185.

[105] Reed, W. H., and Hill, T. R., 1973. Triangular Mesh Methods for the Neutron Transport Equation. *Tech. Report LA-UR-73-479* Los Alamos Scientific Laboratory, Los Alamos, NM.

[106] Riviere, B., Wheeler M., and Girault V., 1999. Improved energy estimates for interior penalty, constrained and discontinuous Galerkin methods for elliptic problems. Part I. *Comput. Geosci.* 3(3), 337-360.

[107] Roe, P. L., 1981. Approximate Riemann solvers, parameter vectors and difference schemes. *J. Comput. Phys.* 43, 357-372.

[108] San O., Kara, K., 2014. Numerical assessments of high-order accurate shock capturing schemes: Kelvin-Helmholtz type vortical structures in high-resolutions. *Comput. Fluids 89* 254-276.

[109] Schwanenberg, D., Köngeter, J., 2000. A discontinuous Galerkin method for the shallow water equations with source terms. Lecture Notes in Computational Science and Engineering, Springer, Berlin, 11, 419-424.

[110] Schwanenberg, D., Harms, M., 2004. Discontinuous Galerkin finite element method for transcritical two-dimensional shallow water flows. *J. Hydr. Engng.* 130(5), 412-421.

[111] Shahbazi, K., Fischer, P. F., Ethier, C. R., 2007. A high-order discontinuous Galerkin method for the unsteady incompressible Navier-Stokes equations. *J. Comput. Phys.* 222, 391-407.

[112] Shi, F., Kirby, J.T., Harris, J.C., Geiman, J.D. and Grilli, S.T., 2012. A high-order adaptive time-stepping TVD solver for Boussinesq modeling of breaking waves and coastal inundation. *Ocean Mode.* 43-44, 36-51.

[113] Shi, F., Dalrymple, R.A., Kirby, J.T., Chen, Q., and Kennedy, A., 2001. A fully nonlinear Boussinesq model in generalized curvilinear coordinates. *Coast. Eng.* 42(4), 337-358.

[114] Shu, C.-W., and Osher, S., 1988. Efficient implementation of essentially non-oscillatory shock-capturing schemes. *J. Comput. Phys.* 77, 439-471.

[115] Sobey, R. J., 2009. Analytical solutions for steep standing waves. *Proceedings of the Institution of Civil Engineers Engineering and Computational Mechanics* 162, December, 2009. EM4, 185-197.

[116] Stratigaki, V., Manca, E., Prinos, P., Losada, I.J., Lara, J.L., Sclavo, M., Amos, C.L., Cáceres, I., and Sànchez-Arcilla, A., 2011. Large-scale experiments on wave propagation over Posidonia oceanica. *J. Hydraulic Research* 49, 31-43.

[117] Steinmoeller, D.T., Stastna, M., Lamb, K. G., 2013. A short note on the discontinuous Galerkin discretization of the pressure projection operator in incompressible flow. *J. Comput. Phys.* 251, 480-486.

[118] Suzuki, T., Zijlema, M., Burger, B., Meijer, M. C., and Narayan, S., 2011. Wave dissipation by vegetation with layer schematization in SWAN. *Coast. Eng.* 59, 64-71.

[119] Tang, J., Causon, D., Mingham, C., and Qian, L., 2013. Numerical study of vegetation damping effects on solitary wave run-up using the nonlinear shallow water equations. *Coast. Eng.* 75, 21-28.

[120] Tang H., Warnecke, G., 2005. A Runge-Kutta discontinuous Galerkin method for the Euler equations. *Comput. Fluids* 34(3), 375-398.

[121] Tassi, P., Bokhove, O., Vionnet, C., 2007. Space discontinuous Galerkin method for shallow water flows kinetic and HLLC flux, and potential vorticity generation. *Adv. Water Resour.* 30(4), 998-1015.

[122] Toro, E. F., Spruce, M., Speares, W., 1994. Restoration of the contact surface in the Harten-Lax-van Leer Riemann Solver. *J. Shock Waves* 4, 25-34.

[123] Toro, E. F., 1999. Riemann solvers and numerical methods for fluid dynamics. A practical introduction (2nd Ed.). Springer-Verlag, New York.

[124] Toro, E. F. 2001. Shock-capturing methods for free-surface shallow flows. Wiley, New York.

[125] Van der Vorst HA., 1992. Bi-CGSTAB: a fast and smoothly converging variant of Bi-CG for the solution of nonsymmetric linear systems. *SIAM Journal on Scientic and Statistical Computing* 13, 631-644.

[126] Wu, C. H., Young, C. C., Chen, Q., and Lynett, P. J., 2010. Efficient nonhydrostatic modeling of surface waves from deep to shallow water. *J. Waterway, Port, Coastal, Ocean Eng.* 136 (2), 104-118.

[127] Wu, W., Ozeren, Y., Wren, D., Chen, Q., Zhang, G., Holland, M., Ding, Y., Kuiry, S.N., Zhang, M., Jadhav, R., Chatagnier, J., Chen, Y., and Gordji, L., 2011. SERRI project: investigation of surge and wave reduction by vegetation. *SERRI Report* 80037-01.

[128] Wu, W., Zhang, M., Ozeren, Y., and Wren, D., 2012. Analysis of vegetation effect on waves using a vertical 2D RANS model. *J. Coast. Res.* 29(2), 383-397.

[129] Xing, Y., Zhang, X., Shu, C.-W., 2010. Positivity-preserving high order well-balanced discontinuous Galerkin methods for the shallow water equations. *Adv. Water Resour.* 33(12), 1476-1493.

[130] Xing, Y., and Zhang, X., 2013. Positivity-preserving well-balanced discontinuous Galerkin methods for the shallow water equations on unstructured triangular meshes. *J. Sci. Comput.* 57, 19-41.

[131] Young, C.-C., Wu, C.H., 2010. A σ-coordinate non-hydrostatic model with embedded Boussinesq-type like equations for modeling deep-water waves. *Int. J. Numer. Meth. Fluids* 63, 1448-1470.

[132] Yuan, H., Wu, C.H., 2006. Fully nonhydrostatic modeling of surface waves. *J. Eng. Mech.* 132, 447-456.

[133] Zhan, J. M., Yu, L. H., Li, C. W., Li, Y. S., Zhou, Q., and Han, Y., 2014. A 3D model for irregular wave propagation over partly vegetated waters. *Ocean Eng.*, 75, 138-147.

[134] Zhang, X., Shu, C.-W., 2010. A genuinely high order total variation diminishing scheme for one-dimensional scalar conservation laws. *SIAM J. Numer. Anal.* 48, 772-795.

[135] Zhao, H. and Chen, Q., 2013. Modeling attenuation of storm surge over deformable vegetation: methodology and verification. *J. Eng. Mech.*, 04014090.

[136] Zhu, L., Chen, Q., and Wan, X., 2014. Optimization of non-hydrostatic Euler model for water waves. *Coast. Eng.* 91, 191199.

[137] Zijlema, M., Stelling, G.S., 2005. Further experiences with computing non-hydrostatic free-surface flows involving water waves. *Int. J. Numer. Meth. Fluids* 48, 169-197.

[138] Zijlema, M., Stelling, G.S., 2008. Efficient computation of surf zone waves using the nonlinear shallow water equations with non-hydrostatic pressure. *Coast. Eng.* 55, 780-790.

[139] Zijlema, M., Stelling, G.S., Smit, P., 2011. SWASH: An operational public domain code for simulating wave fields and rapidly varied flows in coastal waters. *Coast. Eng.* 58, 992-1012.

APPENDIX A DISPERSION RELATION COEFFICIENTS FOR THE THREE-LAYER MODEL

The coefficients $B_1^0,\ B_2^0,\ B_1^1,\ B_2^1,\ B_1^2,\ B_2^2,\ B_3^2,\ C_0,\ C_1,\ C_2$ and C_3 for the three-layer model are given as

$$B_1^0 = -4\alpha_1^2 - 4\alpha_2^2 - 4\alpha_3^2 - 8\alpha_1\alpha_2 - 8\alpha_1\alpha_3 - 8\alpha_2\alpha_3 \tag{A.1}$$

$$B_2^0 = -2\alpha_1^2\alpha_2\alpha_3 - 2\alpha_1\alpha_2^2\alpha_3 - 2\alpha_3^2\alpha_1\alpha_2 \tag{A.2}$$

$$B_3^0 = -\frac{1}{4}\alpha_1^2\alpha_2^2\alpha_3^2 \tag{A.3}$$

$$B_1^1 = -8\alpha_1\alpha_2 - 8\alpha_1\alpha_3 - 8\alpha_2\alpha_3 - 4\alpha_2^2 - 4\alpha_3^2 \tag{A.4}$$

$$B_2^1 = -\alpha_1^2\alpha_2^2 - \alpha_1^2\alpha_3^2 - 2\alpha_1^2\alpha_2\alpha_3 - 2\alpha_1\alpha_2^2\alpha_3 - 2\alpha_1\alpha_2\alpha_3^2 \tag{A.5}$$

$$B_1^2 = -8\alpha_1\alpha_3 - 8\alpha_2\alpha_3 - 4\alpha_3^2 \tag{A.6}$$

$$B_2^2 = -2\alpha_1^2\alpha_2\alpha_3 - 2\alpha_1\alpha_2^2\alpha_3 - \alpha_1^2\alpha_3^2 - 4\alpha_1\alpha_2\alpha_3^2 - \alpha_2^2\alpha_3^2 \tag{A.7}$$

$$B_3^2 = -\frac{1}{4}\alpha_1^2\alpha_2^2\alpha_3^2 \tag{A.8}$$

$$C_0 = 8 \tag{A.9}$$

$$C_1 = 2\alpha_1^2 + 2\alpha_2^2 + 2\alpha_3^2 + 8\alpha_1\alpha_2 + 8\alpha_1\alpha_3 + 8\alpha_2\alpha_3 \tag{A.10}$$

$$C_2 = \frac{1}{2}\alpha_1^2\alpha_2^2 + \frac{1}{2}\alpha_1^2\alpha_3^2 + \frac{1}{2}\alpha_2^2\alpha_3^2 + 2\alpha_1^2\alpha_2\alpha_3 + 2\alpha_1\alpha_2^2\alpha_3 + 2\alpha_1\alpha_2\alpha_3^2 \tag{A.11}$$

$$C_3 = \frac{1}{8}\alpha_1^2\alpha_2^2\alpha_3^2 \tag{A.12}$$

APPENDIX B DIMENSIONLESS COEFFICIENTS OF DISPERSION RELATIONSHIP FOR STOKES WAVES

Let $q = \tanh(kh)$, the dimensionless coefficients D_i are given as (Sobey, 2009)

$$D_1 = q^{1/2} \tag{B.1}$$

$$D_2 = D_4 = 0 \tag{B.2}$$

$$D_3 = -\frac{1}{64}\frac{-9 + 3q^4 + 12q^2 + 2q^6}{q^{7/2}} \tag{B.3}$$

$$D_5 = -\frac{1}{16384}\frac{12q^{16} - 176q^{14} - 681q^{12} + 201q^{10} + 279q^8 - 978q^6 - 279q^4 + 513q^2 + 405}{q^{19/2}} \tag{B.4}$$

APPENDIX C A FIFTH-ORDER STOKES WAVE THEORY FOR STEEP STANDING WAVES

The velocity potential function, water surface elevation, and velocities are given as (Sobey, 2009)

$$\phi(x,\ z,\ t) = (g/k^3)^{1/2} \sum_{i=1}^{5} \epsilon^i \sum_{j=0}^{i} \sum_{m=0}^{i} A_{ijm} \frac{\cosh[jk(h+z)]}{\cosh(jkh)} \cos(jkx) \sin(m\omega t) \tag{C.1}$$

$$\eta(x,\ t) = \frac{1}{k} \sum_{i=1}^{5} \epsilon^i \sum_{j=0}^{i} \sum_{m=0}^{i} b_{ijm} \cos(jkx) \cos(m\omega t) \tag{C.2}$$

$$u(x,\ z,\ t) = \frac{\phi}{x} = -k(g/k^3)^{1/2} \sum_{i=1}^{5} \epsilon^i \sum_{j=0}^{i} \sum_{m=0}^{i} j \cdot A_{ijm} \frac{\cosh[jk(h+z)]}{\cosh(jkh)} \sin(jkx) \sin(m\omega t) \tag{C.3}$$

$$w(x,\ z,\ t) = \frac{\phi}{z} = k(g/k^3)^{1/2} \sum_{i=1}^{5} \epsilon^i \sum_{j=0}^{i} \sum_{m=0}^{i} j \cdot A_{ijm} \frac{\sinh[jk(h+z)]}{\cosh(jkh)} \cos(jkx) \sin(m\omega t) \tag{C.4}$$

where, $\epsilon = 2ka_0$. b_{ijm} and A_{ijm} are dimensionless coefficients that can be found in Sobey (2009).

APPENDIX D CALCULATION OF VEGETATION SWAYING MOTION

The algorithm to solve the complete force balance equation for flexible vegetation using the fourth-order finite element method coupled with a wave model is as follows

- Step 1. Obtain water particle movement W and vegetation deflection ξ from previous time steps $n-1$ and n at each node.
- Step 2. Compute factors f_1 to f_6 using Eqs. (4.15) - (4.20).
- Step 3. Compute local matrices **K**, **J**, **M** and local vectors B, C using Eqs. (4.12), (4.25) - (4.29).
- Step 4. Assemble the local matrices $\mathbf{K}^k$, $\mathbf{J}^k$, $\mathbf{M}^k$ and local vectors B^k, C^k into global ones, **K**, **J**, **M** and B, C, and enforce the boundary conditions.
- Step 5. Solve the global vector X at time step $n+1$ by solving the linear system of equation in Eq. (4.32).
- Step 6. Obtain the vegetation deflection ξ at time step $n+1$ using Eq. (4.21).
- Step 7. Compute the vegetation swaying motion $\dot{\xi} = (\xi^{n+1} - \xi^n)/\Delta t$.

APPENDIX E PERMISSION LETTER 1

ELSEVIER LICENSE
TERMS AND CONDITIONS

Jul 06, 2015

This is a License Agreement between Ling Zhu ("You") and Elsevier ("Elsevier") provided by Copyright Clearance Center ("CCC"). The license consists of your order details, the terms and conditions provided by Elsevier, and the payment terms and conditions.

All payments must be made in full to CCC. For payment instructions, please see information listed at the bottom of this form.

Supplier	Elsevier Limited The Boulevard,Langford Lane Kidlington,Oxford,OX5 1GB,UK
Registered Company Number	1982084
Customer name	Ling Zhu
Customer address	4445 Alvin Dark Ave BATON ROUGE, LA 70820
License number	3663150940693
License date	Jul 06, 2015
Licensed content publisher	Elsevier
Licensed content publication	Coastal Engineering
Licensed content title	Optimization of non-hydrostatic Euler model for water waves
Licensed content author	Ling Zhu,Qin Chen,Xiaoliang Wan
Licensed content date	September 2014
Licensed content volume number	91
Licensed content issue number	n/a
Number of pages	9
Start Page	191
End Page	199
Type of Use	reuse in a thesis/dissertation
Portion	full article
Format	electronic
Are you the author of this Elsevier article?	Yes
Will you be translating?	No
Title of your thesis/dissertation	DEVELOPMENT AND OPTIMIZATION OF NON-HYDROSTATIC MODELS FOR WATER WAVES AND FLUID-VEGETATION INTERACTION

Expected completion date	Aug 2015
Estimated size (number of pages)	111
Elsevier VAT number	GB 494 6272 12
Permissions price	0.00 USD
VAT/Local Sales Tax	0.00 USD / 0.00 GBP
Total	0.00 USD
Terms and Conditions	

INTRODUCTION

1. The publisher for this copyrighted material is Elsevier. By clicking "accept" in connection with completing this licensing transaction, you agree that the following terms and conditions apply to this transaction (along with the Billing and Payment terms and conditions established by Copyright Clearance Center, Inc. ("CCC"), at the time that you opened your Rightslink account and that are available at any time at http://myaccount.copyright.com).

GENERAL TERMS

2. Elsevier hereby grants you permission to reproduce the aforementioned material subject to the terms and conditions indicated.

3. Acknowledgement: If any part of the material to be used (for example, figures) has appeared in our publication with credit or acknowledgement to another source, permission must also be sought from that source. If such permission is not obtained then that material may not be included in your publication/copies. Suitable acknowledgement to the source must be made, either as a footnote or in a reference list at the end of your publication, as follows:

"Reprinted from Publication title, Vol /edition number, Author(s), Title of article / title of chapter, Pages No., Copyright (Year), with permission from Elsevier [OR APPLICABLE SOCIETY COPYRIGHT OWNER]." Also Lancet special credit - "Reprinted from The Lancet, Vol. number, Author(s), Title of article, Pages No., Copyright (Year), with permission from Elsevier."

4. Reproduction of this material is confined to the purpose and/or media for which permission is hereby given.

5. Altering/Modifying Material: Not Permitted. However figures and illustrations may be altered/adapted minimally to serve your work. Any other abbreviations, additions, deletions and/or any other alterations shall be made only with prior written authorization of Elsevier Ltd. (Please contact Elsevier at permissions@elsevier.com)

6. If the permission fee for the requested use of our material is waived in this instance, please be advised that your future requests for Elsevier materials may attract a fee.

7. Reservation of Rights: Publisher reserves all rights not specifically granted in the combination of (i) the license details provided by you and accepted in the course of this licensing transaction, (ii) these terms and conditions and (iii) CCC's Billing and Payment

terms and conditions.

8. License Contingent Upon Payment: While you may exercise the rights licensed immediately upon issuance of the license at the end of the licensing process for the transaction, provided that you have disclosed complete and accurate details of your proposed use, no license is finally effective unless and until full payment is received from you (either by publisher or by CCC) as provided in CCC's Billing and Payment terms and conditions. If full payment is not received on a timely basis, then any license preliminarily granted shall be deemed automatically revoked and shall be void as if never granted. Further, in the event that you breach any of these terms and conditions or any of CCC's Billing and Payment terms and conditions, the license is automatically revoked and shall be void as if never granted. Use of materials as described in a revoked license, as well as any use of the materials beyond the scope of an unrevoked license, may constitute copyright infringement and publisher reserves the right to take any and all action to protect its copyright in the materials.

9. Warranties: Publisher makes no representations or warranties with respect to the licensed material.

10. Indemnity: You hereby indemnify and agree to hold harmless publisher and CCC, and their respective officers, directors, employees and agents, from and against any and all claims arising out of your use of the licensed material other than as specifically authorized pursuant to this license.

11. No Transfer of License: This license is personal to you and may not be sublicensed, assigned, or transferred by you to any other person without publisher's written permission.

12. No Amendment Except in Writing: This license may not be amended except in a writing signed by both parties (or, in the case of publisher, by CCC on publisher's behalf).

13. Objection to Contrary Terms: Publisher hereby objects to any terms contained in any purchase order, acknowledgment, check endorsement or other writing prepared by you, which terms are inconsistent with these terms and conditions or CCC's Billing and Payment terms and conditions. These terms and conditions, together with CCC's Billing and Payment terms and conditions (which are incorporated herein), comprise the entire agreement between you and publisher (and CCC) concerning this licensing transaction. In the event of any conflict between your obligations established by these terms and conditions and those established by CCC's Billing and Payment terms and conditions, these terms and conditions shall control.

14. Revocation: Elsevier or Copyright Clearance Center may deny the permissions described in this License at their sole discretion, for any reason or no reason, with a full refund payable to you. Notice of such denial will be made using the contact information provided by you. Failure to receive such notice will not alter or invalidate the denial. In no event will Elsevier or Copyright Clearance Center be responsible or liable for any costs, expenses or damage incurred by you as a result of a denial of your permission request, other than a refund of the amount(s) paid by you to Elsevier and/or Copyright Clearance Center for denied permissions.

LIMITED LICENSE

The following terms and conditions apply only to specific license types:

15. **Translation**: This permission is granted for non-exclusive world **English** rights only unless your license was granted for translation rights. If you licensed translation rights you may only translate this content into the languages you requested. A professional translator must perform all translations and reproduce the content word for word preserving the integrity of the article. If this license is to re-use 1 or 2 figures then permission is granted for non-exclusive world rights in all languages.

16. **Posting licensed content on any Website**: The following terms and conditions apply as follows: Licensing material from an Elsevier journal: All content posted to the web site must maintain the copyright information line on the bottom of each image; A hyper-text must be included to the Homepage of the journal from which you are licensing at http://www.sciencedirect.com/science/journal/xxxxx or the Elsevier homepage for books at http://www.elsevier.com; Central Storage: This license does not include permission for a scanned version of the material to be stored in a central repository such as that provided by Heron/XanEdu.

Licensing material from an Elsevier book: A hyper-text link must be included to the Elsevier homepage at http://www.elsevier.com . All content posted to the web site must maintain the copyright information line on the bottom of each image.

Posting licensed content on Electronic reserve: In addition to the above the following clauses are applicable: The web site must be password-protected and made available only to bona fide students registered on a relevant course. This permission is granted for 1 year only. You may obtain a new license for future website posting.

17. **For journal authors:** the following clauses are applicable in addition to the above:

Preprints:

A preprint is an author's own write-up of research results and analysis, it has not been peer-reviewed, nor has it had any other value added to it by a publisher (such as formatting, copyright, technical enhancement etc.).

Authors can share their preprints anywhere at any time. Preprints should not be added to or enhanced in any way in order to appear more like, or to substitute for, the final versions of articles however authors can update their preprints on arXiv or RePEc with their Accepted Author Manuscript (see below).

If accepted for publication, we encourage authors to link from the preprint to their formal publication via its DOI. Millions of researchers have access to the formal publications on ScienceDirect, and so links will help users to find, access, cite and use the best available version. Please note that Cell Press, The Lancet and some society-owned have different preprint policies. Information on these policies is available on the journal homepage.

Accepted Author Manuscripts: An accepted author manuscript is the manuscript of an article that has been accepted for publication and which typically includes author-incorporated changes suggested during submission, peer review and editor-author communications.

Authors can share their accepted author manuscript:

- immediately
    - via their non-commercial person homepage or blog
    - by updating a preprint in arXiv or RePEc with the accepted manuscript
    - via their research institute or institutional repository for internal institutional uses or as part of an invitation-only research collaboration work-group
    - directly by providing copies to their students or to research collaborators for their personal use
    - for private scholarly sharing as part of an invitation-only work group on commercial sites with which Elsevier has an agreement
- after the embargo period
    - via non-commercial hosting platforms such as their institutional repository
    - via commercial sites with which Elsevier has an agreement

In all cases accepted manuscripts should:

- link to the formal publication via its DOI
- bear a CC-BY-NC-ND license - this is easy to do
- if aggregated with other manuscripts, for example in a repository or other site, be shared in alignment with our hosting policy not be added to or enhanced in any way to appear more like, or to substitute for, the published journal article.

Published journal article (JPA): A published journal article (PJA) is the definitive final record of published research that appears or will appear in the journal and embodies all value-adding publishing activities including peer review co-ordination, copy-editing, formatting, (if relevant) pagination and online enrichment.

Policies for sharing publishing journal articles differ for subscription and gold open access articles:

Subscription Articles: If you are an author, please share a link to your article rather than the full-text. Millions of researchers have access to the formal publications on ScienceDirect, and so links will help your users to find, access, cite, and use the best available version.

Theses and dissertations which contain embedded PJAs as part of the formal submission can be posted publicly by the awarding institution with DOI links back to the formal publications on ScienceDirect.

If you are affiliated with a library that subscribes to ScienceDirect you have additional private sharing rights for others' research accessed under that agreement. This includes use for classroom teaching and internal training at the institution (including use in course packs and courseware programs), and inclusion of the article for grant funding purposes.

Gold Open Access Articles: May be shared according to the author-selected end-user license and should contain a CrossMark logo, the end user license, and a DOI link to the formal publication on ScienceDirect.

Please refer to Elsevier's posting policy for further information.

18. **For book authors** the following clauses are applicable in addition to the above: Authors are permitted to place a brief summary of their work online only. You are not allowed to download and post the published electronic version of your chapter, nor may you scan the printed edition to create an electronic version. **Posting to a repository:** Authors are permitted to post a summary of their chapter only in their institution's repository.

19. **Thesis/Dissertation**: If your license is for use in a thesis/dissertation your thesis may be submitted to your institution in either print or electronic form. Should your thesis be published commercially, please reapply for permission. These requirements include permission for the Library and Archives of Canada to supply single copies, on demand, of the complete thesis and include permission for Proquest/UMI to supply single copies, on demand, of the complete thesis. Should your thesis be published commercially, please reapply for permission. Theses and dissertations which contain embedded PJAs as part of the formal submission can be posted publicly by the awarding institution with DOI links back to the formal publications on ScienceDirect.

Elsevier Open Access Terms and Conditions

You can publish open access with Elsevier in hundreds of open access journals or in nearly 2000 established subscription journals that support open access publishing. Permitted third party re-use of these open access articles is defined by the author's choice of Creative Commons user license. See our open access license policy for more information.

Terms & Conditions applicable to all Open Access articles published with Elsevier:

Any reuse of the article must not represent the author as endorsing the adaptation of the article nor should the article be modified in such a way as to damage the author's honour or reputation. If any changes have been made, such changes must be clearly indicated.

The author(s) must be appropriately credited and we ask that you include the end user license and a DOI link to the formal publication on ScienceDirect.

If any part of the material to be used (for example, figures) has appeared in our publication with credit or acknowledgement to another source it is the responsibility of the user to ensure their reuse complies with the terms and conditions determined by the rights holder.

Additional Terms & Conditions applicable to each Creative Commons user license:

CC BY: The CC-BY license allows users to copy, to create extracts, abstracts and new works from the Article, to alter and revise the Article and to make commercial use of the Article (including reuse and/or resale of the Article by commercial entities), provided the user gives appropriate credit (with a link to the formal publication through the relevant DOI), provides a link to the license, indicates if changes were made and the licensor is not represented as endorsing the use made of the work. The full details of the license are

available at http://creativecommons.org/licenses/by/4.0.

CC BY NC SA: The CC BY-NC-SA license allows users to copy, to create extracts, abstracts and new works from the Article, to alter and revise the Article, provided this is not done for commercial purposes, and that the user gives appropriate credit (with a link to the formal publication through the relevant DOI), provides a link to the license, indicates if changes were made and the licensor is not represented as endorsing the use made of the work. Further, any new works must be made available on the same conditions. The full details of the license are available at http://creativecommons.org/licenses/by-nc-sa/4.0.

CC BY NC ND: The CC BY-NC-ND license allows users to copy and distribute the Article, provided this is not done for commercial purposes and further does not permit distribution of the Article if it is changed or edited in any way, and provided the user gives appropriate credit (with a link to the formal publication through the relevant DOI), provides a link to the license, and that the licensor is not represented as endorsing the use made of the work. The full details of the license are available at http://creativecommons.org/licenses/by-nc-nd/4.0. Any commercial reuse of Open Access articles published with a CC BY NC SA or CC BY NC ND license requires permission from Elsevier and will be subject to a fee.

Commercial reuse includes:

- Associating advertising with the full text of the Article
- Charging fees for document delivery or access
- Article aggregation
- Systematic distribution via e-mail lists or share buttons

Posting or linking by commercial companies for use by customers of those companies.

20. **Other Conditions**:

v1.7

Questions? customercare@copyright.com or +1-855-239-3415 (toll free in the US) or +1-978-646-2777.

APPENDIX F PERMISSION LETTER 2

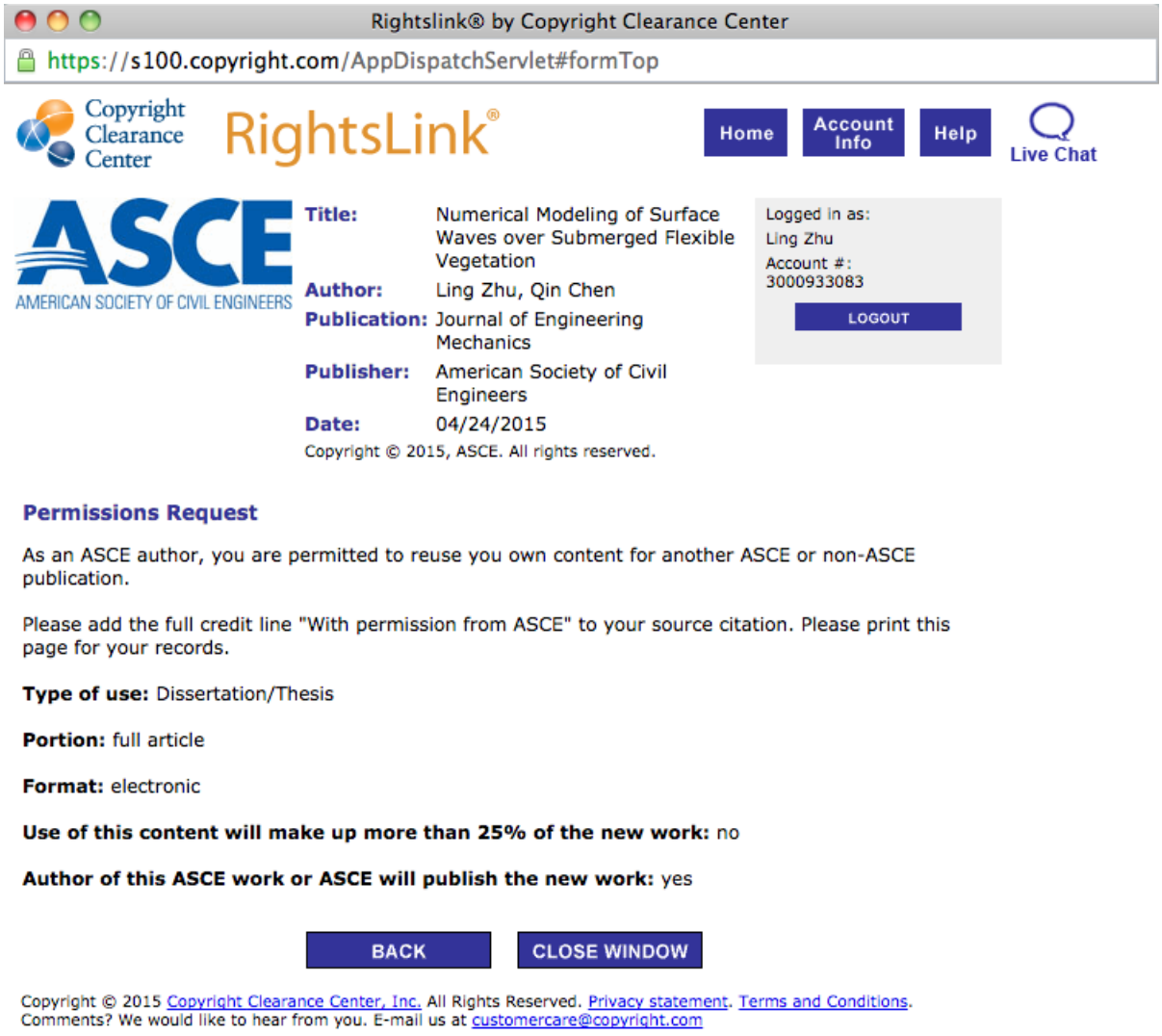

Rightslink® by Copyright Clearance Center

https://s100.copyright.com/AppDispatchServlet#formTop

Copyright Clearance Center RightsLink®

Home | Account Info | Help | Live Chat

ASCE AMERICAN SOCIETY OF CIVIL ENGINEERS

Title: Numerical Modeling of Surface Waves over Submerged Flexible Vegetation

Author: Ling Zhu, Qin Chen

Publication: Journal of Engineering Mechanics

Publisher: American Society of Civil Engineers

Date: 04/24/2015

Copyright © 2015, ASCE. All rights reserved.

Logged in as:
Ling Zhu
Account #:
3000933083

LOGOUT

Permissions Request

As an ASCE author, you are permitted to reuse you own content for another ASCE or non-ASCE publication.

Please add the full credit line "With permission from ASCE" to your source citation. Please print this page for your records.

Type of use: Dissertation/Thesis

Portion: full article

Format: electronic

Use of this content will make up more than 25% of the new work: no

Author of this ASCE work or ASCE will publish the new work: yes

BACK CLOSE WINDOW

Copyright © 2015 Copyright Clearance Center, Inc. All Rights Reserved. Privacy statement. Terms and Conditions.
Comments? We would like to hear from you. E-mail us at customercare@copyright.com

VITA

Ling Zhu came from Changzhou in Jiangsu Province, China. In the fall of 2002, she was enrolled into East China Normal University, located in Shanghai, China. She majored in Mathematics and Applied Mathematics. She received her Bachelor of Science degree in 2006 and entered the graduate school at the same university pursuing the masters degree in Computational Mathematics with the research focused on the inverse eigenvalue problems for a set of Jacobi matrices. During that period, she learned how to build mathematic models to solve practical problems and how to use numerical methods to solve differential equations in the models. She received her master degree of science in May 2009, and in the fall of 2009, she started her Ph.D. study in the Department of Civil and Environmental Engineering at Louisiana State University. She has developed wave models to simulate fully dispersive and highly nonlinear water waves and investigated the wave-vegetation interaction. She has published two journal papers as first author, and several conference papers and presentations. Presently, she is a candidate for the degree of Doctor of Philosophy at Louisiana State University.